

POLITECNICO DI TORINO

Master's Degree in Mechatronic Engineering



Master's Degree Thesis

**On-board electric powertrain control for
the compensation of the longitudinal
acceleration oscillations caused by road
irregularities**

Supervisor

Prof. Alessandro VIGLIANI

Co-supervisor

Prof. Aldo SORNIOTTI

Dr. Antonio TOTA

Author

Silvio SANTORO

A.Y. 2021/2022

"It would be a waste of life to do
nothing with one's ability."

Bruce McLaren

Abstract

The drivability of a vehicle describes all the perceptions of a driver, including perceived safety and comfort. The latter one is mostly affected by road irregularities, involving uncomfortable variations in vertical and longitudinal accelerations of sprung and unsprung masses. While the vertical dynamics has been already fully studied, the longitudinal dynamics has not been completely explored yet. However, although smaller than the vertical acceleration oscillations, the longitudinal acceleration's variations oscillations are not negligible.

The goal of this study is to develop, and to implement in real time, a preemptive non-linear model predictive control (NMPC), whose aim is to attenuate the oscillation of longitudinal acceleration by changing the motor torque requested by the driver. In particular, the controllers have been implemented on a full electric vehicle, which includes a realistic tire model for ride comfort simulation, characterised by three different architectures: the 4 in-wheel motors, 4 on-board motors and 2 on-board motors with open differential. The NMPCs' performances have been evaluated and compared by considering four different key performance indicators (KPIs) along multiple manoeuvres, e.g. uneven road profile and step profile, at different speeds and required motor torques. Further analyses have been conducted to analyse the effect of some powertrain's parameters of the 4 on-board configuration, such as motor time constant, equivalent inertia at the wheel, shaft stiffness and angular backlash, on the controller's capability. In the end, the controllers' capability to be implemented in real time is proved by using dSPACE MicroAutoBox III.

The thesis' project has been developed in collaboration with the Centre of Automotive Engineering at the University of Surrey (UK). The content and the points of novelty of this research work are the subject for a future research paper. A colleague from "Università degli Studi di Pavia", Davide Lazzarini, and I were the engineers responsible for the development of this innovative research project. This activity has been supervised by Prof. Aldo Sorniotti and Prof. Umberto Montanaro, from "University of Surrey", Prof. Alessandro Vigliani, from "Politecnico di Torino", Prof. Antonella Ferrara, from "Università degli Studi di Pavia", and Pietro Stano, PhD student at "University of Surrey".

Table of Contents

| | |
|--|-----------|
| List of Tables | III |
| List of Figures | IV |
| Acronyms | VI |
| 1 Optimization problems and controls | 1 |
| 1.1 Introduction | 1 |
| 1.2 General definitions | 2 |
| 1.3 State space representation | 4 |
| 1.3.1 Class of problems | 6 |
| 1.4 Controllers | 7 |
| 1.4.1 PID | 10 |
| 1.4.2 Fuzzy Control | 11 |
| 1.4.3 Linear Quadratic Regulator | 11 |
| 1.4.4 Sliding Mode Control | 12 |
| 1.4.5 H_∞ | 13 |
| 1.4.6 Model Predictive Control | 13 |
| 1.5 MPC | 14 |
| 1.5.1 Receding horizon | 14 |
| 1.5.2 Cost function | 17 |
| 2 Full Electric Vehicle | 18 |
| 2.1 Introduction | 18 |
| 2.1.1 Internal combustion engine | 19 |
| 2.1.2 Electric motor | 22 |
| 2.2 Full car model | 26 |
| 2.2.1 Motor dynamics | 29 |
| 2.2.2 Powertrains: 4 on-board motors | 31 |
| 2.2.3 Powertrains: 2 on-board motors | 34 |
| 2.2.4 MF-Swift | 37 |

| | | |
|----------|---|-----------|
| 2.2.5 | Anti-properties | 39 |
| 2.2.6 | Rotational dynamics | 42 |
| 2.2.7 | Vertical dynamics | 44 |
| 2.2.8 | Longitudinal dynamics | 45 |
| 3 | Non-Linear MPC | 47 |
| 3.1 | Introduction | 47 |
| 3.1.1 | Acado toolkit | 48 |
| 3.1.2 | Enveloping model and preview | 50 |
| 3.1.3 | Prediction model | 52 |
| 3.1.4 | Simulation environment | 54 |
| 3.2 | Vehicle with in-wheel motors | 59 |
| 3.2.1 | Internal model | 61 |
| 3.3 | Vehicle with 4 on-board motors | 64 |
| 3.3.1 | Internal model | 65 |
| 3.4 | Vehicle with 2 on-board motors | 66 |
| 3.4.1 | Internal model | 68 |
| 4 | Results | 71 |
| 4.1 | Introduction | 71 |
| 4.1.1 | Internal models' validation | 71 |
| 4.1.2 | Performance assessment | 72 |
| 4.2 | Prediction horizon and preview analysis | 73 |
| 4.3 | Controller evaluation on step | 79 |
| 4.4 | Controller evaluation on road with irregularities | 81 |
| 4.5 | Asymmetric road profile | 83 |
| 4.6 | Robustness analysis | 85 |
| 4.6.1 | Speed analysis | 86 |
| 4.6.2 | Torque analysis | 88 |
| 4.7 | Powertrains parameters' sensitivity analysis | 90 |
| 4.7.1 | Backlash sensitivity analysis of different models | 93 |
| 4.8 | dSPACE | 95 |
| | Conclusion | 97 |

List of Tables

| | | |
|------|--|----|
| 2.1 | Main parameters in-wheels motors | 27 |
| 2.2 | Main parameters 4 on-board motors | 28 |
| 2.3 | Main parameters 2 on-board motors | 29 |
| 2.4 | Motor parameters | 30 |
| 2.5 | 4 on-board motors powertrains parameters | 34 |
| 2.6 | 2 on-board motors powertrains parameters | 36 |
| 2.7 | Anti-properties | 41 |
| 2.8 | Suspensions parameters | 44 |
| 3.1 | Prediction model parameters | 54 |
| 3.2 | Differential equations : in-wheel internal model | 62 |
| 3.3 | Differential equations : 4 on-board internal model | 65 |
| 3.4 | Differential equations : 2 on-board internal model | 69 |
| 4.1 | NMPC parameters : in-wheel model | 75 |
| 4.2 | NMPC parameters : 4 on-board model | 77 |
| 4.3 | NMPC parameters : 2 on-board model | 79 |
| 4.4 | Asymmetry analysis KPIs : 4 on-board model | 84 |
| 4.5 | Asymmetry analysis KPIs : 2 on-board model | 84 |
| 4.6 | Speed analysis KPIs : in-wheel model | 87 |
| 4.7 | Speed analysis KPIs : 4 on-board model | 87 |
| 4.8 | Speed analysis KPIs : 2 on-board model | 88 |
| 4.9 | Torque analysis KPIs : in-wheel model | 89 |
| 4.10 | Torque analysis KPIs : 4 on-board model | 89 |
| 4.11 | Torque analysis KPIs : 2 on-board model | 90 |

List of Figures

| | | |
|------|--|----|
| 1.1 | Open loop | 7 |
| 1.2 | Closed loop | 8 |
| 1.3 | Analog signal | 8 |
| 1.4 | Digital signal | 9 |
| 1.5 | Digital controller | 9 |
| 1.6 | PID scheme | 11 |
| 1.7 | Fuzzy scheme | 11 |
| 1.8 | LQR scheme | 12 |
| 1.9 | H_∞ scheme | 13 |
| 1.10 | Model predictive control | 15 |
| 1.11 | Predictive horizon | 16 |
| | | |
| 2.1 | Four-stroke operating cycle | 20 |
| 2.2 | Otto cycle | 21 |
| 2.3 | Diesel cycle | 21 |
| 2.4 | Hard magnetic material's properties | 24 |
| 2.5 | Development of PM materials | 24 |
| 2.6 | Electric motor torque | 26 |
| 2.7 | In-wheels model | 27 |
| 2.8 | 4 on-board model | 28 |
| 2.9 | 2 on-board model | 29 |
| 2.10 | Tip-in tip-out test | 31 |
| 2.11 | 4 on-board motors implementation on Simulink | 32 |
| 2.12 | Half-shaft implementation on Simulink | 33 |
| 2.13 | 2 on-board motors implementation on Simulink | 36 |
| 2.14 | MF-Swift | 38 |
| 2.15 | Anti-properties | 39 |
| 2.16 | Anti-dive and Anti-lift angle | 39 |
| 2.17 | Pitch | 42 |
| 2.18 | Vertical damper forces | 43 |

| | | |
|------|--|----|
| 3.1 | Acado feature | 50 |
| 3.2 | Enveloping model | 51 |
| 3.3 | Schematic of the road preview concept | 52 |
| 3.4 | Schematic of a corner prediction model | 53 |
| 3.5 | Simplified schematic of the simulation and control environment : 4 motors | 54 |
| 3.6 | Main Simulink layer : 4 motors | 56 |
| 3.7 | Controller layer : in-wheels model | 56 |
| 3.8 | Controller layer : 4 on-board model | 57 |
| 3.9 | Enveloping model : 4 on-board and in-wheel models | 57 |
| 3.10 | Simplified schematic of the simulation and control environment : 2 on-board powertrains | 58 |
| 3.11 | Main Simulink layer : 2 on-board model | 58 |
| 3.12 | Controller layer : 2 on-board model | 59 |
| 3.13 | Enveloping model: 2 on-board model | 59 |
| 3.14 | Non-linear vs linear damper | 62 |
| | | |
| 4.1 | Internal models validation | 72 |
| 4.2 | Prediction horizon KPIs : in-wheel model | 73 |
| 4.3 | Computation time : in-wheel model | 74 |
| 4.4 | Preview KPIs : in-wheel model | 74 |
| 4.5 | Prediction horizon KPIs : 4 on-board model | 75 |
| 4.6 | Computation time : 4 on-board model | 76 |
| 4.7 | Preview KPIs : 4 on-board model | 76 |
| 4.8 | Prediction horizon KPIs : 2 on-board model | 77 |
| 4.9 | Computation time : 2 on-board model | 78 |
| 4.10 | Preview KPIs : 2 on-board model | 78 |
| 4.11 | Comparison : step 2 cm | 80 |
| 4.12 | Comparison : uneven road profile | 81 |
| 4.13 | Comparison : road without preview | 82 |
| 4.14 | Comparison : road with preview | 82 |
| 4.15 | Comparison : 2 cm step with asymmetry of 0.25 m | 83 |
| 4.16 | Step asymmetries : 2 on-board motors' model KPI reductions | 85 |
| 4.17 | Step asymmetries : 4 on-board motors' model KPI reductions | 85 |
| 4.18 | Motor time constant sensitivity | 91 |
| 4.19 | Equivalent inertia moment sensitivity | 92 |
| 4.20 | Half shaft stiffness sensitivity | 93 |
| 4.21 | Sensitivity analysis of different models w.r.t. the backlash | 94 |
| 4.22 | dSPACE | 95 |

Acronyms

BC Bottom-Center Crack Position

COG Centre of Gravity

DMC Dynamic Matrix Control

DOF Degree of Freedom

EM Electric Motor

EV Electric Vehicle

GPC Generalized Predictive Control

ICE Internal Combustion Engine

KPI Key Performance Indicator

LP Linear Problem

LQR Linear Quadratic Regulator

MIMO Multi-Input Multi-Output

MPC Model Predictive Control

NLP Nonlinear Problem

NMPC Non-Linear Model Predictive Control

ODE Ordinary Differential Equation

PID Proportional Integral Derivative

PM Permanent Magnet

QP Quadratic Programming

SISO Single-Input Single-Output

SMC Sliding Mode Control

SQP Sequential Quadratic Programming

TC Top-Center Crack Position

Chapter 1

Optimization problems and controls

1.1 Introduction

Optimization problems refers to those problem which aim is to minimize or maximize function respect to some set, finding different solution and determinate which is the best one. In a formally shape, the optimization problem is represented as:

$$\begin{aligned} &\text{optimize } f(x) \\ &x \in S \end{aligned} \tag{1.1}$$

where:

- optimize stands for min or max a function;
- $f : R^n \rightarrow R$ is the objective function, assumed continuous and differentiable, and function of n variables $f(x_1, \dots, x_n)$;
- $S \subseteq R^n$ is the feasible set of the possible choiche for $x = (x_1, \dots, x_n)$.

By considering 1.1 as maximisation problem, it can be rewritten as:

$$\begin{aligned} &\max f(x) \\ &x \in S \end{aligned}$$

which coincides with the minimization problem of the opposite objective function

$$\begin{aligned} &\min -f(x) \\ &x \in S \end{aligned}$$

So can be conclude that the problem can be write as follows:

$$\max_{x \in S} f(x) = - \min_{x \in S} (-f(x))$$

1.2 General definitions

Before getting in to detail of the optimization problem, some important definition must be introduced. The concepts of feasibility and in-feasibility are fundamental; actually, is important to find the best solution of a problem, but firstly must be determined whether or not exist a feasible solution.

- **Unfeasible problem** The optimization problems is unfeasible if $\nexists x \in S$, such that $S \neq \emptyset$, i.e. no solution can be found.
- **Feasible problem** The optimization problems is feasible if $\exists x \in S$, such that $S \neq \emptyset$, i.e. a solution can be found.

This concept can be better understand by considering the following example:

$$\begin{aligned} \min f(x) &= x^3 \\ x &\leq 1 \\ x &> 3 \end{aligned}$$

A feasible solution is one that satisfies all constraints and requirements. On the other hand, a solution is infeasible when no combination of decision variable values can satisfy the entire set of requirements and constraints. Here the optimal solution can not be found due to the constraints.

The optimization problem can be also distinguished, depending if a finite solution exists, in two categories:

- **Bounded Problem:** The minimization problems is bounded if is feasible and \exists a real number $M > 0$ such that $\forall x \in S, |f(x)| \leq M$;
- **Unbounded Problem:** The minimization problems is unbounded if is feasible and \nexists a real number $M > 0$ such that $\forall x \in S, |f(x)| \leq M$.

An example can help understanding what an unbounded problem is:

$$\begin{aligned} \min f(x) &= x^3 \\ x &\leq 2 \end{aligned}$$

in which, for $x \rightarrow -\infty$, the function $f \rightarrow -\infty$ too. In the case in which an opposite constraint (e.g. $x \geq 0$) is added to the feasible set, the problem will not be unbounded anymore.

Solving a feasible and bounded optimization problem, different type of solutions can be obtained. These solution can be divided in two categories:

- **Global minimizer** A point x^* is a global minimizer, or optimal solution, if:

$$f(x^*) \leq f(x) \quad \forall x \in S$$

Depending on the set S , can be done a further distinction: in case the set is open one, also the global minimizer is an unconstrained one; otherwise it is constrained.

In general, an optimization problem has a solution $\longleftrightarrow \exists x^* \in S$ and its value $f(x^*)$ is called *optimal value*.

- **Local minimizer** A point $\bar{x} \in S$ is called local minimizer if for a neighborhood $N(\bar{x}, \rho)$ of \bar{x} :

$$f(\bar{x}) \leq f(x) \quad \text{for all } x \in N \cap S$$

Moreover, a local minimizer $\bar{x} \in S$ is considered a strict one if, for a neighborhood $N(\bar{x}, \rho)$ of \bar{x} :

$$f(\bar{x}) < f(x) \quad \text{for all } x \in N \cap S \text{ with } x \neq \bar{x}$$

Generally, the best solution is to find a global minimizer x^* of f , but it can be difficult to find. Indeed most algorithms are able to find only a local minimizer. Moreover, a global minimizer is also a local point, but a local minimizer is not a global one .

By summarizing, “solving” an optimization problem can be divided in three main step:

- The first thing is check if the feasible set in not empty;
- then must be verify if exist the optimal solution;
- only at this point can be found the optimal solution.

Above, was introduced the concept of constraints; indeed, a feasible set is composed by a finite number of constraints which can be equality or inequality relations, $g_i : \mathbb{R}^n \rightarrow \mathbb{R}, i = 1, \dots, m$. The inequality constraint can be expressed as follows

$$S = x \in \mathbb{R}^n | g_1(x) < 0, g_2(x) < 0, \dots, g_m(x) < 0$$

Talking about the equality constraints, they can be defined as follows by considering the functions $h_j : \mathbb{R}^n \rightarrow \mathbb{R}, i = 1, \dots, p$

$$S = x \in \mathbb{R}^n | h_1(x) = 0, h_2(x) = 0, \dots, h_p(x) = 0$$

A generic problem with both equality and inequality constraint can be defined as follow:

$$\begin{aligned} \min f(x) \\ g_i(x) \leq 0, i = 1, \dots, m \\ h_j(x) = 0, j = 1, \dots, p \end{aligned} \tag{1.2}$$

or in more compact form as

$$\begin{aligned} \min f(x) \\ g(x) \leq 0 \\ h(x) = 0 \end{aligned} \tag{1.3}$$

where $g : \mathbb{R}^n \rightarrow \mathbb{R}^m$ and $h : \mathbb{R}^n \rightarrow \mathbb{R}^p$

In particular, the optimization problem is called **Linear problem (LP)** when the functions $f, g_1, \dots, g_m, h_1, \dots, h_p$, all the function that are involved in the problem, are linear respect to x .

In mathematical terms, the model is the following linear program:

$$\begin{aligned} \min c_1x_1 + c_2x_2 + \dots + c_nx_n \\ a_{i1}x_1 + \dots + a_{in}x_n \geq (\leq / =)b_i \end{aligned} \tag{1.4}$$

Moreover, if the optimization problem is not linear, the problem can be generalize and it is called "Nonlinear programming problem" (NLP).

1.3 State space representation

From Greek, a system is a whole compounded of several parts or members. Nowadays it can be defined as a set of interacting or interdependent entities forming a set of relationships. In a static system the input - output relationship is a static function, where the value $y(t)$ depends on the value $u(t)$ only

$$y(t) = h(u(t)) \forall t$$

In a dynamical system the input – output relationship is dynamical, where the value $y(t)$ does not depend on the value $u(t)$ only, but also on its past values up to time t and on the initial condition of the system

$$y(t) = h(u([0, t]), \dots) \forall t$$

Generally, the behavior of such systems, is described through a system of ordinary differential equations. To simplify this problem, the state space method are introduced. The state space representation of a linear time invariant (LTI) system replaces an n^{th} order differential equation with a single first order matrix differential equation. The state space representation is given by two equations:

$$\begin{aligned} \dot{x}(t) &= Ax(t) + Bu(t) \\ y(t) &= Cx(t) + Du(t) \end{aligned} \tag{1.5}$$

The system is linear because both equation are linear in x and y , and it is time invariant because it does not depend explicitly on time.

The first equation is called the state equation; the second one output equation. Given an n^{th} order system with p inputs and q outputs, the size of each elements and the matrices are as follows:

- $x \in \mathbb{R}^{n \times 1}$ (n rows by 1 column); x is called the state vector, it is a function of time
- $A \in \mathbb{R}^{n \times n}$; A is a constant and is the state matrix;
- $B \in \mathbb{R}^{n \times p}$; B is a constant and is the input matrix;
- $u \in \mathbb{R}^{p \times 1}$; u is function of time and is the input;
- $C \in \mathbb{R}^{q \times n}$; C is a constant and is the output matrix;
- $D \in \mathbb{R}^{q \times p}$; D is a constant and is the direct transition matrix;
- $y \in \mathbb{R}^{q \times 1}$; y is function of time and is the output.

The more general form of a state-space model, for linear and non-linear systems, can be written as two functions:

$$\begin{aligned} \dot{x}(t) &= f(x(t), u(t)) \\ y(t) &= h(x(t), u(t)) \end{aligned} \tag{1.6}$$

In particular, if n and p are equal to 1, the system is called SISO, single input - single output; otherwise, it is called MIMO, multiple input - multiple output.

Let's see the vector notation of the previous system:

$$\begin{aligned}
 x(t) &= \begin{bmatrix} x_1(t) \\ \cdot \\ \cdot \\ x_n(t) \end{bmatrix}, u(t) = \begin{bmatrix} u_1(t) \\ \cdot \\ \cdot \\ u_p(t) \end{bmatrix}, y(t) = \begin{bmatrix} y_1(t) \\ \cdot \\ \cdot \\ y_q(t) \end{bmatrix} \\
 f(x(t), u(t), t) &= \begin{bmatrix} f_1(x(t), u(t), t) \\ \cdot \\ \cdot \\ f_n(x(t), u(t), t) \end{bmatrix}, h(x(t), u(t), t) = \begin{bmatrix} h_1(x(t), u(t), t) \\ \cdot \\ \cdot \\ h_q(x(t), u(t), t) \end{bmatrix}
 \end{aligned} \tag{1.7}$$

1.3.1 Class of problems

Another important aspect of a problem is the time domain. Depending on the sampling time, the problems can be classified as follows:

- **Continuous**

The variables x can take values in \mathbb{R}^n ; it can be further distinguish in:

- if the considered set $S \subset \mathbb{R}^n$, the problem is unconstrained;
- if $S = \mathbb{R}^n$, the problem is *constrained*

- **Discrete**

When the variables x is not taken in \mathbb{R}^n , but in a finite set, it can be further distinguish in:

- *boolean optimization* if $S \subset \{0,1\}^n$;
- *integer programming* when the considered set $S \subset \mathbf{Z}^n$

- **Mixed problems**

- The variables are both continuous and discrete.

Discrete-time systems can be either inherently discrete or obtained as a result of sampling of continuous-time systems. In this kinds of systems, inputs, state space variables, and outputs are expressed in a discrete form and the system models can be represented as follows:

$$\begin{aligned}
 \dot{x}(k+1) &= Ax(k) + Bu(k) \\
 y(k) &= Cx(k) + Du(k)
 \end{aligned} \tag{1.8}$$

As in the continuous problem, the general form , both for linear and non-linear problem, can be the follow:

$$\begin{aligned} \dot{x}(k + 1) &= f(x(k), u(k)) \\ y(k) &= h(x(k), u(k)) \end{aligned} \tag{1.9}$$

1.4 Controllers

Before to talk about different kind of controller, the concept of control system must be introduced. It is defined as a dynamical system that manages the behavior of other devices or systems, in a certain prescribed way without any human action. Moreover, a control system achieves the desired result through control loops.¹ Its basic concept are:

- **The plant** which is the system to be controlled;
- **the controlled output** $y(t)$, which is the physical variable under control;
- **the control input** $u(t)$, which affects the plant and is a manipulable variable;
- **the disturbance input** $d(t)$, which affects the plant hindering the achievement of the control purpose and cannot be manipulated;
- **the reference signal** $r(t)$ gives the prescribed values of the controlled output.

Is important to note that the control input to the plant is provided by a device called controller; it could be in open loop and closed loop. The first one provide the control input to the plant by considering only past and present values of the reference signal; the second one generates the information to the plant not only through $r(t)$, but also with the feedback of the measured output $z(t)$, which is obtained by means of one of more sensors.

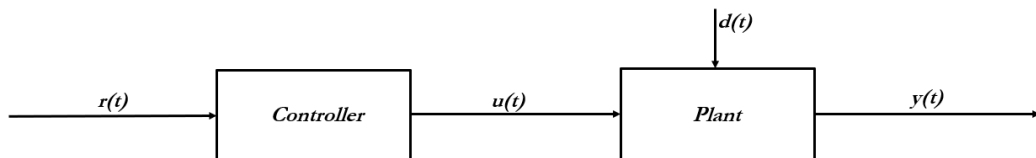


Figure 1.1: Open loop

¹a process designed to maintain the value of a measured process variable at a desired set point.

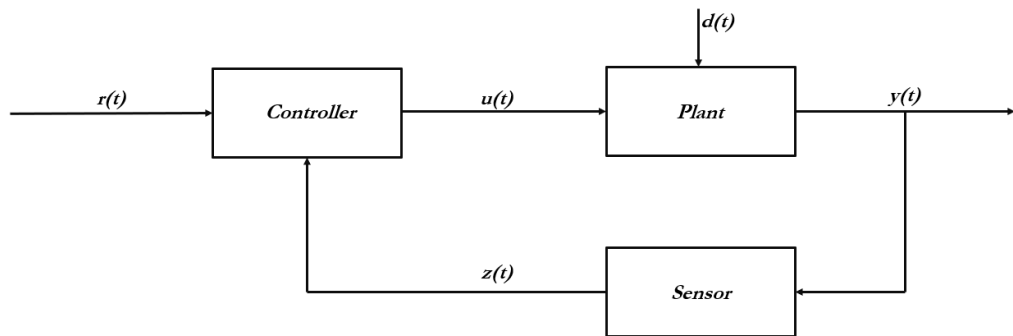


Figure 1.2: Closed loop

Since, as described in the previously, there are two kind of class, there are also two kind of controller: the analog controller and the discrete one. In the first device the signal is analog and the controller is typically realized trough an active electronic filter. An analog system can be represented as a continuous function over time.

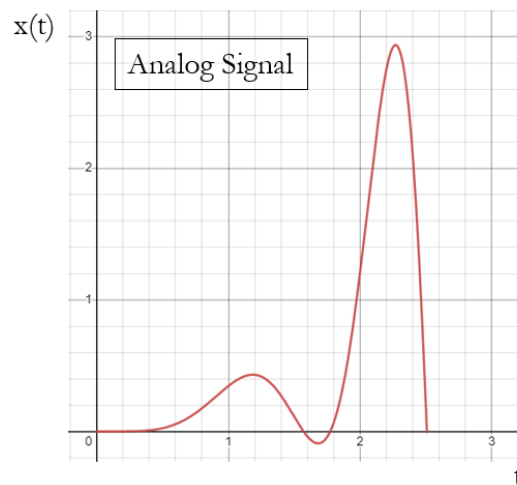


Figure 1.3: Analog signal

With these kind of controllers there could be the following problems:

- Components degradation due to aging;
- parameter uncertainty;
- very expensive in case of re-design;
- electromagnetic disturbances.

A solution to these problems could be design and realize digital controllers.

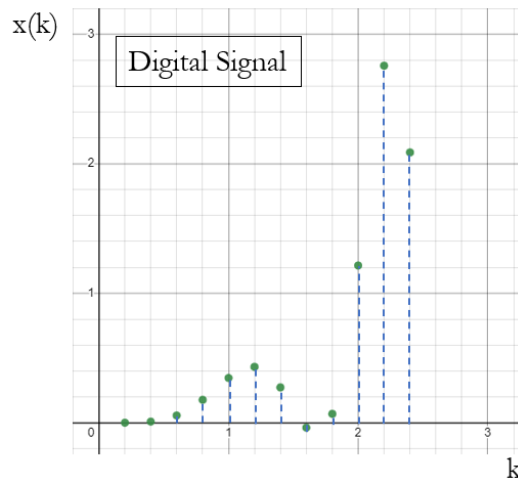


Figure 1.4: Digital signal

In this way the control input can be computed through software algorithms rather than using electronic filter. Other advantages could be:

- flexibility in making modification to the controller after the hardware design is fixed,
- hardware and software design can proceed in parallel,
- rapid prototyping.

Since they work with digital signal, some analog to digital and digital to analog converters (A/D) and (D/A) must be involved in the design of the controller.

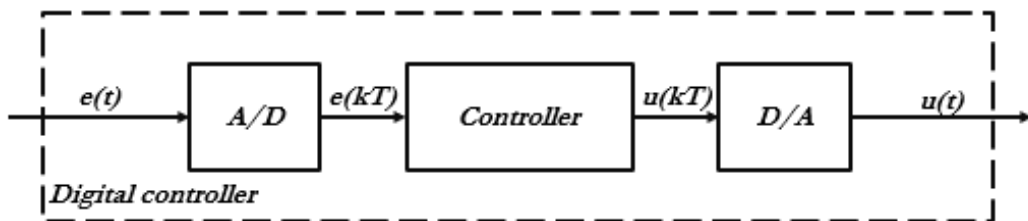


Figure 1.5: Digital controller

Some examples of controllers are discussed in detail below.

1.4.1 PID

One of the most simple and most effective controller is the *PID* controller. It is generally used in industrial control application to regulate temperature, pressure and other different process variables. As matter of fact, its goal is to correct the error between these measured process variable and a desired set-point by computing the difference and then adjusting it by performing a corrective action. A *PID* controller controls a process through three parameters that can be tuned to obtain the desired output: Proportional (P), Integral (I), and Derivative (D).

As discussed in [1], the integral term is useful to reject the constant disturbances and generate a steady-state error equal to zero in tracking constant set-point. Moreover, despite the fact that the integral control filters higher frequency sensor noise, it is generally slow in response to the current error. On the other hand, the proportional term responds immediately to the current error, but with a bad accuracy.

The control law in time-domain is given[2]

$$u(t) = k_p(t) + k_i \int_{t_0}^t e(\tau) d\tau + k_d \frac{d}{dt} e(t) \quad (1.10)$$

- $u(t)$ = controller output
- k_p = Proportional gain
- k_i = Integral gain
- k_d = Derivative gain
- e = error

The parameters k_p , k_i , k_d can either be fixed or computed by a scheme called gain scheduling².

²is a common technique for controlling nonlinear systems with dynamics changing from one operating condition to another.

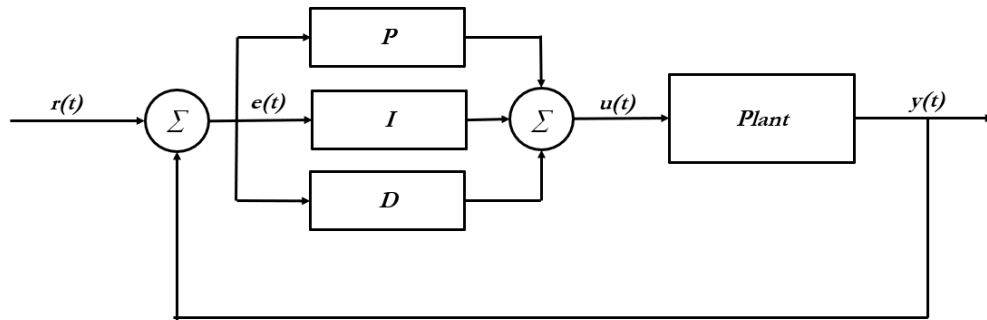


Figure 1.6: PID scheme

1.4.2 Fuzzy Control

The Fuzzy controller, [3], is comparable to the *PID* controller. Actually, it compute the derivative and the integral of the control error or of the control signal. It also has similarities in application because is applied in systems where models are difficult to compute, as for nonlinear dynamics or MIMO (multiple input multiple output) systems. The operation is based on the "if-then" rules; to better understand let's see an example :[2]

if “lateral position error” is left **then** “steering” is right.

In this case, the “lateral position error” refers to the input variable and “steering” the output one.

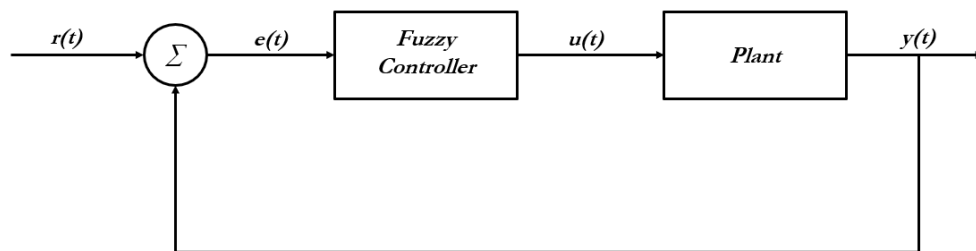


Figure 1.7: Fuzzy scheme

1.4.3 Linear Quadratic Regulator

The linear quadratic regulator (*LQR*) uses the finite horizon linear quadratic (*LQ*) optimal control problem.

The main equation of the controller is $u(t) = -\mathbf{k}^T \mathbf{x}(t)$, where $u(t)$ is the control input, $\mathbf{x} \in \mathbb{R}^n$ represents the states of the system and $\mathbf{k} \in \mathbb{R}^{p \times n}$ is computed in such a manner that the cost function

$$J[u] = \int_0^{\infty} (\mathbf{x}^T \mathbf{Q} \mathbf{x} + \mathbf{u}^T \mathbf{R} \mathbf{u}) dt \quad (1.11)$$

is minimized with respect to an infinite time horizon. This controller, unlike other previous approaches, needs the information of a plant model in advance and actual signals of all states during operation. To obtain these values, a state observer is used for the purpose [4]. The infinite horizon LQ optimal control law $u(t)$ is realized through a static state feedback control architecture.

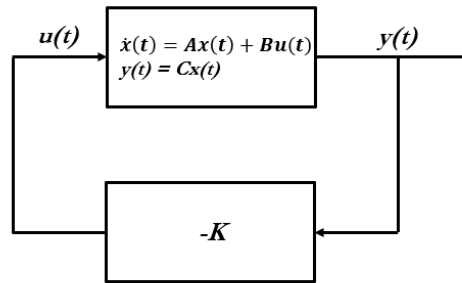


Figure 1.8: LQR scheme

1.4.4 Sliding Mode Control

The sliding mode control (*SMC*) technique is a non linear controller whose main properties are accuracy, robustness, easy tuning and implementation [5]. It is designed in two main parts: in the first one, the sliding surface is designed so that the sliding motion satisfies the desired specification; for example, let's considered the following dynamics, $\dot{s} = \dot{e} + \lambda e$. This variable ensures that the error e , for $s = 0$, goes to 0 in a finite time, depending on the weight of the parameter λ . In the second part, instead, the selection of a control law is established, in such a way that the desired dynamics is obtained; for example, $\dot{s} = -k \text{sign}(s)$ with the control parameter k . This considered switching law may generate chattering in the control input³, that could be avoided by using higher-order *SMC* [6]. A negative aspect of *SMC* is that it is developed in continuous-time, and its discrete-time behavior strongly depends on the sampling frequency [7] [8].

³undesirable phenomenon of oscillations having finite frequency and amplitude

1.4.5 H_∞

H_∞ controllers are used to achieve stabilization with guaranteed performance. [2]. It is a robust technique that allow to control a plant which is characterised by parameter variation and uncertainties. To solve the optimization problem, the H_∞ -norm, 1.12, of a transfer function T of the control system, must be minimize. T is defined by considering different parameters: the plant, the control objective (noise rejection, tracking, etc.), additional uncertainty models, weighting transfer functions and the feedback control matrix. The H_∞ norm of a system $T(s)$ is defined as:

$$\|T\|_\infty := \sup_{\omega \in \mathbb{R}} \|T(j\omega)\|_2 = \sup_{\omega \in \mathbb{R}} \bar{\sigma}[T(j\omega)] \quad (1.12)$$

where $\|\cdot\|_2$ is the induced -norm or equivalently maximum singular value (which is denoted by $\bar{\sigma}$). This norm gives the maximum amplification of an input signal at the output that is caused by the system over all possible input signals.

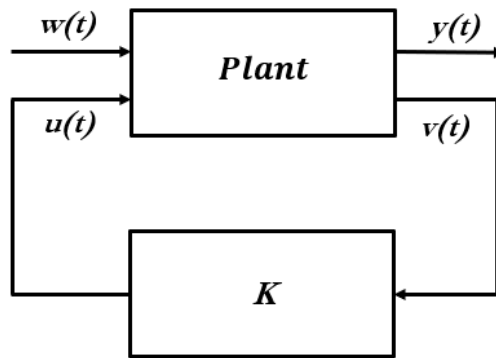


Figure 1.9: H_∞ scheme

The plant has two inputs, as can be seen from the picture: the reference signal and disturbances, defined with $w(t)$, and the manipulated variables $u(t)$. There are also two outputs: the error signals z that must be minimize, and the measured variables v , that is used to control the system.

1.4.6 Model Predictive Control

Model Predictive Control (MPC), is one of the few controllers to have had a significant and widespread impact on industrial process control. The main reason

is that can operate with safety constraints, necessary for the most profitable or most efficient operation in many cases. The diffusion of predictive control into industrial practice has also been helped by the facts that [9]

- its concepts are easy to understand;
- its basic formulation extends to multi-variable plants with almost no modification;
- it is more powerful than *PID* control.

1.5 MPC

As written in [10], the first ideas of receding horizon control and MPC can be found to the 1960s [11], but only in the early 1980s, after a publication on the paper "IDCOM" [12] and dynamic matrix control (*DMC*) [13], the interest in this field started to surge.

In particular, *DMC* had a tremendous impact on industry. In fact, most of the major oil company in the world, employed in most new installations or revamps this approach (or a functionally similar product with a different trade name). [14].

Preliminary research on MPC was marked by attempts to understand *DMC*, which seemed to challenge conventional theoretical analysis because it was formulated in an unconventional way. An example is the development of Internal Model Control (*IMC*) [15], which did not provide any insight into the behavior of constrained *DMCs*, but did lead to some insights into robust control [16].

1.5.1 Receding horizon

To better understand how the predictive control works, it's common to compare this strategy to the chess game. In the chess game, a player chooses a move by projecting in the future the game scenery and trying to predict how the opponent will answer to a sequence of moves. If, at the next turn, the opponent replies in an unexpected way, the player has to re-plan his strategy, to counteract the effect of the opponent move. A good chess player should be able to predict the development of the game for a lot of next turns forward in the time, considering different possible scenarios. Similarly, MPC uses a dynamic model of the system to be controlled to predict the future behavior of the system itself, and thus select the best control inputs to apply to the plant. It is easy to understand that defining the mathematical model of the system is a very important part of the success of this control strategy. On one hand, the model must be descriptive enough to capture all important properties of the system in order to make predictions that are as close as possible to the actual evolution of the process. But on the other hand, if

the model is too descriptive, the complexity will also increase, and the result is that the control system is computationally intensive and can only be handled by expensive hardware devices [17] [18]. Above is shown a generic scheme of a MPC.

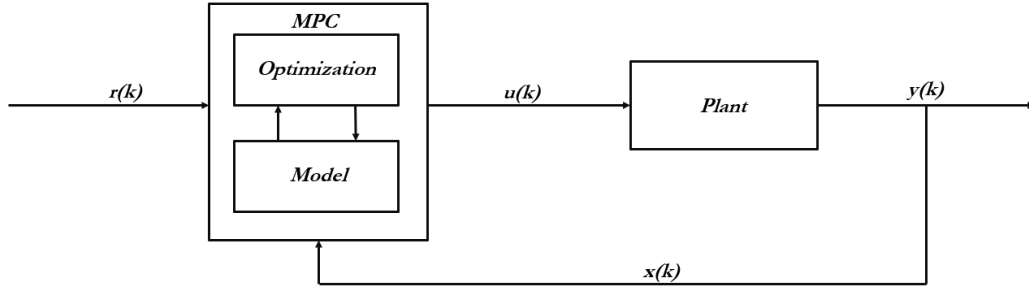


Figure 1.10: Model predictive control

The controller computes the sequence of control inputs for the current and next sample times at each sample time, but only the first one is used in to the plant. After that, the procedure is repeated from the beginning at the next sample time, deleting the other control input values obtained previously. The number of control inputs collected in the control sequence and obtained by the controller at each sample time is determined by the controller's ability to "look forward" in time. This property is defined by a parameter known as Receding Horizon.

Let's consider a single-input, single-output (SISO) and a discrete-time setting. At the current step, the output of the plant is $y(k)$. Also consider the a set-point trajectory, denoted by $s(t)$ at any time t , which is the trajectory that the output should follow, ideally.

By considering the reference trajectory, it begins with the current output $y(k)$ and defines an ideal trajectory along which the plant should return to the set-point trajectory, for example, after a disturbance. It is commonly assumed that the reference trajectory approaches the set-point exponentially from the current output value, with the 'time constant' of the exponential, denoted T_{ref} , defining the response speed. So, if the current error is

$$\epsilon(k) = s(k) - y(k)$$

and the error i steps later, if the output followed it exactly, is

$$\epsilon(k + 1) = e^{\frac{-iT_s}{T_{ref}}} \epsilon(k)$$

where T_s is the sampling interval, the reference trajectory is defined as:

$$r(k+1|k)^4 = s(k+i) - \epsilon(k+i)$$

The internal model of a predictive controller, is used to predict the plant's behavior over a future prediction horizon, starting with the current time. This predicted behavior depends on the assumed input trajectory, $\hat{u}^5(k+i|k)(i = 0, 1, \dots, Hp - 1)$, that is to be applied over the prediction horizon, and the idea is to choose the input with the best predicted behavior. The predicted output is defined as : $\hat{y}(t|k)$

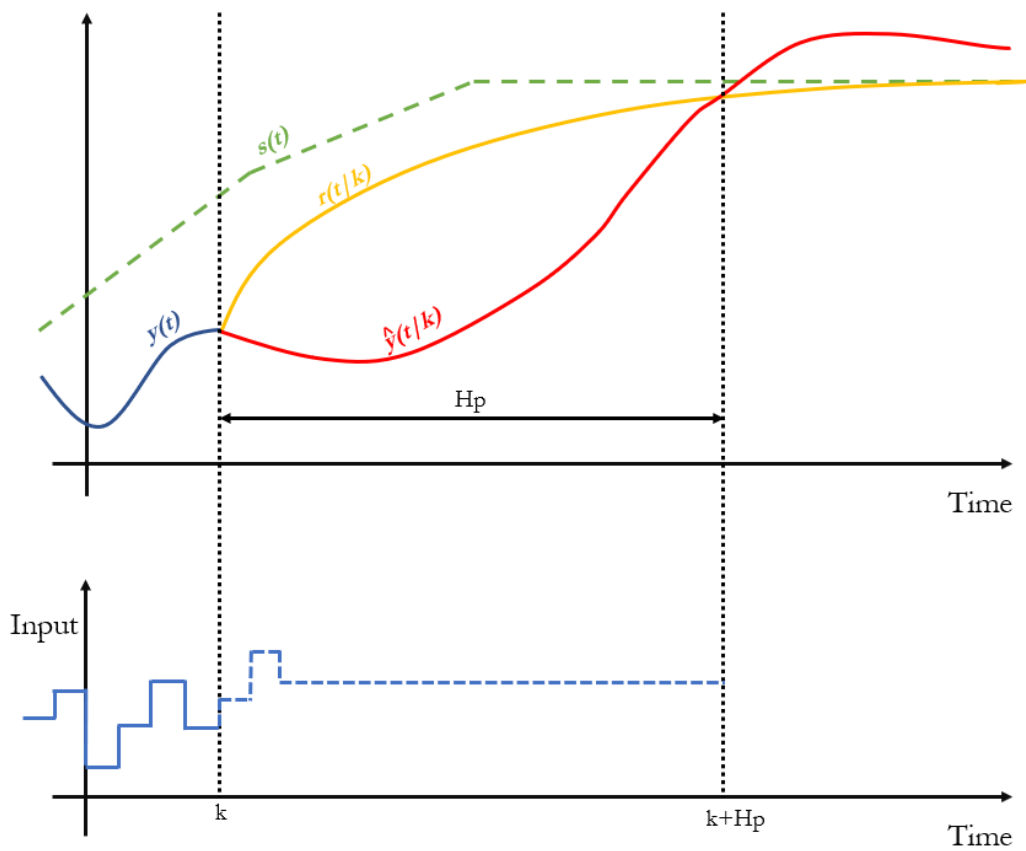


Figure 1.11: Predictive horizon

⁴This notation $(k+1|k)$ indicates that the reference trajectory depends on the conditions at time k

⁵ \hat{u} indicates that at time k we only have a prediction of what the input at time $k+i$ may be

1.5.2 Cost function

MPC control input is computed by solving at each sampling time k the quadratic problem (QP) below:

$$J = \min_{U(k|k)} \sum_{i=0}^{H_p-1} x^T(k+i|k)Qx(k+i|k) + u^T(k+i|k)Ru(k+i|k) + x^T(k+H_p|k)Sx(k+H_p|k) \quad (1.13)$$

with:

$$U(k|k) = [u(k|k)u(k+1|k)\dots u(k+H_c-1|k)]^T, H_c \leq H_p$$

- H_p = Prediction horizon
- H_c = Control horizon
- x = States
- u = Control input
- $Q \in \mathbb{R}^{n \times n} : Q = Q^T \geq 0$
- $R \in \mathbb{R}^{p \times p} : R = R^T > 0$
- $S \in \mathbb{R}^{n \times n} : S = S^T > 0$

Matrices Q and R are the design parameters chosen according to the desired performance trade-off. Moreover, as said before, one of the great features of the *MPC* is the fact that, in the optimization problem is possible to include input and state constraints:

$$s.t. \begin{cases} u_{min} \leq u(k+i|k) \leq u_{max} & i = 0, \dots, H_p - 1 \\ x_{min} \leq x(k+i|k) \leq x_{max} & i = 0, \dots, H_p \end{cases}$$

Chapter 2

Full Electric Vehicle

2.1 Introduction

The drivability of a vehicle describes all the perceptions of a driver, including perceived safety and comfort. The feeling of comfort is mostly affected by road irregularities, involving uncomfortable variations in vertical and longitudinal accelerations of sprung and unsprung masses [19] and in the value and direction of the force applied on the rolling wheel [20][21]. Although longitudinal dynamics on roads with irregularities are significantly affected by tires and suspension, they are rarely mentioned in the literature compared to vertical dynamics and related compensation strategies. But, although smaller than the vertical acceleration oscillation, the longitudinal one is not negligible and therefore has a significant impact on vehicle comfort [22]. Moreover, since the time response of an internal combustion engine, is very slow, and it is difficult to quickly adjust the vehicle's controls to counteract the effects of rough roads, electric powertrains were used in the study improving wheel torque control thanks to the electric motor's accuracy and fast dynamics. Electric vehicles (EVs) are rapidly spreading and becoming important in the automotive market. Among various motor drives, permanent magnet (PM) brushless motor drives, especially permanent magnet synchronous motor drives, are the most attractive motor drives in electric vehicle (EV) drives at present [23]. These benefits are evident in the configuration with in-wheel motors [24], where the motors power the wheel directly due to the fact that are part of the unsprung mass. The main source of torsional dynamic in the in-wheel powertrains is the tire; this effect is explained in [25], in which is proposed a fuzzy logic algorithm to attenuate the associated vibrations. However, some vibration is unavoidable during torque generation due to the mechanical–electrical coupling effect [26]. Among these, the electromagnetic vibration represents the most significant contributor [27] and is mostly affected by an unbalanced airgap flux density distribution [28]. Moreover,

since the ratio between sprung and unsprung mass in the in-wheel powertrains significantly increase, the comfort and road holding suffer [29] [30] [31] [32]. Also, the longitudinal tire force vibrations are affected by the irregularities of the road; indeed, firstly they are transmitted to the unsprung mass by the tire, and then to the sprung mass thanks to the suspension arms and bushings, as explained in [33][34], by worsening the general comfort of the vehicle. Most complex is the vehicle configuration with an on-board location of the motors. Indeed, with these kinds of motors, the longitudinal oscillations are caused, in addition to the problems that characterize the in-wheel model, by the torsional dynamic of some drive-train components, like the half-shafts [35], and they are accentuated by the presence of a backlash in the transmission gears. Indeed, the nonlinear backlash in gearing systems, transmission, and shaft, can cause structural vibration and sharp torque fluctuations [36][37]. The vehicle model that has been studied is a fully electric vehicle, having three different types of powertrains [38]:

- Full electric vehicle with in-wheel motors;
- Full electric vehicle with 4 on-board motors;
- Full electric vehicle with 2 on-board motors.

2.1.1 Internal combustion engine

Internal combustion engines' main function is to convert the chemical energy in fuel into mechanical power [39].

Most reciprocating engines work in a four-stroke cycle. Each cylinder requires four strokes of the piston (two revolutions of the crankshaft) to complete a cycle that produce the power stroke. Both Spark Ignition Engine (SI) and Compression Ignition Engine (CI) use this cycle, which can be explained and divided as follow:

- An *intake stroke*: during this stage, the piston starts in the position TC, the top-center crank position, and ends at BC, the bottom center crank position. Here fresh air or fuel-air mixture enters into the cylinder. the intake valve opens before the start of the stroke and closes at the end of the stroke, to increase intake air mass;
- A *compression stroke*: during this stage, the piston moves up the cylinder bore from BC to TC; this upward movement of the piston mixes compressed air/fuel in the combustion chamber; combustion starts to take place at the end of the compression stroke, and the pressure in the cylinder increases more quickly.

- A *power stroke*: In this stage, the piston moves down the cylinder bore from TC to BC and rotates the crankshaft. This happens because, at the end of the compression stroke, the spark plug fires and ignites the compressed air / fuel mixture. The exhaust valve opens as the piston approaches BC to start the exhaust process and reduce the cylinder pressure to nearly that of the exhaust system.
- An *exhaust stroke*: As final stage, the piston moves up the cylinder bore from BC to TC. This final stroke forces the spent gasses/exhaust out of the cylinder and the piston is ready to begin the intake stroke.

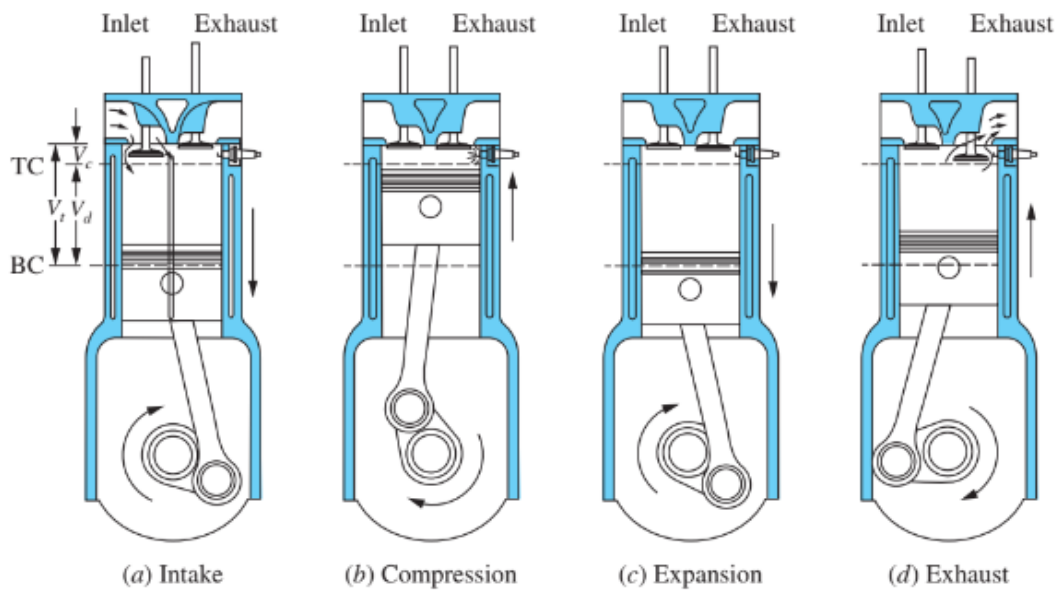


Figure 2.1: Four-stroke operating cycle

SI engine (Spark Ignition Engine) uses the spark from the spark plug to ignite. These engines work according to the Otto cycle. The air-fuel mixture is produced by a carburetor and injected into the engine cylinders for combustion. The spark plug then produces a spark to begin combusting the air-fuel mixture. Because there is no such air compression to initiate combustion of the fuel-air mixture, SI engines typically have low compression ratios. That's why gasoline engines are less powerful.

CI Engine (Compression Ignition Engine) is based on diesel cycle. They do not use a carburetor to mix air and fuel. Instead, air is drawn in and pressurized during the suction stroke. When the air is sufficiently pressurized, fuel is injected through the fuel injectors. Heat from the highly compressed air begins to ignite.

Diesel engines have higher compression ratios than any other SI engine due to the excessive pressure required to compress the air. In addition, the CI engine has more noise and vibration.

The difference between the two engines can be shown through the following graphs which represent the evolution of pressure, volume, temperature and entropy, during the cycle.

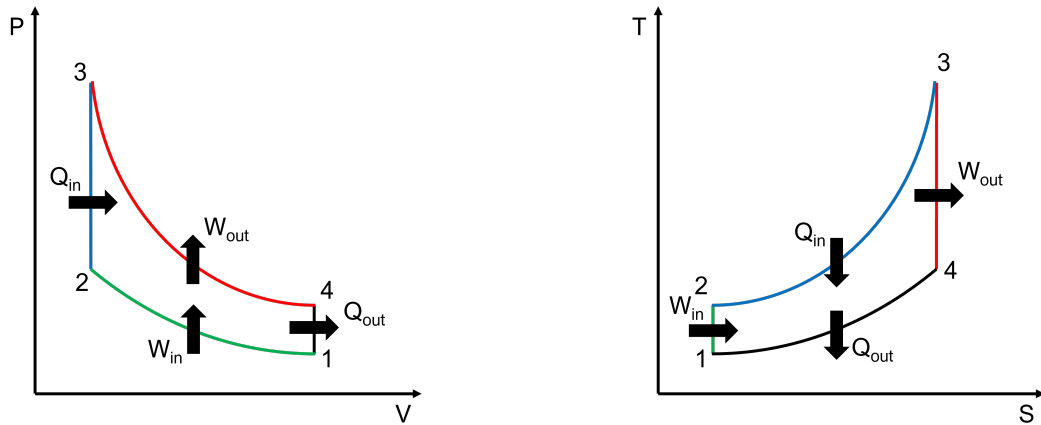


Figure 2.2: Otto cycle

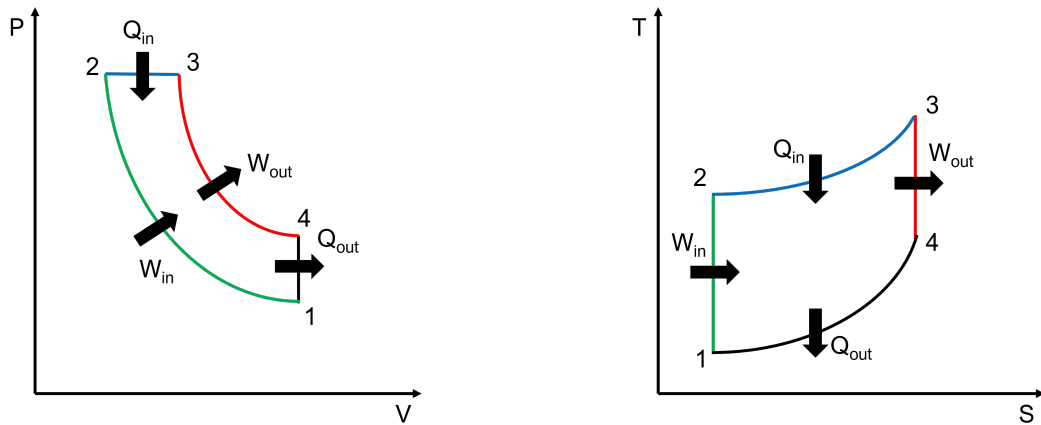


Figure 2.3: Diesel cycle

where:

- 1-2: Isentropic compression
- 2-3: Constant pressure (Diesel cycle) or volume (Otto cycle) heat addition

- 3-4: Isentropic expansion
- 4-1: Constant volume heat rejection

SI engine reaches higher temperature than CI engine, but it reaches lower pressure.

2.1.2 Electric motor

Electric vehicles (EVs) are rapidly spreading and becoming important in the automotive market. Compared to conventional combustion engines and friction brakes, electric powertrains typically offer improved wheel torque control because of the electric motor's accuracy and fast dynamics. Among various motor drives, permanent magnet (PM) brushless motor drives, especially permanent magnet synchronous motor drives, are the most attractive motor drives in electric vehicle (EV) drives at present. Before to getting in detail of these kind of motors, some background information must be introduced.

Their main advantages are as follows [23] :

- Since the magnetic field is excited by high-energy PM, the total weight and volume can be significantly reduced to obtain a specific power output;
- they provide higher efficiency due to the absence of rotor copper losses;
- since heat is mainly generated in the stator, it is better dissipated to the environment, making cooling easier;
- because PM excitation does not cause manufacturing defects, overheating or mechanical damage, they inherently provide higher reliability.;

However, these machines still have some disadvantages, as follows:

- Since the high-energy PM is based on rare earth elements, the machine cost is much higher than the induction counterpart;
- the constant power operating range is limited by the inherently uncontrollable PM flux;
- because of the inherently uncontrollable PM flux, the constant-power operation range is limited;

- if the machine is not designed or operated properly, PM accidental demagnetization by high armature reaction fields or at high voltages Operating temperature.

Brushless has been very successful for many reasons. In this type of motor, the rotor has no windings, which makes cooling easier because there is no current on the rotor, the motor is more compact, and it is possible to operate in a deflagration environment. In addition, due to the reduction in size and inertia, but also due to the air gap is always affected by the permanent magnets. Another important aspect is mechanical materials, especially magnet materials. There are currently four main types of PM materials that are widely used for motor drives:

- Ferrite;
- Alnico;
- Samarium-cobalt (Sm-Co);
- Neodymium-iron-boron (Nd-Fe-B).

These material guarantee the following advantages:

- *High residual induction B_r* : this property allows to create the excitation flow without the need of power supply. The flow is given by $\Phi = B \cdot s$. Having an high value of B means that we can reduce the dimensions of the machine. Moreover, the higher B , the lower the necessary current to produce the same value of torque;
- *High coercive force H_r* : it is the value of the field with opposite sign of the magnetization. The coercive force has to be applied to let the magnetic induction of the magnet cancels out. The higher H , the more resistant the magnet to demagnetization.

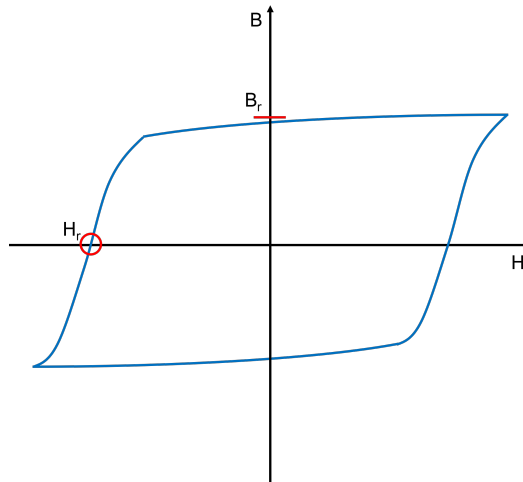


Figure 2.4: Hard magnetic material's properties

The figure 2.5 shows the typical demagnetization performance of the above PM materials; the remanence B_r indicates the strength of the magnetic field produced, and the coercivity and H_c indicate the resistance to demagnetization.

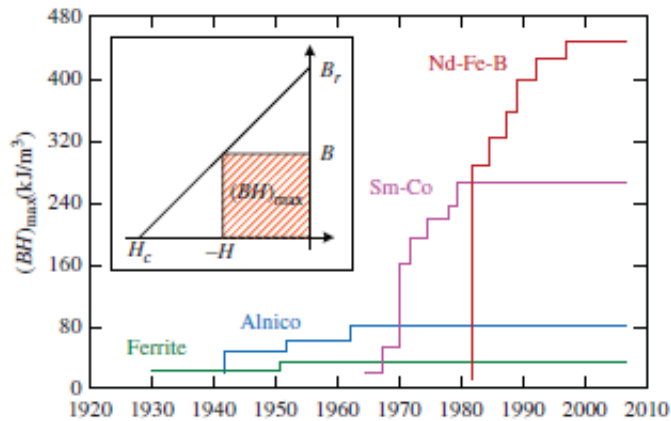


Figure 2.5: Development of PM materials

The working mode of this kind of motors is explained below:

The permanent magnets generate a rotor magnetic field $\overline{\Phi}_r$ and at the same time the currents that goes through the stator generate a stator magnetic field $\overline{\Phi}_s$. The directions of the fields $\overline{\Phi}_r$ and $\overline{\Phi}_s$ are out of phase by an angle θ . From the interaction between these two fields, a torque is generated. So, the torque depends on the angle θ .

A three-phase brushless motor, with star configuration, can be represented by the following model:

$$\begin{cases} v_a = R_s i_a + \frac{d\Phi_a}{dt} \\ v_b = R_s i_b + \frac{d\Phi_b}{dt} \\ v_c = R_s i_c + \frac{d\Phi_c}{dt} \\ J \frac{d\omega_m}{dt} = C_e - C_r \end{cases}$$

where the first 3 equations are the stator equations, while the last one is the mechanical equation of the motor. Moreover:

- v_a, v_b, v_c are the phase voltages,
- i_a, i_b, i_c are the phase currents,
- R_s is the stator resistance,
- Φ_a, Φ_b, Φ_c are the concatenated flows at the windings,
- J is the moment of inertia of the motor,
- ω_m is the motor angular speed,
- C_e and C_r are the electric motor torque and the resistance torque.

The concatenated flows can be represented as function of currents and inductance as follows:

$$\begin{aligned} \Phi_a &= L_a(\theta)i_a + M_{ab}(\theta)i_b + M_{ac}(\theta)i_c + \Phi_{ma}(\theta) \\ \Phi_b &= L_b(\theta)i_b + M_{ba}(\theta)i_a + M_{bc}(\theta)i_c + \Phi_{mb}(\theta) \\ \Phi_c &= L_c(\theta)i_c + M_{ca}(\theta)i_a + M_{cb}(\theta)i_b + \Phi_{mc}(\theta) \end{aligned}$$

where L is the auto-inductance, M is the mutual inductance and Φ_m is the flow generated by the permanent magnet.

Finally, the electric motor torque can be obtained as follows:

$$C_e = pp \left(\frac{1}{2} [i_s]^T \frac{d[L(\theta)]}{d\theta} [i_s] + [i_s]^T \frac{d[\Phi_m(\theta)]}{d\theta} \right)$$

where pp is the pair of poles and the first element of the sum is the reluctance torque, which is due to the reluctance variation seen by the stator and it is only present in anisotropic machines. On the other hand, the second element is the cylindrical torque, which is due to the interactions between the stator currents and the magnetic flow generated by the permanent magnets. This second torque component is always present.

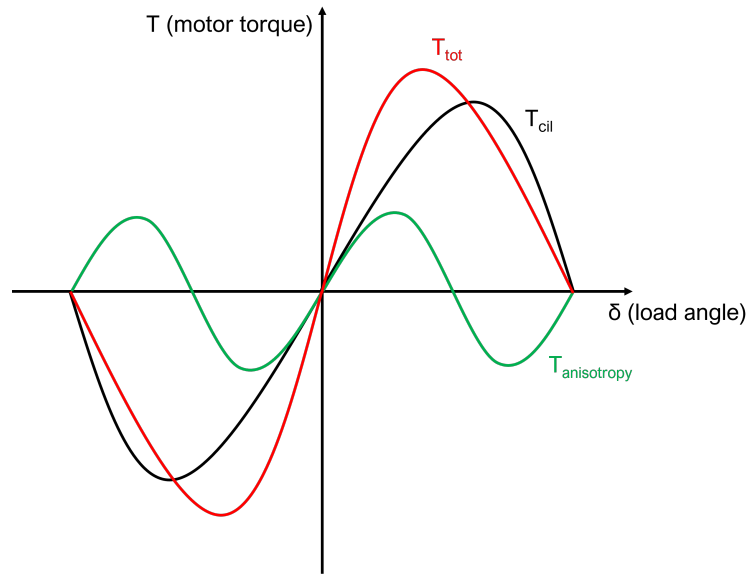


Figure 2.6: Electric motor torque

2.2 Full car model

As mentioned at the beginning of the chapter, the vehicle model that has been studied is a part-time all-wheel ¹ drive electric vehicle model, having three different types of powertrains [38]. The first model is composed by 4 motors positioned directly on the unprung masses : the in-wheel motors.

¹A part-time system has the capability of delivering power to all of the tires but only does so when it is required.

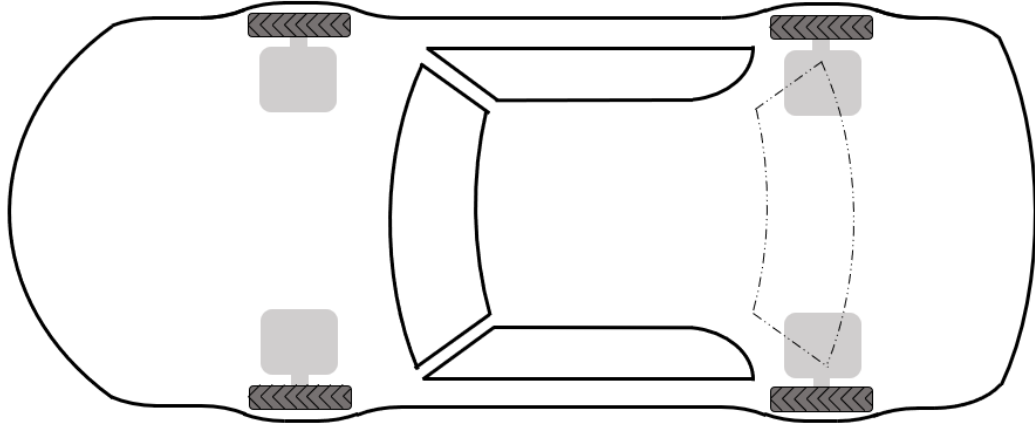


Figure 2.7: In-wheels model

In the 2.1 are shown the main values that characterize the vehicle, as the weight of the sprung and unsprung mass, the wheel radius, etc.

| Parameter | Description | Value | Unit |
|-------------|-----------------------------|--------|------------------------|
| m_b | Sprung mass | 2593.0 | [kg] |
| $I_{b,y}$ | Vehicle body inertia | 2200 | [kg · m ²] |
| a | Front semi-wheelbase | 1.4727 | [m] |
| b | Rear semi-wheelbase | 1.4553 | [m] |
| h_g | COG height | 0.631 | [m] |
| $m_{u,F}$ | Front unsprung mass | 65 | [kg] |
| $m_{u,R}$ | Rear unsprung mass | 65 | [kg] |
| $I_{u,F,y}$ | Front unsprung mass inertia | 1.60 | [kg · m ²] |
| $I_{u,R,y}$ | Rear unsprung mass inertia | 1.60 | [kg · m ²] |
| R_F | Front wheel radius | 0.3725 | [m] |
| R_R | Rear wheel radius | 0.3725 | [m] |

Table 2.1: Main parameters in-wheels motors

The second one has 4 motors, one for each wheel, positioned on the chassis. In this case the electric motors do not power the wheel directly. There's need for a gearbox and driveshaft. When using a reduction gearbox, the speed is reduced and the torque is multiplied.

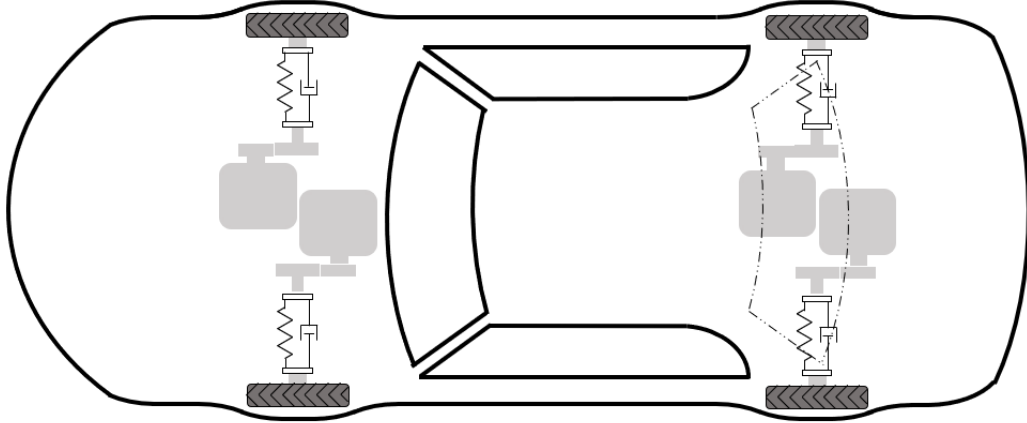


Figure 2.8: 4 on-board model

As for the previous case, in 2.2 are shown the main values of the model.

| Parameter | Description | Value | Unit |
|-------------|-----------------------------|--------|------------------------|
| m_b | Sprung mass | 2789.0 | [kg] |
| $I_{b,y}$ | Vehicle body inertia | 2200 | [kg · m ²] |
| a | Front semi-wheelbase | 1.4727 | [m] |
| b | Rear semi-wheelbase | 1.4553 | [m] |
| h_g | COG height | 0.631 | [m] |
| $m_{u,F}$ | Front unsprung mass | 30 | [kg] |
| $m_{u,R}$ | Rear unsprung mass | 30 | [kg] |
| $I_{u,F,y}$ | Front unsprung mass inertia | 1.39 | [kg · m ²] |
| $I_{u,R,y}$ | Rear unsprung mass inertia | 1.39 | [kg · m ²] |
| R_F | Front wheel radius | 0.3725 | [m] |
| R_R | Rear wheel radius | 0.3725 | [m] |

Table 2.2: Main parameters 4 on-board motors

By comparing 2.1 and 2.2 , is important to observe how the weight of the sprung mass and unsprung changes.

The last model, is the most complex one and it is composed by two motors, one on the front and one on the rear. Each motor is linked to the corresponding wheels through an open differential.[40]

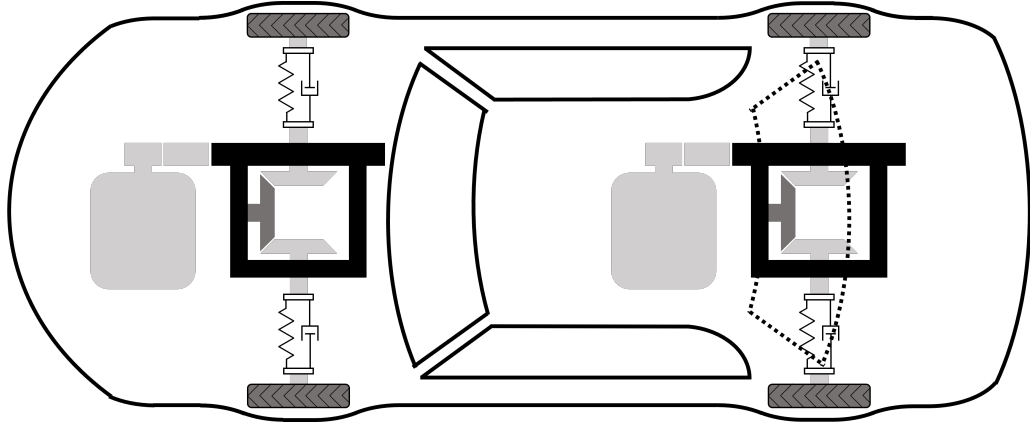


Figure 2.9: 2 on-board model

The model has 15 degrees of freedom (DOF) corresponding to different dynamics (longitudinal, vertical and rotational) of the sprung and unsprung masses.

| Parameter | Description | Value | Unit |
|-------------|-----------------------------|--------|------------------|
| m_b | Sprung mass | 2821.8 | $[kg]$ |
| $I_{b,y}$ | Vehicle body inertia | 2200 | $[kg \cdot m^2]$ |
| a | Front semi-wheelbase | 1.4727 | $[m]$ |
| b | Rear semi-wheelbase | 1.4553 | $[m]$ |
| h_g | COG height | 0.631 | $[m]$ |
| $m_{u,F}$ | Front unsprung mass | 30 | $[kg]$ |
| $m_{u,R}$ | Rear unsprung mass | 30 | $[kg]$ |
| $I_{u,F,y}$ | Front unsprung mass inertia | 1.39 | $[kg \cdot m^2]$ |
| $I_{u,R,y}$ | Rear unsprung mass inertia | 1.39 | $[kg \cdot m^2]$ |
| R_F | Front wheel radius | 0.3725 | $[m]$ |
| R_R | Rear wheel radius | 0.3725 | $[m]$ |

Table 2.3: Main parameters 2 on-board motors

By considering these two tables, 2.3 and 2.2, the values that changes are the weight of the sprung mass; this is due to the fact that the weight of the motor of the model with 2 on-board powertrains is heavier.

2.2.1 Motor dynamics

The inverter and electric motor (EM) dynamics are modelled as a first order system:

$$\dot{T}_m = \frac{T_{m,cor} - T_m}{\tau_m} \quad (2.1)$$

Where T_m is the actual electro-magnetic motor torque, $T_{m,cor}$ is the motor torque correction imposed by the longitudinal vibration controller and τ_m is the time constant of the electric drive.

In case of in-wheel motors, shown in figure 2.9, T_m is the motor torque at the wheels, otherwise there are transmission ratios and torsional dynamics of the half shafts in between.

In 2.4 are show the main values used in all three cases:

| Vehicle with in-wheel motors | | | |
|---------------------------------------|----------------------|---------------------|------------------------|
| Parameter | Description | Value | Unit |
| m_m | Motor mass | 35 | [kg] |
| τ_m | Motor time constant | $5.7 \cdot 10^{-3}$ | [s] |
| J_m | Motor inertia | $2.1 \cdot 10^{-1}$ | [kg · m ²] |
| T_m | Maximum motor torque | 1500 | [N · m] |
| Vehicle with 4 on-board motors | | | |
| Parameter | Description | Value | Unit |
| m_m | Motor mass | 49 | [kg] |
| τ_m | Motor time constant | $5.7 \cdot 10^{-3}$ | [s] |
| J_m | Motor inertia | $6.7 \cdot 10^{-2}$ | [kg · m ²] |
| T_m | Maximum motor torque | 350 | [N · m] |
| Vehicle with 2 on-board motors | | | |
| Parameter | Description | Value | Unit |
| m_m | Motor mass | 57.2 | [kg] |
| τ_m | Motor time constant | $2.5 \cdot 10^{-2}$ | [s] |
| J_m | Motor inertia | $8.6 \cdot 10^{-2}$ | [kg · m ²] |
| T_m | Maximum motor torque | 400 | [N · m] |

Table 2.4: Motor parameters

In these tables, are highlight the different weight of the motor mass, and, most of all, the motor time constant. The case study EV is a sport utility vehicle, used as one of the demonstrators of the European Horizon 2020 EVC1000 project [41]. The powertrain parameters, instead, are obtained by literature; in particular the in-wheel considers values shown in [42], the 4 on-board in [43] and 2 on-board in [44]. As the complexity of the model increase, the motors adopted also becomes more complex. The longitudinal acceleration of the vehicle has been recorded

during a Tip in Tip out test [45], shown in Fig. 2.10, in order to highlight the promptness of the considered motors subjected to sudden changes of the vehicle acceleration. All of three configurations has been tested with the same reference torque at wheel equal to 1500 Nm, obtained, for the on-board configuration, thanks an appropriate value of transmission ratio. Due to the presence of bigger motor inertia, mass, motor time constant, and different powertrains configuration the motor on the 2 on-board configuration has a slower time response; on the other hand, the motor used for the in-wheel configuration present a faster dynamic. Moreover, the on-board powertrains have been experimentally tested at the Lommel proving ground (Belgium) along numerous tip-in manoeuvres at different initial vehicle speeds and requested torque, obtaining a good match between simulations and experiments. [40]

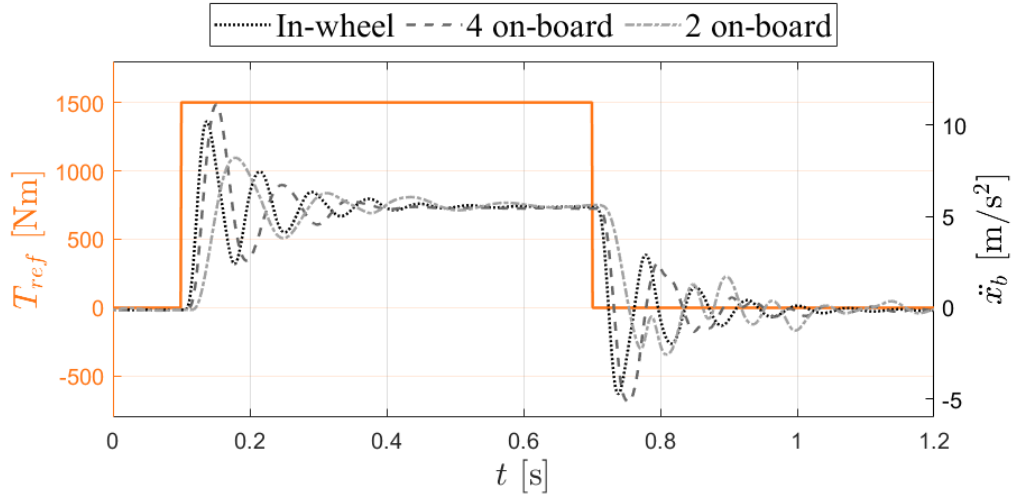


Figure 2.10: Tip-in tip-out test

2.2.2 Powertrains: 4 on-board motors

Since the on-board motors are linked to the wheels through a shaft, as shown in 2.8, the motor torque T_m is no longer the motor torque at the wheel. The torsional dynamics of the shaft is described by the following equation:

$$T_t - J_{eq}\ddot{\theta}_s - T_{hs} = 0 \quad (2.2)$$

Where $\ddot{\theta}_s$ is the angular acceleration of the shaft, T_{hs} is the motor torque at the half shaft, J_{eq} is the equivalent moment of inertia at the shaft, and T_t is the motor torque at the gearbox.

In particular T_t is calculated as follows:

$$T_t = T_m i_t \eta_t \quad (2.3)$$

Where i_t and η_t are the total gear ratio and efficiency obtained respectively by the product between the first and second gear ratio i_{g1} and i_{g2} , and the first and second gear efficiency η_{g1} and η_{g2} .

J_{eq} is obtained as follows:

$$J_{eq} = J_m i_t^2 \eta_t + J_{g1} i_t^2 \eta_t + J_{g2} i_{g2}^2 \eta_{g2} + J_{g3} i_{g2}^2 \eta_{g2} + J_{g4} + \frac{1}{2} J_{hs} \quad (2.4)$$

Where J_m is the moment of inertia of the motor, J_{g1} , J_{g2} , J_{g3} and J_{g4} are respectively the moment of inertia of the first, second, third and fourth gear and J_{hs} is the moment of inertia of the half shaft.

Below is shown the implementation with Simulink.

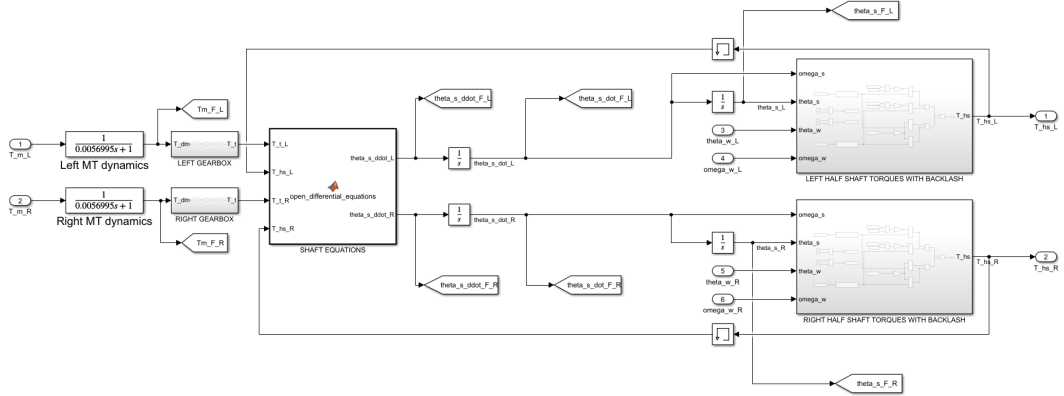


Figure 2.11: 4 on-board motors implementation on Simulink

In the formula 2.4 was introduced the motor torque at the half shaft. It can be formulated in two components and represented by a spring and damper system:

$$\begin{aligned} T_{hs} &= T_{hs,K} + T_{hs,\beta} \\ T_{hs,K} &= f_a f_1 + f_b f_2 \\ T_{hs,\beta} &= f_c f_1 + f_c f_2 \\ f_a &= K_{hs}(\Delta\theta + \alpha) \\ f_b &= K_{hs}(\Delta\theta - \alpha) \\ f_c &= \beta_{hs} \Delta\dot{\theta} \\ \Delta\theta &= \theta_s - \theta_w \end{aligned} \quad (2.5)$$

In particular K_{hs} and β_{hs} are the spring and damper constant of the half shaft, θ_s and θ_w are the angular displacement of the half shaft and the wheels and f_a , f_b and f_c are linear functions.

In this case, since model has to be as real as possible, also the backlash in the differential has been considered.[46] [47] The backlash, sometimes called lash or play, is clearance between mating components, sometimes described as the amount of lost motion due to clearance or slackness when movement is reversed, and contact is re-established. f_1 and f_2 are switching function modelled as follows:

$$f_1 = \begin{cases} 1 & \text{if } \Delta\theta < -\alpha \\ 0 & \text{if } \Delta\theta \geq -\alpha \end{cases}$$

$$f_2 = \begin{cases} 1 & \text{if } \Delta\theta > \alpha \\ 0 & \text{if } \Delta\theta \leq \alpha \end{cases}$$
(2.6)

Where α is half of the considered backlash. Below is shown the implementation of the backlash with simulink.

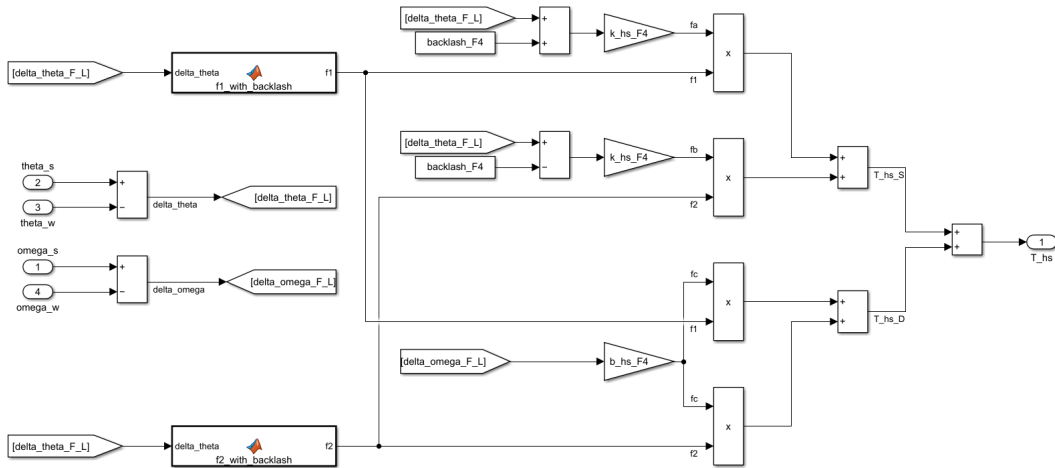


Figure 2.12: Half-shaft implementation on Simulink

In the following table are shown the main values used:

| Parameter | Description | Value | Unit |
|--------------|---|---------------------|-----------------------------------|
| i_{g1} | First gear ratio | 2.128 | [-] |
| i_{g2} | Second gear ratio | 2.128 | [-] |
| η_{g1} | First gear efficiency | 0.98 | [-] |
| η_{g2} | Second gear efficiency | 0.98 | [-] |
| J_{g1} | First gear inertia | $1.9 \cdot 10^{-3}$ | $[kg \cdot m^2]$ |
| J_{g2} | Second gear inertia | $4.9 \cdot 10^{-3}$ | $[kg \cdot m^2]$ |
| J_{g3} | Third gear inertia | $1.9 \cdot 10^{-3}$ | $[kg \cdot m^2]$ |
| J_{g4} | Fourth gear inertia | $4.9 \cdot 10^{-3}$ | $[kg \cdot m^2]$ |
| J_{hs} | Half shaft inertia | $8.6 \cdot 10^{-5}$ | $[kg \cdot m^2]$ |
| K_{hs} | Half shaft stiffness | 7700 | $[\frac{N \cdot m}{rad}]$ |
| β_{hs} | Half shaft damping coefficient | 47 | $[\frac{N \cdot m \cdot s}{rad}]$ |
| α | Half of the equivalent angular backlash | 0.0105 | $[rad]$ |

Table 2.5: 4 on-board motors powertrains parameters

2.2.3 Powertrains: 2 on-board motors

The most complex model is the 2 on-board powertrains. Indeed, as can be seen from the picture 2.9, there are two open differential, one each axle, to consider the torsional dynamic, connected to the shaft and to the tyre.

The open differential is described with the following equation:

$$\begin{aligned}
 T_{df} - J_{eq,1}\ddot{\theta}_{df} - \frac{\Delta J_{hs}}{4}\Delta\ddot{\theta}_s - (T_{hs,R} + T_{hs,L}) &= 0 \\
 \frac{\Delta J_{hs}}{2}\ddot{\theta}_{df} + J_{eq,2}\Delta\ddot{\theta}_s + T_{hs,R} - T_{hs,L} &= 0
 \end{aligned}
 \tag{2.7}$$

Where $\ddot{\theta}_{df}$ is the angular acceleration of the differential; $\Delta\ddot{\theta}_s$ is the relative angular acceleration between the left and right sun gears; T_{df} is the motor torque at the differential; $T_{hs,R}$ and $T_{hs,L}$ are the motor torque at the right and left half shafts and they are formulated as in equations 2.5; ΔJ_{hs} is the difference between the moments of inertia of the right and left half shaft; $J_{eq,1}$ and $J_{eq,2}$ are two equivalent moment of inertia.

In particular T_{df} is computed as follows:

$$T_{df} = T_m i_t \eta_t \tag{2.8}$$

Where T_m is the electric motor torque obtained by the equation 2.1; i_t and η_t , despite the previous model, are obtained respectively by the product between the gear ratios of the gearbox i_g and the differential i_{df} , and the product between the

gear efficiency of the transmission η_g and differential η_{df} . Moreover, the equivalent mass of inertia $J_{eq,1}$ and $J_{eq,2}$ are described below:

$$\begin{aligned}
 J_{eq,1} &= J_{mgd} + 2J_s + \frac{J_{hs,R} + J_{hs,L}}{2} \\
 J_{eq,2} &= J_s + \frac{J_{hs,R} + J_{hs,L}}{4} + i_p^2 J_p \\
 \Delta J_{hs} &= J_{hs,R} - J_{hs,L} \\
 i_p &= \frac{R_s}{R_p}
 \end{aligned} \tag{2.9}$$

Where $J_{hs,R}$ is the the mass moment of inertia of the right half-shaft, $J_{hs,L}$ is that of the left half-shaft, J_s is that of the sun gear and J_p of the planetary gear. i_p the gear ratio between the solar and planetary gears; lastly, J_{mgd} , the equivalent moment of inertia of the motor, gearbox and differential, is given by:

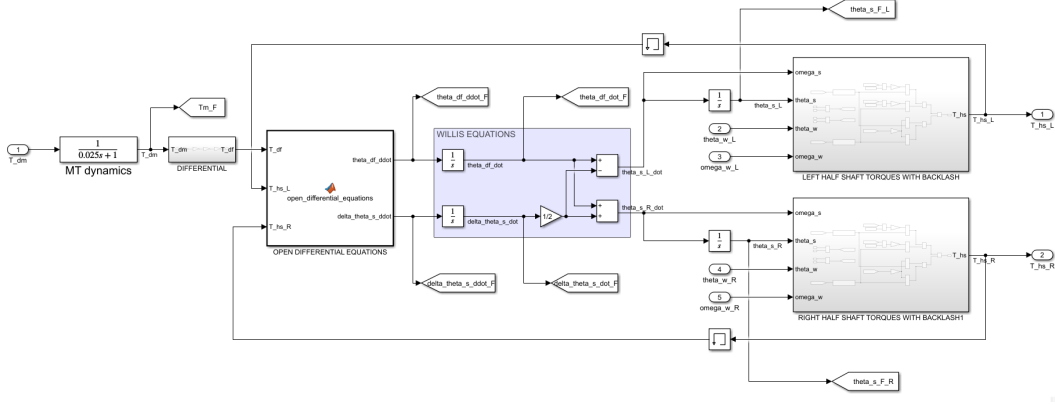
$$J_{mgd} = J_m i_t^2 \eta_t + J_{g1} i_t^2 \eta_t + J_{g2} i_{df}^2 + J_d \tag{2.10}$$

where J_m , J_{g1} and J_{g2} are the individual mass moments of inertia of the motor rotor, gearbox input shaft, gearbox output shaft, and differential case.

To completely describe the open differential dynamics, the Willis equations have to be introduced. They describe the relation between the left and right part of the shaft by considering the angular velocity of the differential $\dot{\theta}_{df}$ and the difference between the angular velocities of the left and right half shafts $\Delta\dot{\theta}_s$:

$$\begin{aligned}
 \dot{\theta}_{s,L} &= \dot{\theta}_{df} - \frac{1}{2} \Delta\dot{\theta}_s \\
 \dot{\theta}_{s,R} &= \dot{\theta}_{df} + \frac{1}{2} \Delta\dot{\theta}_s
 \end{aligned} \tag{2.11}$$

As in the previous case, the following picture shows the implementation on simulink.


Figure 2.13: 2 on-board motors implementation on Simulink

Below, are shown the main values used to model the vehicle:

| Parameter | Description | Value | Unit |
|----------------|---|---------------------|---------------------------------|
| i_g | Gear ratio of the gearbox | 1.746 | [-] |
| i_{df} | Gear ratio of the differential | 4.6 | [-] |
| η_g | Efficiency of the gearbox | 0.98 | [-] |
| η_{df} | Efficiency of the differential | 0.98 | [-] |
| J_{g1} | First gear inertia | $1.9 \cdot 10^{-3}$ | $[kg \cdot m^2]$ |
| J_{g2} | Second gear inertia | $4.9 \cdot 10^{-3}$ | $[kg \cdot m^2]$ |
| J_d | Differential inertia | $6.5 \cdot 10^{-2}$ | $[kg \cdot m^2]$ |
| J_s | Sun gear inertia | $2.9 \cdot 10^{-3}$ | $[kg \cdot m^2]$ |
| J_p | Planetary gear inertia | $2.4 \cdot 10^{-3}$ | $[kg \cdot m^2]$ |
| $J_{hs,L}$ | Left half shaft inertia | $8.6 \cdot 10^{-5}$ | $[kg \cdot m^2]$ |
| $J_{hs,R}$ | Right half shaft inertia | $1.3 \cdot 10^{-4}$ | $[kg \cdot m^2]$ |
| R_s | Sun gear radius | 0.055 | $[m]$ |
| R_p | Planetary gear radius | 0.051 | $[m]$ |
| $K_{hs,L}$ | Left half shaft stiffness | 7700 | $\frac{N \cdot m}{rad}$ |
| $K_{hs,R}$ | Right half shaft stiffness | 7700 | $\frac{N \cdot m}{rad}$ |
| $\beta_{hs,L}$ | Left half shaft damping coefficient | 47 | $\frac{N \cdot m \cdot s}{rad}$ |
| $\beta_{hs,R}$ | Right half shaft damping coefficient | 49.5 | $\frac{N \cdot m \cdot s}{rad}$ |
| α | Half of the equivalent angular backlash | 0.03 | $[rad]$ |

Table 2.6: 2 on-board motors powertrains parameters

2.2.4 MF-Swift

The performance of vehicles when driving is significantly influenced by the contact interaction between the tyres and the road which is being optimised by automotive experts to ensure that the car handles well and runs smoothly and safely in every situation. An adequate description of the tyre-road contact interactions is necessary for the engineer to analyse how tyre parameters affect the dynamic behaviour of vehicles.

Standard vehicle simulation software, like Matlab or CarSim or CarMaker or VSM, does not include by default sufficiently advanced tire models to allow accurate ride comfort analyses for short wavelength road inputs. Indeed, standard vehicle dynamics simulation models tend to use the conventional Magic Formula model, which is very appropriate for accurate longitudinal and lateral tire force computation for vehicle dynamics analysis, but does not include neither a tire enveloping model, describing the processes occurring at the tire contact patch in case of short wavelength road irregularities, nor a dynamic model of the tire structure, to achieve a good match with ride comfort experimental results in the relevant frequency range.

Therefore, in this study a dedicated advanced tire simulation software for ride comfort analyses was used, i.e., MF-Swift, commercialized by Siemens, which was interfaced with a vehicle model implemented in Matlab/Simulink. The MF-Swift model conjugates the Pacejka magic formula model for tangential tire force computation, with appropriate enveloping and tire structure models. MF-Swift has been extensively validated through experiments for a variety of conditions by its developers. Its semi-empirical approach enables fast and robust tire-road contact force and moment simulation for steady-state and transient behavior up to 100 Hz, which makes it suitable for:

- vehicle handling simulations including parking maneuvers;
- vehicle control prototyping (e.g. ABS / ESC);
- rollover analysis;
- ride comfort analysis;
- durability analysis.

Its main elements [48]-[49] are:

- The elastically suspended rigid ring model, with six degrees of freedom, that represents the tire sidewalls and belt with the respective mass and inertial properties; the rigid ring describes the primary vibration modes of the tire belt, connected to the rim by means of springs and dampers, and its inertial,

centrifugal, and gyroscopic effects are taken into account, which permits to accurately model the tire dynamic behavior also in a higher frequency range;

- the residual stiffness and damping models. These have been introduced between the contact patch and the rigid ring to ensure realistic modeling of the total quasi-static tire stiffness in vertical, longitudinal, lateral and yaw directions. The total tire model compliance is based on the carcass (ring suspension) compliance, the residual compliance (in reality a part of the total carcass compliance), and the tread compliance;
- the contact patch model, which features horizontal tread element compliance and partial sliding. Based on this model, the effects of the finite length and width of the footprint are approximately included;
- the magic Formula steady-state tire slip model, describing the nonlinear slip force and moment properties, which enables accurate response for handling maneuvers.

The previous models allow to represent the main features determining the transient response of a tire, namely the flexibility of the tire carcass, the length of the contact patch, and the mass and mass moments of inertia of the belt. Moreover, MF-Swift includes the temperature and velocity model (disabled within the specific analysis of this study) developed by Lugaro et al. [50]-[51], where:

- The thermodynamic model predicts the evolution of the temperature profile and inflation pressure;
- the effect of the tire temperature and rolling speed are then captured through appropriate Magic Formula scaling factors.

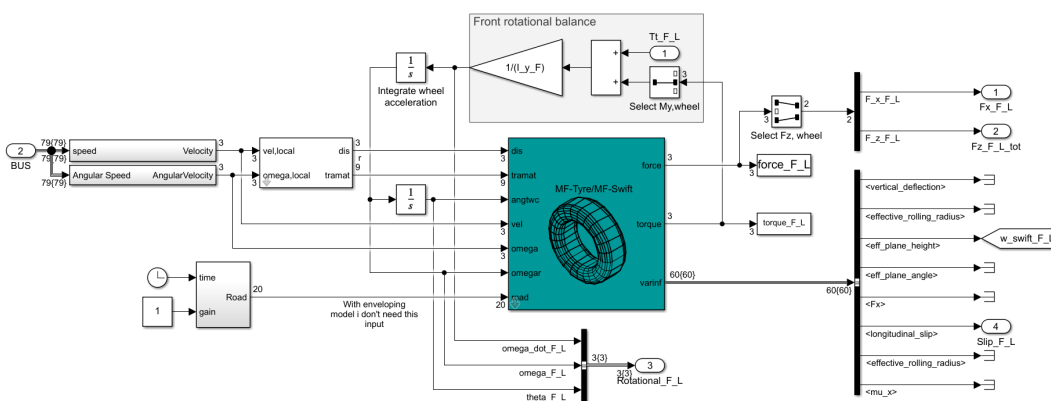


Figure 2.14: MF-Swift

2.2.5 Anti-properties

Any vehicle will typically feel a longitudinal force at its centre of gravity due to longitudinal accelerations. The suspension springs and dampers are primarily responsible for responding to this force, which will cause the car to pitch. Three separate expressions, *Lift*, *Squat*, and *Dive*, are developed to distinguish between various vehicle pitches.

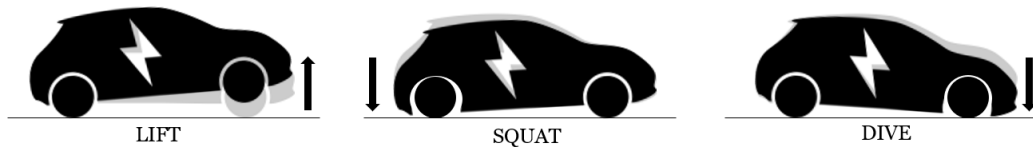


Figure 2.15: Anti-properties

An opposing force must be supplied to the centre of gravity in order to stop this rotation from occurring or to reduce its intensity. The *suspension anti-properties mechanism* is how this system is known as. The location of the castor pole in relation to the centre of the wheel regulates how much anti-dive or anti-lift is present in a suspension system. Below, a front suspension's anti-dive and anti-lift angles are displayed.

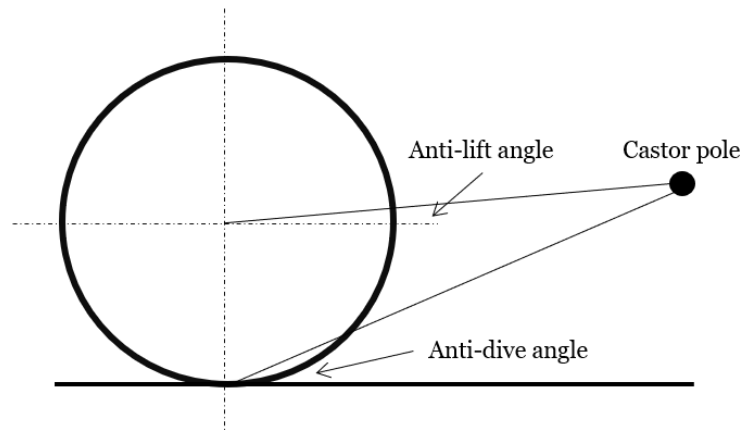


Figure 2.16: Anti-dive and Anti-lift angle

Additionally, percentages are used to indicate this type of value. The anti properties are expressed mathematically as follows. First, let's consider the sprung and unsprung masses all together and assume the car to be symmetric between its left and right part (e.g. $F_{x,R} = F_{x,R,L} = F_{x,R,R}$ and $F_{x,F} = F_{x,F,L} = F_{x,F,R}$).

The longitudinal dynamics can be described through the following equation

$$F_{x,R} + F_{x,F} = m_h \ddot{x}_b$$

where:

- m_h is half of the total car mass, and it's calculated as

$$m_h = \frac{1}{2}(m_b + 2m_{u,R} + 2m_{u,F}) \quad (2.12)$$

where m_b is the sprung mass, $m_{u,R}$ and $m_{u,F}$ are the rear and front unsprung masses, respectively.

- \ddot{x}_b is the longitudinal acceleration of the sprung mass.
- $F_{x,R}$ and $F_{x,F}$ are the longitudinal interaction forces between the wheels and the road, and they can be formulated as follows

$$\begin{aligned} F_{x,R} &= (1 - p)\ddot{x}_b \\ F_{x,F} &= p\ddot{x}_b \end{aligned} \quad (2.13)$$

where p is the *front to total distribution*.

An important aspect are the angles ϕ_R and ϕ_F of the equivalent arms, which are the main factors that allow the pitch in a vehicle:

$$\begin{aligned} \tan \phi_R &= AP_R \frac{h_g}{(1 - p_i)L} \\ \tan \phi_F &= AP_F \frac{h_g}{p_i L} \end{aligned} \quad (2.14)$$

where:

- AP_R and AP_F are the anti-properties percentage, with $0 < AP_R, AP_F < 1$, and they are a trade-off between comfort and pitch attenuation;
- h_g is the height of the centre of gravity (COG);
- p_i is the front to total distribution assumed for the suspension installation;
- L is the wheelbase.

Moreover, the amount of load transfer that is transmitted to the equivalent rigid arm is function of the angles of the equivalent arms:

$$\begin{aligned} F_{z,R,AP} &= F_{x,R} \tan \phi_R \\ F_{z,F,AP} &= F_{x,F} \tan \phi_F \end{aligned} \quad (2.15)$$

where $F_{x,R}$ and $F_{x,F}$ has been introduced in equations 2.13, while $\tan \phi_R$ and $\tan \phi_F$ in equations 2.14.

Starting from static condition, the vertical force applied to the sprung mass can be divided in two components:

$$\begin{aligned} F_{z,R} &= -F_{z,lt} + F_{z,R,AP} \\ F_{z,F} &= F_{z,lt} - F_{z,F,AP} \end{aligned} \quad (2.16)$$

where:

- $F_{z,lt} = m_h \ddot{x}_b \frac{h_g}{L}$ is the total load transfer;
- $F_{z,R,AP}$ and $F_{z,F,AP}$ are the forces introduced in equations 2.15.

By summing the front and rear forces (eq. 2.16), the total vertical force applied to the sprung mass can be expressed as:

$$\begin{aligned} F_{z,b} &= F_{z,R} + F_{z,F} \\ &= -F_{z,lt} + F_{z,R,AP} + F_{z,lt} - F_{z,F,AP} \\ &= F_{z,R,AP} - F_{z,F,AP} \\ &= F_{x,R} \tan \phi_R - F_{x,F} \tan \phi_F \\ &= (1 - p) \ddot{x}_b \tan \phi_R - p \ddot{x}_b \tan \phi_F \end{aligned} \quad (2.17)$$

In addition, by multiplying the front and rear forces (eq. 2.16) for the semi-wheelbases, a momentum is generated respect to the COG:

$$\begin{aligned} M_{z,b} &= F_{z,F}a - F_{z,R}b \\ &= (F_{z,lt} - F_{z,F,AP})a - (-F_{z,lt} + F_{z,R,AP})b \\ &= \left(m_h \ddot{x}_b \frac{h_g}{L} - F_{x,F} \tan \phi_F \right) a - \left(-m_h \ddot{x}_b \frac{h_g}{L} + F_{x,R} \tan \phi_R \right) b \\ &= m_h \ddot{x}_b h_g - F_{x,F} \tan \phi_F a - F_{x,R} \tan \phi_R b \\ &= m_h \ddot{x}_b h_g - p \ddot{x}_b \tan \phi_F a - (1 - p) \ddot{x}_b \tan \phi_R b \end{aligned} \quad (2.18)$$

In the following table are shown the main values used.

| Parameter | Description | Value | Unit |
|-----------|--|-------|------|
| p | Front to total distribution | 0.5 | [-] |
| p_i | Front to total distribution installation | 0.5 | [-] |
| AP_R | Anti-properties rear percentage | 0.05 | [-] |
| AP_F | Anti-properties front percentage | 0.05 | [-] |

Table 2.7: Anti-properties

2.2.6 Rotational dynamics

As already explained, the rotational dynamics of the unsprung masses is integrated in the MF-Swift system. Given the road profile, it returns the wheel-road interaction forces and it calculates the angular acceleration and consequently the angular velocity and angular displacement. The remaining rotational dynamics of the full vehicle is related to the sprung mass. The rotation of a vehicle, respect the transverse axis, is called pitch.

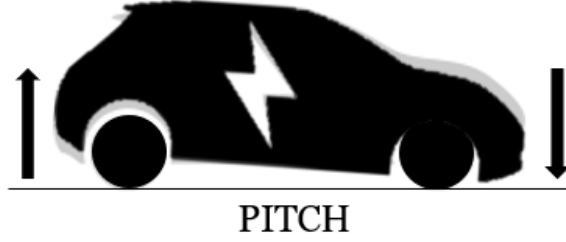


Figure 2.17: Pitch

The used formula of the model, take care about different forces:

$$\begin{aligned} \ddot{\theta}_b = & [(F_{k,z,R,L} + F_{c,z,R,L} + F_{k,z,R,R} + F_{c,z,R,R})b + \\ & - (F_{k,z,F,L} + F_{c,z,F,L} + F_{k,z,F,R} + F_{c,z,F,R})a + \\ & - (F_{k,x,R,L} + F_{c,x,R,L} + F_{k,x,R,R} + F_{c,x,R,R} + \\ & + F_{k,x,F,L} + F_{c,x,F,L} + F_{k,x,F,R} + F_{c,x,F,R})h_g + \\ & + M_{z,b,AP}] \cdot \frac{1}{I_{b,y}} \end{aligned}$$

Where the forces $F_{k,z}$ and $F_{c,z}$ are referred to the vertical suspension forces, associated with the sprung and shock absorbed. In particular the first one represents the vertical spring force and is formulated as follows:

$$\begin{aligned} F_{k,z,R,L} &= K_z \epsilon_{z,R,L} = K_z (z_b - \theta_b b - z_{u,R,L}) \\ F_{k,z,R,R} &= K_z \epsilon_{z,R,R} = K_z (z_b - \theta_b b - z_{u,R,R}) \\ F_{k,z,F,L} &= K_z \epsilon_{z,F,L} = K_z (z_b + \theta_b a - z_{u,F,L}) \\ F_{k,z,F,R} &= K_z \epsilon_{z,F,R} = K_z (z_b + \theta_b a - z_{u,F,R}) \end{aligned} \tag{2.19}$$

Here, K_z is the vertical suspension stiffness, z_b is vertical position of the COG of the sprung mass, that is unique, and z_u is the vertical displacement of each unsprung mass, θ_b is the pitch angle, b and a are respectively the rear and front semi-wheelbase.

$F_{c,z}$, instead, is computed by considering the following formula that approximates the passive damper behaviour:

$$\begin{aligned}
 F_{c,z,R,L} &= \beta_{z,R}(\dot{\epsilon}_z)\dot{\epsilon}_{z,R,L} = \beta_{z,R}(\dot{\epsilon}_z)(\dot{z}_b - \dot{\theta}_b b - \dot{z}_{u,R,L}) \\
 F_{c,z,R,R} &= \beta_{z,R}(\dot{\epsilon}_z)\dot{\epsilon}_{z,R,R} = \beta_{z,R}(\dot{\epsilon}_z)(\dot{z}_b - \dot{\theta}_b b - \dot{z}_{u,R,R}) \\
 F_{c,z,F,L} &= \beta_{z,F}(\dot{\epsilon}_z)\dot{\epsilon}_{z,F,L} = \beta_{z,F}(\dot{\epsilon}_z)(\dot{z}_b + \dot{\theta}_b a - \dot{z}_{u,F,L}) \\
 F_{c,z,F,R} &= \beta_{z,F}(\dot{\epsilon}_z)\dot{\epsilon}_{z,F,R} = \beta_{z,F}(\dot{\epsilon}_z)(\dot{z}_b + \dot{\theta}_b a - \dot{z}_{u,F,R})
 \end{aligned} \tag{2.20}$$

In this formula, \dot{z}_b is the vertical speed of the COG of the sprung mass, $\dot{\theta}_b$ is the pitch velocity, b and a are respectively the rear and front semi-wheelbase, and $\beta_{z,R}$ and $\beta_{z,F}$ are the vertical damping coefficient and they are function of the relative vertical speeds between the sprung and unsprung masses and are expressed by the following shape:

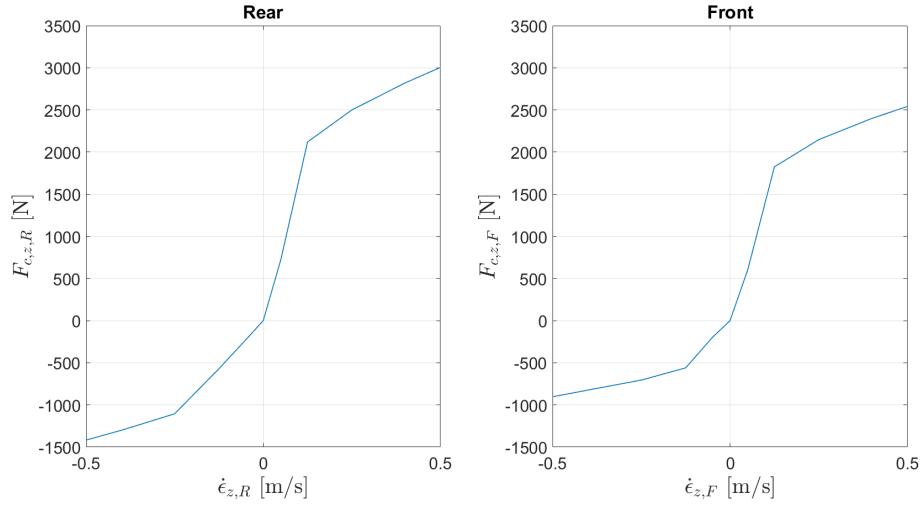


Figure 2.18: Vertical damper forces

Moreover, $F_{k,x}$ and $F_{c,x}$ are the forces associated with the longitudinal compliance of the suspension system; in particular the first one represents the spring forces and is formulated as follows:

$$\begin{aligned}
 F_{k,x,R,L} &= K_x \epsilon_{x,R,L} = K_x(x_b - b - x_{u,R,L}) \\
 F_{k,x,R,R} &= K_x \epsilon_{x,R,R} = K_x(x_b - b - x_{u,R,R}) \\
 F_{k,x,F,L} &= K_x \epsilon_{x,F,L} = K_x(x_b + a - x_{u,F,L}) \\
 F_{k,x,F,R} &= K_x \epsilon_{x,F,R} = K_x(x_b + a - x_{u,F,R})
 \end{aligned} \tag{2.21}$$

There, K_x is the longitudinal suspension stiffness, x_b is the longitudinal displacement of the COG of the sprung mass and x_u represents the longitudinal displacements of the unsprung masses. $F_{c,x}$ is, instead, the damper forces:

$$\begin{aligned}
 F_{c,x,R,L} &= \beta_x \dot{\epsilon}_{x,R,L} = \beta_x(\dot{x}_b - \dot{x}_{u,R,L}) \\
 F_{c,x,R,R} &= \beta_x \dot{\epsilon}_{x,R,R} = \beta_x(\dot{x}_b - \dot{x}_{u,R,R}) \\
 F_{c,x,F,L} &= \beta_x \dot{\epsilon}_{x,F,L} = \beta_x(\dot{x}_b - \dot{x}_{u,F,L}) \\
 F_{c,x,F,R} &= \beta_x \dot{\epsilon}_{x,F,R} = \beta_x(\dot{x}_b - \dot{x}_{u,F,R})
 \end{aligned} \tag{2.22}$$

There β_x is the longitudinal damping coefficient, \dot{x}_b is the longitudinal speed of the sprung mass, and \dot{x}_u represent the longitudinal displacements of the unsprung mass.

The used value are shown below:

| Parameter | Description | Value | Unit |
|-----------|---|--------|------------------------------------|
| K_z | Suspension's vertical stiffness | 33000 | $\left[\frac{N}{m}\right]$ |
| K_x | Suspension's horizontal stiffness | 600000 | $\left[\frac{N}{m}\right]$ |
| β_x | Suspension's horizontal damping coefficient | 1800 | $\left[\frac{N \cdot s}{m}\right]$ |

Table 2.8: Suspensions parameters

2.2.7 Vertical dynamics

The vertical force balance of the sprung and unsprung mass are represented below:

$$\begin{aligned}
 \ddot{z}_b &= [-F_{k,z,R,L} - F_{k,z,R,R} - F_{k,z,F,L} - F_{k,z,F,R} + \\
 &\quad - F_{c,z,R,L} - F_{c,z,R,R} - F_{c,z,F,L} - F_{c,x,F,R} + \\
 &\quad + F_{z,b,AP}] \cdot \frac{1}{m_b} \\
 \ddot{z}_{u,R,L} &= \frac{F_{k,z,R,L} + F_{c,z,R,L} + F_{z,R,L} - F_{z,R,AP}}{m_{u,R}} \\
 \ddot{z}_{u,R,R} &= \frac{F_{k,x,R,R} + F_{c,x,R,R} + F_{z,R,R} - F_{z,R,AP}}{m_{u,R}} \\
 \ddot{z}_{u,F,L} &= \frac{F_{k,x,F,L} + F_{c,x,F,L} + F_{z,F,L} + F_{z,F,AP}}{m_{u,F}} \\
 \ddot{z}_{u,F,R} &= \frac{F_{k,x,F,R} + F_{c,x,F,R} + F_{z,F,R} + F_{z,F,AP}}{m_{u,F}}
 \end{aligned} \tag{2.23}$$

The first equation represent the vertical force balance of the sprung mass, where m_b is the total sprung mass and the forces $F_{k,z}$ and $F_{c,z}$ are introduced already in 2.19 and 2.20; $m_{u,R}$ is the relevant unsprung mass of the rear and $m_{u,F}$ refers to the front unsprung mass.

Two new forces are introduced; $F_{z,R,AP}$ and $F_{z,F,AP}$ are the forces of the anti-properties, introduced in equations 2.15; F_z is is the vertical component of the braking/traction force of the tire, computed with MF-swift without the weight component:

$$\begin{aligned}
 F_{z,R,L} &= F_{z,R,L,tot} - \frac{1}{2}mg\frac{a}{L} \\
 F_{z,R,R} &= F_{z,R,R,tot} - \frac{1}{2}mg\frac{a}{L} \\
 F_{z,F,L} &= F_{z,F,L,tot} - \frac{1}{2}mg\frac{b}{L} \\
 F_{z,F,R} &= F_{z,F,R,tot} - \frac{1}{2}mg\frac{b}{L}
 \end{aligned}$$

2.2.8 Longitudinal dynamics

In the end, the last dynamics that has been considered is the longitudinal dynamics of the sprung and unsprung masses that is described by the following equations:

$$\begin{aligned}
 \ddot{x}_b &= [-F_{k,x,R,L} - F_{k,x,R,R} - F_{k,x,F,L} - F_{k,x,F,R} + \\
 &\quad - F_{c,x,R,L} - F_{c,x,R,R} - F_{c,x,F,L} - F_{c,x,F,R} + \\
 &\quad - F_{drag}] \frac{1}{m_b} \\
 \ddot{x}_{u,R,L} &= \frac{F_{k,x,R,L} + F_{c,x,R,L} + F_{x,R,L}}{m_{u,R}} \\
 \ddot{x}_{u,R,R} &= \frac{F_{k,x,R,R} + F_{c,x,R,R} + F_{x,R,R}}{m_{u,R}} \\
 \ddot{x}_{u,F,L} &= \frac{F_{k,x,F,L} + F_{c,x,F,L} + F_{x,F,L}}{m_{u,F}} \\
 \ddot{x}_{u,F,R} &= \frac{F_{k,x,F,R} + F_{c,x,F,R} + F_{x,F,R}}{m_{u,F}}
 \end{aligned} \tag{2.24}$$

As for the vertical dynamics, the first equation describes the vertical dynamics of the sprung mass and the other four equations, the vertical dynamics of the unsprung masses. Here, the longitudinal forces were already introduced in 2.21. In the formula there is also the longitudinal component of the force of the tire, F_x , computed through MF-Swift.

Moreover, F_{drag} is the aerodynamic drag force and it's calculated as

$$F_{drag} = \frac{1}{2} \rho_{air} C_d A_{car} \dot{x}_b^2 \tag{2.25}$$

where ρ_{air} is the air density, C_d is the aerodynamics drag coefficient, A_{car} is the vehicle's frontal area and \dot{x}_b is the longitudinal speed of the vehicle.

Chapter 3

Non-Linear MPC

3.1 Introduction

As told in the previous chapter, the reduction of longitudinal acceleration caused by road irregularities is not much covered in literature. In [52], Fukudome suggests a controller based on the difference in longitudinal speed between the unsprung and sprung masses in a vehicle with in-wheel powertrains. Bakirci et al. use a PI controller in [53], in which, due to the use of an internal combustion engine, the advantages of its use are neglected. A controller which considers both feed-forward and feedback contribution is proposed in [54]; the feedback contribution considers a dead-time compensator observer to provide robustness against communications delays, and the controller is tuned by considering the model [55]. However, since the road is unknown, this method focuses not on the suppression of the oscillation due to the road irregularities, but on the suppression of vibrations caused by in-wheel motor torque transients. Walz et al., in [56] and [57], propose a feed-forward controller able to reduce the longitudinal acceleration oscillation only over a known road profile, a step test, during speed lower than 10 km/h. In particular, in the second paper, the controller is able to compute actuation of the engine and friction brake to achieve the torque demand. The article [54], proposed by Yamada et al, focused on the active suppression of resonant modes in the high frequency (3–25 Hz) by proposing a model-based longitudinal acceleration control for a vehicle with in-wheel motors. In particular the control method is composed of three main components: an FF controller for torque input, a FB controller and a dead-time compensated state observer. The performances are confirmed by the comparison with benchmark feedback controller in [52]. V. Vidal et al, in [58], propose an innovative nonlinear model predictive control formulation to compensate the longitudinal acceleration caused by irregular road profile; indeed the study is based on a pre-emptive control system, that considers ahead the

road profile of the expected path, by acting on the torque of 4 different in-wheel motors of a full electric vehicle. The NMPC formulations with road preview, across different road profiles such as uneven road or a step, achieve a good compensation of the longitudinal acceleration peaks.

In conclusion, the previous analysis highlights how a predictive control that uses electric powertrains to compensate the effect of the longitudinal dynamics of the vehicle of road irregularities is rarely used; the most innovative aspect of this study is not only the pre-emptive model, not yet analyzed in the literature, but above all its use with on-board powertrains. This thesis shows that MPCs, controlling different power-trains, can reduce these oscillations.

3.1.1 Acado toolkit

There have been an exponentially growing number of applications over the past few decades where control approaches based on dynamic optimization have increased performance. In such sophisticated controllers, the main algorithmic step is the numerical solution of optimal control problems. The open-source tool IPOPT, a MATLAB package called PROPT, NEWCON, OptCon, and other optimization algorithms have all been built for handling this problem, according to a literature search. Each of the mentioned packages has distinct advantages, and they have all demonstrated success in a certain set of applications. Which one is best depends typically on the nature of the problem at hand because they are all specialized to a certain set of underlying numerical methods. Furthermore, it is challenging to mix algorithmic ideas from several packages or to augment them with new mathematical ideas due to their specific software architecture. The ACADO Toolkit was created to address the following four essential characteristics, which, in addition to ensuring an implementation's functionality and effectiveness, are, in the authors' opinion, essential for software packages for automated control based on dynamic optimization [59].

The ACADO Toolkit is an algorithm library and software environment for autonomous control and dynamic optimization. It offers a broad framework for utilizing a wide range of direct optimum control techniques, such as model predictive control, state and parameter estimation, and robust optimization. The ACADO Toolkit has a user-friendly MATLAB interface and is built as self-contained C++ code. The object-oriented architecture makes it possible to enhance it with user written optimization procedures and to conveniently couple it with already-existing optimization packages[60].

While discussing them, we also sketch how they are addressed within the ACADO Toolkit:

- **Open-source:** For researchers to be able to replicate all results, verify that

everything is implemented as stated, and test out their own improvements, the package must at the very least be publicly available to academic users.

- **User-friendliness:** Optimal control problem formulation syntax should be as simple as possible. This could simply be a matter of convenience for expert users. However, considering the increasing prevalence of dynamic optimization in several engineering applications, even non-experts need to be able to construct their control issues within a respectable amount of time. Whenever possible, the program should also choose appropriate setup and algorithmic parameters on its own if the user does not offer them.
- **Code extensibility:** The software should be designed in a way that makes it possible to expand the package while also meeting some criteria. It should be simple to link together already-developed algorithms. It should act as a foundation for future developments without duplicating existing code. Modularity can help with this to some level as long as efficiency is not compromised.
- **Self-containedness:** The use of additional packages should be optional, and the primary package should include a mode to operate stand-alone. The program should only depend on external packages if doing so is truly unavoidable. Due to the fact that model predictive controllers frequently use them, this capability is especially important for embedded hardware applications. On the one hand, linking against these packages could not even be possible, for instance if they depend on other compilers that are not supported by the hardware or if linking against external packages is just not supported. On the other hand, even if linking is feasible, integrating normally huge external packages greatly expands the executable's size and adds to the work required to maintain the product. Finally, complex software license difficulties might emerge from mixing several programs.

The basic structure of ACADO is outlined in Figure 3.1 .
Its features are the following.[61]

- **Direct optimal control methods :** Only Single Shooting (Sargent and Sullivan, 1978) and Multiple Shooting (Bock and Plitt,1984) are accessible in the current version of ACADO. Both approaches are direct methods that convert the optimal control problem into a NLP using the first discretize then optimize guiding principle. Numerous limitations exist when using single shooting to answer boundary value issues numerically; as a result, multiple shooting is typically employed to resolve boundary value problems;
- **Integration and collocation methods :** For ordinary differential equation (ODE) systems, a variety of integration techniques are available, such as the

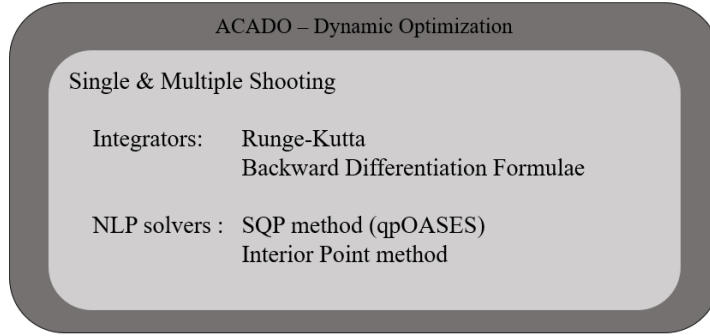


Figure 3.1: Acado feature

Runge-Kutta type integrators (RK12 (adaptive Euler), RK23 (second order), RK45 (Dormand-Prince), or RK78 (Dormand-Prince));

- **Optimisation routines** : Sequential quadratic programming (SQP) and interior point approaches can be used as optimization procedures. For both the QP sequences produced by SQP-type techniques and linear MPC, the ACADO Toolkit employs qpOASES as its default QP solver [62].

3.1.2 Enveloping model and preview

In order to better estimate the effective road profile, which in the plant is calculated by MFSwift, and to achieve a suitable balance between precision and computing effort, Schmeitz’s tandem enveloping model with elliptical cams [63] is employed in the controller implementation. The model produces the effective road profile, which is determined external to the NMPC, provided as an external input, or online data, to the controller and specified as w and β_y . The tire-road contact model, as shown in the figure 3.2, is composed of two moving, rigid and identical ellipses. Accordingly to the wheel, they move longitudinally without rotating, and, accordingly to the road profile, they independently translate vertically, and maintain a fixed horizontal distance l_s .

At P_0 , which is perpendicular to the center of the wheel, the effective road profile is determined. Taking into account the front and rear ellipses’ vertical centers as a starting point, $Z_{e,F}$ and $Z_{e,R}$ (fig. 3.2) the effective road profile parameters w and β_y , which relate to the longitudinal wheel position x_u , are given by:

$$\begin{aligned} w(x_u) &= \frac{Z_{e,F} + Z_{e,R}}{2} - b_c \\ \tan\beta_y(x_u) &= \frac{Z_{e,F} - Z_{e,R}}{l_s} \end{aligned} \tag{3.1}$$

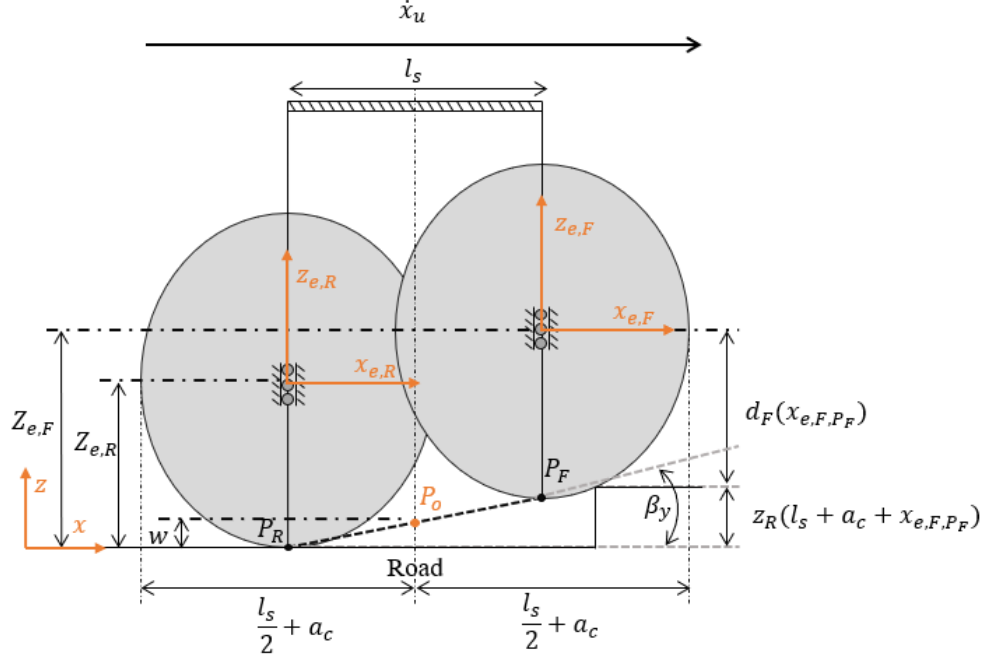


Figure 3.2: Enveloping model

where b_c is the vertical ellipses' semi-axis. By writing the front ellipse's equation:

$$\left(\frac{x_{e,F}}{a_c}\right)^2 + \left(\frac{z_{e,F}}{b_c}\right)^2 = 1$$

where a_c is the horizontal ellipse's semi-axis, c is the ellipse shape parameter, $x_{e,f}$ and $z_{e,f}$ are the front ellipse's local axis system. It is possible to describe the vertical gap, d_F , between the front ellipse's center and its bottom edge, as a function of $x_{e,F} \in [-a_c, a_c]$:

$$d_F(x_{e,F}) = b_c \left\{ 1 - \left[\frac{|z_{e,F}|}{a_c} \right]^c \right\}^{\frac{1}{c}}$$

The corresponding distance for the rear ellipse d_r is calculated using similar methods. $Z_{e,F}$ and $Z_{e,R}$, i.e. the highest values of the combination of the road height z_R and the distances d_F and d_R over the feasible range for $x_{e,F}$ and $x_{e,R}$, are determined for a given longitudinal wheel coordinate x_u :

$$Z_{e,F} = \max_{x_{e,F} \in [-a_c, a_c]} (z_R(x_u, x_{e,F}) + d_F(x_{e,F}))$$

$$Z_{e,R} = \max_{x_{e,R} \in [-a_c, a_c]} (z_R(x_u, x_{e,R}) + d_R(x_{e,R}))$$

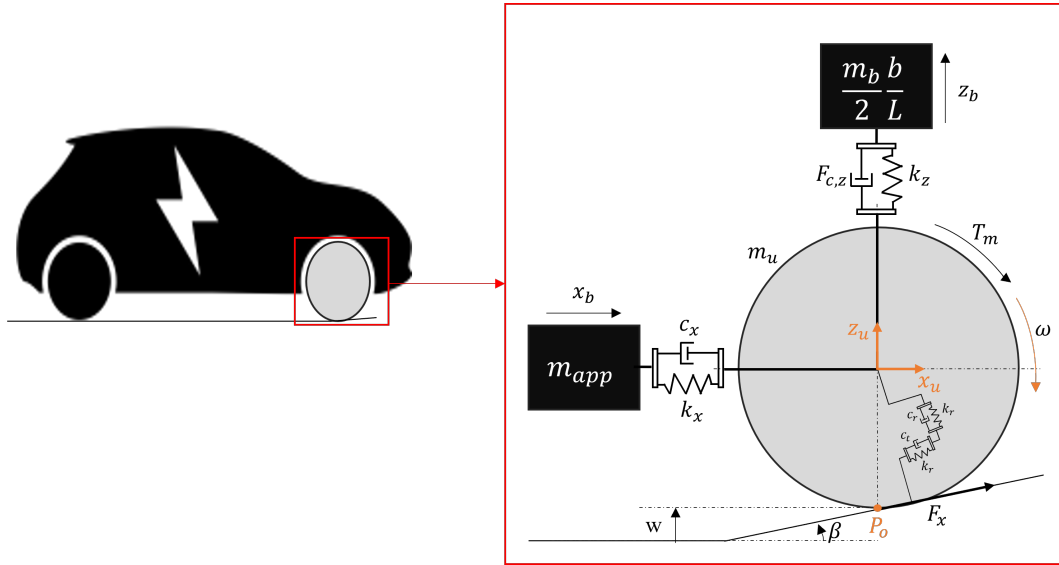


Figure 3.4: Schematic of a corner prediction model

But there is a big difference between the models with 4 motors and the one with only two motors; for the first two models the internal model can be considered as a *quarter-full car model*; this means that, for the vertical dynamics, only one corner of the vehicle is considered at once, while the remaining part's variables and forces are considered as external inputs; meanwhile, for the longitudinal dynamic, the full vehicle is considered. The last one use a *half-full car model*, that, instead, consider half of a vehicle for the vertical dynamics and full for the longitudinal one.

Each prediction model incorporates different dynamics; *quarter-full car model* for in-wheel powertrains can be described as follows:

1. the tire and wheel dynamics;
2. the vertical unsprung mass dynamics;
3. the longitudinal unsprung mass dynamics;
4. the vertical sprung mass dynamics of the corner under consideration;
5. the longitudinal sprung mass dynamics of the entire vehicle.

Moreover, in case of 4 on-board motors, the *quarter-full car prediction model* also contains the torsional dynamics of the shaft. Instead, the 2 on-board model, that is represented by an *half-full car prediction model*, also includes the torsional dynamics of the shafts and the open differential equations.

The system has five degrees of freedom (eight in case of half-full car model) from the perspective of the mechanics of the dynamics of the associated masses

and inertia. Although it can be assumed that the input from the road impacts the sprung mass's longitudinal and vertical dynamics, the prediction model ignores the unsprung masses' longitudinal and vertical dynamics of the vehicle corners that are not taken into account. (three corners in case of quarter-full car model; two corners in case of half-full car model)

| Parameter | Description |
|-----------------|--|
| k_x and c_x | stiffness and damping coefficient to reproduce the effect of the suspension bushings |
| k_r and c_r | stiffness and damping coefficient to reproduce the radial dynamics of the tire |
| k_t and c_t | stiffness and damping coefficient to reproduce the tangential dynamics of the tire |

Table 3.1: Prediction model parameters

3.1.4 Simulation environment

The control schemes of the in-wheel model and 4 on-board model are very similar and can be schematize as in the following figure:

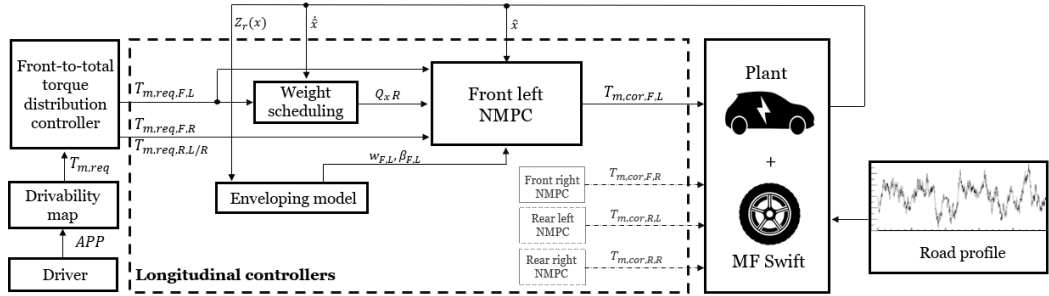


Figure 3.5: Simplified schematic of the simulation and control environment : 4 motors

- The driver block computes the electric motor torque at the EV level, $T_{m,req}$ thanks to an appropriate map, function of the position of the accelerator pedal and vehicle speed. Then, the Front to total torque distribution controller determines, based on powertrain efficiency, the individual reference motor torque values $T_{m,req,i,j}$, as input of the controllers. The notation "i" indicates the front (F) and rear (R) axle, while the notation "j" designates the left (L) or right (R) vehicle side.

- Since the weights of the cost function, Q and R , change depending on the conditions under which the controllers are tested, e.g different road profile, also a weight scheduling block is inserted.

- The enveloping model employed in the controller implementation is used in order to consider the real behaviour of the tire also in the controller by considering, e.g, the capability of the tire to deform when rolling over road irregularities and providing the road displacement, W and β .

- The model-based controllers, the cores of this study, provide $T_{m,cor,i,j}$, explained in detail in 3.2. Each NMPC is presumed to be used in the inverter connected to the corresponding motor. Since the motor sensors are frequently directly hardwired on the inverter, this makes it easier to reduce the system's pure time delays.

- The last block is the nonlinear vehicle model of the plant, designed in MATLAB/Simulink, used for control system assessment. A transfer function formulation is employed to take into account the electromagnetic torque dynamics of the in-wheel machines in the non-linear vehicle model of the plant used for control system assessment. The suspension springs and dampers' non-linearity, the longitudinal compliance properties of the suspension bushings, and the dynamics of sprung and unsprung masses are all considered in the model thanks to MF SWIFT [64]. MATLAB does not include by default sufficiently advanced tire models to allow accurate ride comfort analyses for short wavelength road inputs. Indeed, standard vehicle dynamics simulation models tend to use the conventional Magic Formula model, which is very appropriate for accurate longitudinal and lateral tire force computation for vehicle dynamics analysis, but does not include neither a tire enveloping model, describing the processes occurring at the tire contact patch in case of short wavelength road irregularities, nor a dynamic model of the tire structure, to achieve a good match with ride comfort experimental results in the relevant frequency range. Therefore, in this study MF SWIFT was used.

To better understand how the plant and controllers have been implemented, the figure below shows the Simulink implementation.

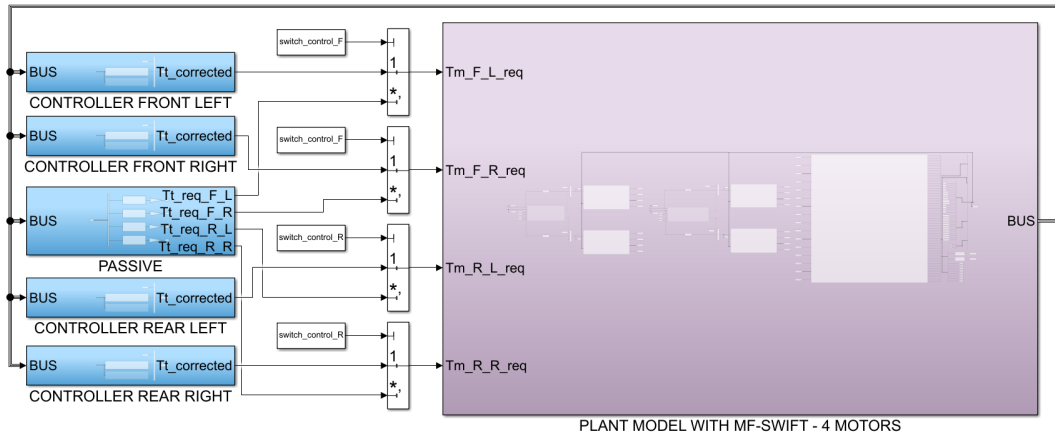


Figure 3.6: Main Simulink layer : 4 motors

This particular scheme is the one used for the vehicle models with in-wheel motors, 2.7, and 4 on-board motors, 2.8. The Simulink block on the right corresponds to the plant model; it is composed by all the equations introduced in chapter 2, 4 MF-Swift blocks, 2.14, the 4 motors blocks 2.11, the half shaft blocks 2.12 and a switching block to switch from the 4 on-board model to the 4 in-wheel one, and vice-versa.

On the left, 4 NMPCs have been developed, one for each motors, connected to 4 switching blocks, to switch between the active and passive plant. The active plant means that the plant model is controlled by the NMPCs; otherwise, the passive plant means that the motor torques of the 4 motors are just the required ones, so the ones chosen by the driver through the pedal, and not the corrected ones.

Each controller block contains two controllers, one for the in-wheel model and one for the 4 on-board model.

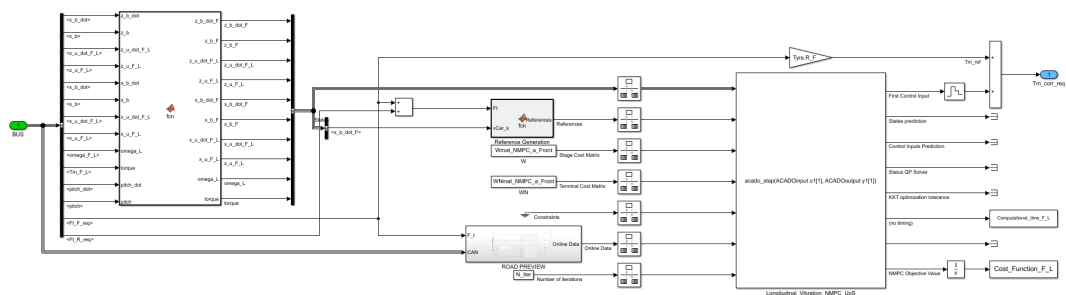


Figure 3.7: Controller layer : in-wheels model

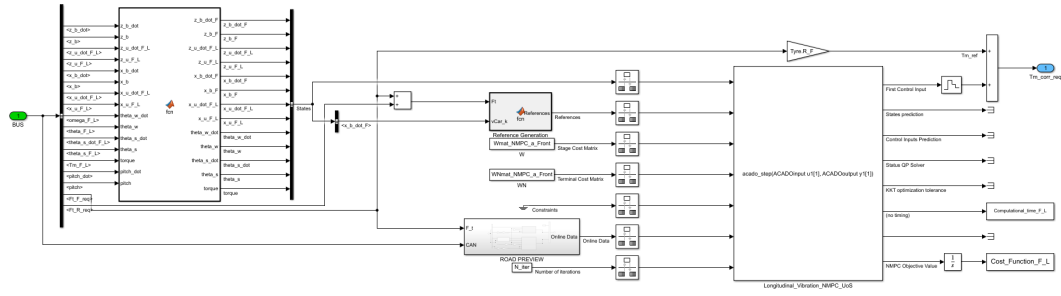


Figure 3.8: Controller layer : 4 on-board model

By comparing both figure, 3.7 and 3.8, the main difference is about the amount of inputs/outputs of the Matlab function on the left. These parameters corresponds to the states of the OCP of the NMPCs. Indeed, in case of 4 onboard models, the presence of the shafts provides the formulations of more states, regarding the torsional dynamics of the shaft. The other blocks, instead, are very similar to each other, because just few parameters change: both the references and the online data depend on the transmission ratio between the motor and the wheel that, in case of in-wheel motors, it's equal to 1, and the online data.

Regarding the online data Simulink block, it includes the required motor torque at the other corners and the road preview, which contains the enveloping model and it is represented as follows:

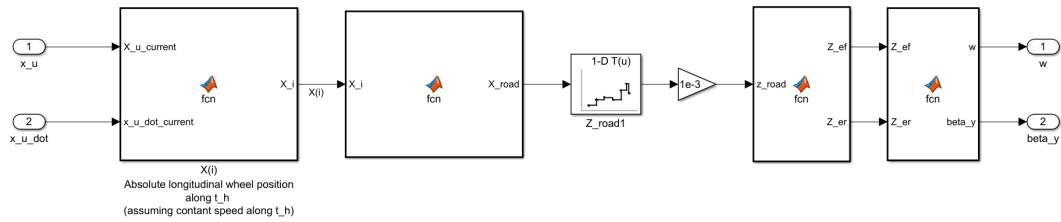


Figure 3.9: Enveloping model : 4 on-board and in-wheel models

This block, thanks to the current position of the considered corner, is able to provide as output ω and β , values explained in the equation 3.1.

The simulation environment for the 2 on-board powertrains is represented below:

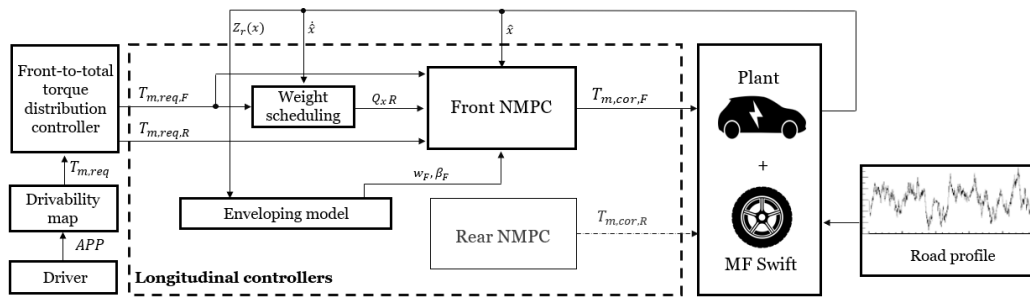


Figure 3.10: Simplified schematic of the simulation and control environment : 2 on-board powertrains

There, can be seen only two different controller, one for the rear and one for the left, due to the presence of the differential that is able to split the motor torque to the corresponding right or left half-shaft.

Below, as for the previous models, is presented the Simulink environment and the controller layer:

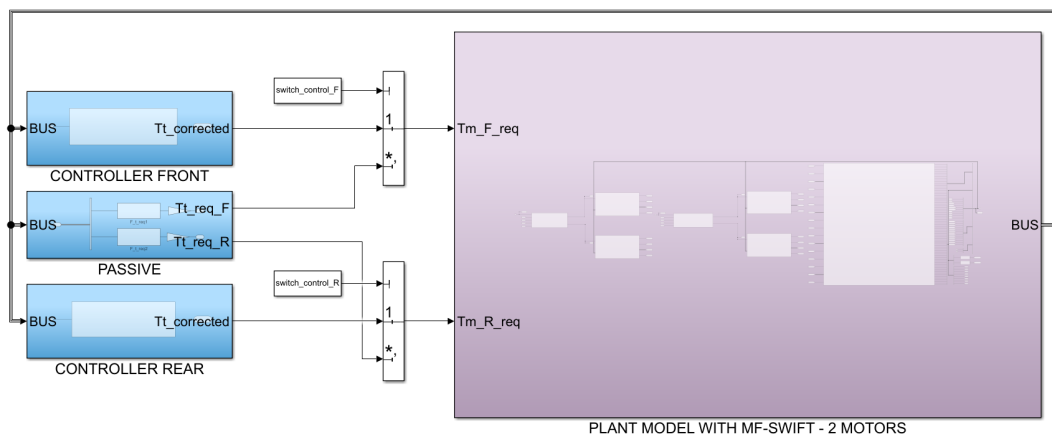


Figure 3.11: Main Simulink layer : 2 on-board model

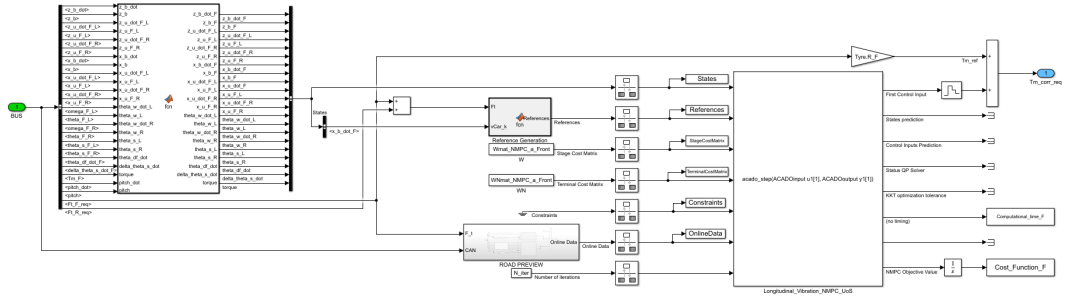


Figure 3.12: Controller layer : 2 on-board model

Also in this case, the Simulink implementation of the NMPC is pretty similar to the previous ones, except for the states and online data; actually, for the states, are considered also the parameters explained in the equation 2.7; for the online data, are provided ω and β for only the front and rear.

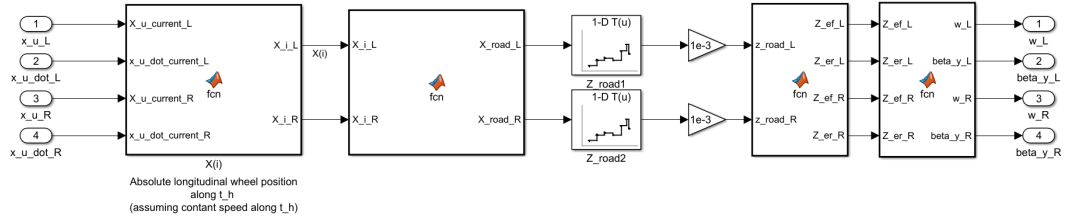


Figure 3.13: Enveloping model: 2 on-board model

3.2 Vehicle with in-wheel motors

Since the motors power the wheel directly, no torsional dynamics of the shaft has to be considered. Due to the presence of 4 motors (fig. 2.7), a MPC for each vehicle's corner that controls its own motor has been implemented. For this reason not all the variables in the system can be considered at once, but only the ones of the considered corner. All the other needed variables are assumed as *online data*.

To define the optimization problem, *states*, *online data*, *control actions* and *constraints* have to be defined. From now on, only the front-left corner will be considered.

The states vector $x_{F,L}$ of the front-left MPC is represented by

$$x_{F,L} = [\dot{z}_{b,F,L} \ z_{b,F,L} \ \dot{z}_{u,F,L} \ z_{u,F,L} \ \dot{x}_{b,F,L} \ x_{b,F,L} \ \dot{x}_{u,F,L} \ x_{u,F,L} \ \dot{\theta}_{u,F,L} \ T_{m,F,L}]^T$$

where:

- $\dot{z}_{b,F,L}$ is the vertical speed of the sprung mass at the front-left wheel

$$\dot{z}_{b,F,L} = \dot{z}_b + a \cdot \dot{\theta}_b$$

where \dot{z}_b is the vertical speed of the sprung mass at its own COG, $\dot{\theta}_b$ is the pitch velocity and a is the front semi-wheelbase;

- $z_{b,F,L}$ is the vertical displacement of the sprung mass at the front-left wheel

$$z_{b,F,L} = z_b + a \cdot \tan \theta_b$$

where z_b is the vertical displacement of the COG of the sprung mass and θ_b is the pitch angle;

- $\dot{z}_{u,F,L}$ is the vertical speed of the front-left unsprung mass;
- $z_{u,F,L}$ is the vertical displacement of the front-left unsprung mass;
- $\dot{x}_{b,F,L} = \dot{x}_b$ is the longitudinal speed of the sprung mass at the front-left wheel and it's equal to the longitudinal speed of the sprung mass at its own COG;
- $x_{b,F,L}$ is the longitudinal displacement of the sprung mass at the front-left wheel

$$x_{b,F,L} = x_b + a$$

where x_b is the longitudinal displacement of the COG of the sprung mass;

- $\dot{x}_{u,F,L}$ is the longitudinal speed of the front-left unsprung mass;
- $x_{u,F,L}$ is the longitudinal displacement of the front-left unsprung mass;
- $\dot{\theta}_{u,F,L}$ is the angular velocity of the front-left unsprung mass;
- $T_{m,F,L}$ is the actual motor torque of the front-left motor.

The control action $u_{F,L}$ is ΔT_m which is the correction of the motor torque, i.e. it corresponds to the difference between the corrected motor torque $T_{m,cor,F,L}$ and the required motor torque $T_{m,req,F,L}$ as follows:

$$T_{m,cor,F,L} = T_{m,req,F,L} + \Delta T_m$$

The online data vector $o_{F,L}$ of the front-left MPC is represented by

$$o_{F,L} = [w_{F,L} \ \beta_{y,F,L} \ T_{m,req,F,L} \ T_{m,req,F,R} \ T_{m,req,R,L} \ T_{m,req,R,R}]^T$$

where:

- $w_{F,L}$ is the individual effective road displacement;
- $\beta_{y,F,L}$ is the individual effective road gradient;

- $T_{m,req,F,L}$, $T_{m,req,F,R}$, $T_{m,req,R,L}$ and $T_{m,req,R,R}$ are the required motor torque of the considered corner (front-left) and the other ones (front-right, rear-left, and rear-right).

In the end, the constraints of this model are only related to the motor torque, which, depending on the motor characteristics, is limited by a maximum and minimum motor torque $T_{m,max}$ and $T_{m,min}$ (table 2.4), as shown below:

$$T_{m,min} \leq T_{m,cor,F,L} \leq T_{m,max}$$

so,

$$T_{m,min} \leq T_{m,req,F,L} + \Delta T_m \leq T_{m,max}$$

and finally, according to the Acado's constraint formulation,

$$\begin{aligned} T_{m,min} - (T_{m,req,F,L} + \Delta T_m) &\leq 0 \\ T_{m,max} - (T_{m,req,F,L} + \Delta T_m) &\geq 0 \end{aligned} \tag{3.2}$$

where $T_{m,min}$ is the lower bound L_{b,T_m} and is equal to $-T_{m,max}$, and $T_{m,max}$ corresponds to the upper bound U_{b,T_m} .

To complete the description of the optimization problem, the internal model has to be introduced.

3.2.1 Internal model

The internal model is a representation of the real plant. In this case, because 4 NMPCs control their own corner, each internal model represent a *quarter-full car model*. This means that, as already said, the states are only the variables of the considered corner and all the other forces/variables are considered as external forces/parameters. Due to the fact that the control method is a *Pyshics-Based MPC*, the internal model is composed by differential equations. Each equation represents a different dynamics, such as the longitudinal dynamics, the vertical one etc.

To completely describe the system, the following differential equations are used:

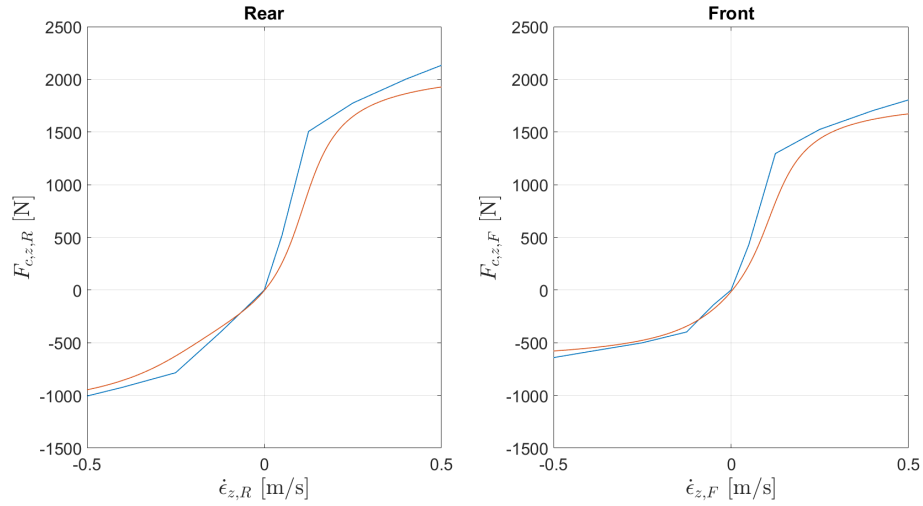
| | | |
|-------------------------|---|-----|
| $\ddot{z}_{b,F,L}$ | $= \left[-F_{k,z,F,L} - F_{c,z,F,L} \right] \cdot \frac{2}{m_b} \frac{L}{b}$ | (1) |
| $\ddot{z}_{u,F,L}$ | $= \frac{F_{k,z,F,L} + F_{c,z,F,L} + F_{r,z,F,L} - F_{t,z,F,L} + F_{x,z,F,L}}{m_{u,F}}$ | (2) |
| $\ddot{x}_{b,F,L}$ | $= \left[-F_{k,x,F,L} - F_{c,x,F,L} + \frac{T_{m,req,F,R}}{R_F} + \frac{T_{m,req,R,L}}{R_R} \right.$ | (3) |
| | $\left. + \frac{T_{m,req,R,R}}{R_R} - F_{drag} - \frac{F_{roll,F}}{2} - F_{roll,R} \right] \cdot \frac{1}{m_{app}}$ | |
| $\ddot{x}_{u,F,L}$ | $= \frac{F_{k,x,F,L} + F_{c,x,F,L} - F_{r,x,F,L} - F_{t,x,F,L} + F_{x,x,F,L}}{m_{u,F}}$ | (4) |
| $\ddot{\theta}_{u,F,L}$ | $= \frac{T_{m,F,L} - F_{x,F,L} \cdot \rho_{F,L} - M_{y,F,L}}{I_{u,F,y}}$ | (5) |
| $\dot{T}_{m,F,L}$ | $= \frac{T_{m,cor,F,L} - T_{m,F,L}}{\tau_m}$ | (6) |

Table 3.2: Differential equations : in-wheel internal model

The first and second equations represent the vertical dynamics of the sprung and unsprung masses (eq. 2.23), where $F_{k,z,F,L}$ is calculated as in eq. 2.19, while $F_{c,z,F,L}$ can't be express through a non-linear function (fig. 2.18) and so, a linear approximation is needed:

$$F_{c,z,F,L} = a_1 + b_1 \arctan(c_1[\dot{z}_{b,F,L} - \dot{z}_{u,F,L}] + d_1) + b_2 \arctan(c_2[\dot{z}_{b,F,L} - \dot{z}_{u,F,L}] + d_2) \quad (3.3)$$

where a_1 , b_1 , b_2 , c_1 , c_2 , d_1 and d_2 are parameters that need to be optimized to better approximate the non-linear function.


Figure 3.14: Non-linear vs linear damper

$F_{r,z,F,L}$ and $F_{t,z,F,L}$ are the vertical components of the radial and tangential

forces related to the tire structure, $F_{r,F,L}$ and $F_{t,F,L}$ and they are formulated as:

$$\begin{aligned} F_{r,z,F,L} &= F_{r,F,L} \cdot \cos \beta_{y,F,L} \\ F_{t,z,F,L} &= F_{t,F,L} \cdot \sin \beta_{y,F,L} \end{aligned} \quad (3.4)$$

where:

$$\begin{aligned} F_{r,F,L} &= k_{r,F}(w_{F,L} - z_{u,F,L}) \cos \beta_{y,F,L} + \beta_{r,F}(\dot{w}_{F,L} - \dot{z}_{u,F,L}) \cos \beta_{y,F,L} \\ F_{t,F,L} &= k_{t,F}(w_{F,L} - z_{u,F,L}) \sin \beta_{y,F,L} + \beta_{t,F}(\dot{w}_{F,L} - \dot{z}_{u,F,L}) \sin \beta_{y,F,L} \end{aligned} \quad (3.5)$$

by assuming that the time derivative of $\beta_{y,F,L}$ is negligible. $F_{x,z,F,L}$ is the vertical component of the traction/braking force of the tire $F_{x,F,L}$, calculated by the Pacejka's magic formula for zero slip angle conditions. Moreover, m_b and $m_{u,F}$ are the sprung and front unsprung masses, L is the wheelbase and b is the rear semi-wheelbase (table 2.1).

Instead, the third and fourth equations represent the horizontal dynamics (eq. 2.24). $F_{k,x,F,L}$ and $F_{c,x,F,L}$ are calculated as in eq. 2.22. $T_{m,req,F,R}$, $T_{m,req,R,L}$ and $T_{m,req,R,R}$ are the required torque of the other motors, already introduced as online data. F_{drag} is the aerodynamic drag force formulated in eq. 2.25, while $F_{roll,F}$ and $F_{roll,R}$ are the front and rear rolling resistance forces and they are given by:

$$\begin{aligned} F_{roll,F} &= f_{roll} m_{tot} \frac{b}{L} g \\ F_{roll,R} &= f_{roll} m_{tot} \frac{a}{L} g \end{aligned} \quad (3.6)$$

where m_{tot} is the total mass and it's formulated as in eq. 2.12, g is the gravity, and f_{roll} is the rolling resistance coefficient given by

$$f_{roll} = f_0 + f_2 \cdot \dot{x}_b^2$$

where f_0 and f_2 are two constant parameters. $F_{r,x,F,L}$ and $F_{t,x,F,L}$ are the longitudinal components of the radial and tangential forces, $F_{r,F,L}$ and $F_{t,F,L}$, and they are given by:

$$\begin{aligned} F_{r,x,F,L} &= F_{r,F,L} \cdot \sin \beta_{y,F,L} \\ F_{t,x,F,L} &= F_{t,F,L} \cdot \cos \beta_{y,F,L} \end{aligned} \quad (3.7)$$

where $F_{r,F,L}$ and $F_{t,F,L}$ are given by eq. 3.5. $F_{x,x,F,L}$ is the longitudinal component of the traction/braking force of the tire $F_{x,F,L}$. Moreover, R_F and R_R are the wheel radius of the front and rear wheels, respectively, and m_{app} is the apparent mass, in which the sprung and unsprung masses, and the moment of inertia of the other corner's wheels are included:

$$m_{app} = m_b + 2m_{u,R} + m_{u,F} + 2 \frac{I_{u,R,y}}{R_R^2} + \frac{I_{u,F,y}}{R_F^2} \quad (3.8)$$

In the end, the fifth and sixth equations describe the rotational dynamics of the front-left unsprung mass, which is given by the MF-Swift package, and the motor dynamics. Here, $T_{m,F,L}$ is actual motor torque, already introduced as state, which differs from the corrected motor torque $T_{m,cor,F,L}$, due to the motor time constant τ_m . In the end, $F_{x,F,L}$ is already well-known forces calculated through the magic formula, $M_{y,F,L}$ is the rolling resistance moment, and $\rho_{F,L}$ is the laden wheel radius.

3.3 Vehicle with 4 on-board motors

As in the other case, four MPCs are developed, each one for its own corner. But, compared to the previous , the torsional dynamics of the shaft is present. Indeed, the main difference between these two models, besides the sprung and unsprung masses and moments of inertia, is about the powertrains. The delayed motor torque T_m no longer acts directly on the wheels, but pass through the transmission shaft, T_{hs} , as shown as shown in fig 2.8. As already known, to define the optimization problem, *states*, *online data*, *control actions* and *constraints* have to be defined.

The states vector $x_{F,L}$ of the front-left MPC is represented by

$$x_{F,L} = [\dot{z}_{b,F,L} \ z_{b,F,L} \ \dot{z}_{u,F,L} \ z_{u,F,L} \\ \dot{x}_{b,F,L} \ x_{b,F,L} \ \dot{x}_{u,F,L} \ x_{u,F,L} \\ \dot{\theta}_{u,F,L} \ \theta_{u,F,L} \ \dot{\theta}_{s,F,L} \ \theta_{s,F,L} \ T_{m,F,L}]^T$$

where:

- $\dot{z}_{b,F,L}$, $z_{b,F,L}$, $\dot{z}_{u,F,L}$, $z_{u,F,L}$, $\dot{x}_{b,F,L}$, $x_{b,F,L}$, $\dot{x}_{u,F,L}$, $x_{u,F,L}$, $\dot{\theta}_{u,F,L}$ and $T_{m,F,L}$ are defined as in the optimization problem of the previous case with in-wheel motors;
- $\theta_{u,F,L}$ is the angular displacement of the front-left unsprung mass;
- $\dot{\theta}_{s,F,L}$ is the angular velocity of the front-left shaft;
- $\theta_{s,F,L}$ is the angular displacement of the front-left shaft.

As in the previous case, the control action $u_{F,L}$ is the correction of the motor torque ΔT_m , and the online data vector $o_{F,L}$ is still represented by

$$o_{F,L} = [w_{F,L} \ \beta_{y,F,L} \ T_{m,req,F,L} \ T_{hs,req,F,R} \ T_{hs,req,R,L} \ T_{hs,req,R,R}]^T$$

where $w_{F,L}$ is the the individual effective road displacement, $\beta_{y,F,L}$ is the individual effective road gradient, $T_{m,req,F,L}$ is the required front-left motor torque, and

$T_{hs,req,F,R}$, $T_{hs,req,R,L}$ and $T_{hs,req,R,R}$ are the required motor torque at the other wheels:

$$\begin{aligned} T_{hs,req,F,R} &= T_{m,req,F,R} \cdot i_{ft,F,R} \\ T_{hs,req,R,L} &= T_{m,req,R,L} \cdot i_{ft,R,L} \\ T_{hs,req,R,R} &= T_{m,req,R,R} \cdot i_{ft,R,R} \end{aligned}$$

where $i_{ft,F,R}$, $i_{ft,R,L}$ and $i_{ft,R,R}$ are the final transmission ratio between the motor and the wheel.

Moreover, also the constraints of this model are only related to the motor torque as in eq. 3.2.

3.3.1 Internal model

As in the previous case, the internal model represents a *quarter-full car model*. This internal model is composed by equations which represent different dynamics, such as the longitudinal, vertical and rotational dynamics of the sprung and unsprung masses, but also the torsional dynamics of the shaft.

$$\begin{aligned} \ddot{z}_{b,F,L} &= [-F_{k,z,F,L} - F_{c,z,F,L}] \cdot \frac{2}{m_b} \frac{L}{b} & (1) \\ \ddot{z}_{u,F,L} &= \frac{F_{k,z,F,L} + F_{c,z,F,L} + F_{r,z,F,L} - F_{t,z,F,L} + F_{x,z,F,L}}{m_{u,F}} & (2) \\ \ddot{x}_{b,F,L} &= [-F_{k,x,F,L} - F_{c,x,F,L} + \frac{T_{hs,req,F,R}}{R_F} + \frac{T_{hs,req,R,L}}{R_R} & (3) \\ &+ \frac{T_{hs,req,R,R}}{R_R} - F_{drag} - \frac{F_{roll,F}}{2} - F_{roll,R}] \cdot \frac{1}{m_{app}} \\ \ddot{x}_{u,F,L} &= \frac{F_{k,x,F,L} + F_{c,x,F,L} - F_{r,x,F,L} - F_{t,x,F,L} + F_{x,x,F,L}}{m_{u,F}} & (4) \\ \ddot{\theta}_{u,F,L} &= \frac{T_{hs,F,L} - F_{x,F,L} \rho_{F,L} - M_{y,F,L}}{I_{u,F,y}} & (5) \\ \ddot{\theta}_{s,F,L} &= \frac{T_{t,F,L} - T_{hs,F,L}}{J_{eq}} & (6) \\ \dot{T}_{m,F,L} &= \frac{T_{m,cor,F,L} - T_{m,F,L}}{\tau_m} & (7) \end{aligned}$$

Table 3.3: Differential equations : 4 on-board internal model

The previous internal model (tab. 3.2) already introduced and explained the equations (1), (2), (4) and (7), shown in tab. 3.3.

The third equation describes the longitudinal dynamics of the sprung mass at the front-left corner. Compared to the other internal model (tab. 3.2), the required motor torques at the other corners, $T_{m,req,F,R}$, $T_{m,req,R,L}$ and $T_{m,req,R,R}$, are substituted by the required motor torques at the wheel, $T_{hs,req,F,R}$, $T_{hs,req,R,L}$ and $T_{hs,req,R,R}$, due to the fact that the motors are no longer positioned on the unsprung masses.

The fifth equation describes the rotational dynamics of the front-left unsprung mass. Compared to the fifth equation of tab. 3.2, the motor torque at the wheel is no longer the actual motor torque $T_{m,F,L}$, but the motor torque at the half shaft $T_{hs,F,L}$, which is formulated as in eq. 2.6. Since non-linear functions are not accepted in NMPC formulations (e.g. fig. 3.14), the switching functions f_1 and f_2 of eq. 2.6 have to be approximate through exponential functions:

$$\begin{aligned} f_1 &= 0.5 \frac{1 - e^{2a \cdot (\alpha - \Delta\theta)}}{1 + e^{2a \cdot (\alpha - \Delta\theta)}} + 0.5 \\ f_2 &= 0.5 \frac{1 - e^{2a \cdot (\alpha + \Delta\theta)}}{1 + e^{2a \cdot (\alpha + \Delta\theta)}} + 0.5 \end{aligned} \quad (3.9)$$

where a is the shape factor of the function; higher is this value, sharper is the shape of the function, but more computationally onerous it becomes. A good trade-off has been selected.

Moreover, α is half of the equivalent backlash, and $\Delta\theta$ is the difference between the angular displacement of the shaft $\theta_{s,F,L}$ and the angular displacement of the unsprung mass $\theta_{u,F,L}$.

The sixth equation represents the torsional dynamics of the shaft (eq. 2.2), where the transmission torque $T_{t,F,L}$ and the half shaft motor torque $T_{hs,F,L}$ are calculated as in eq. 2.3 and eq. 2.6, and the equivalent inertia J_{eq} is given by eq. 2.4.

3.4 Vehicle with 2 on-board motors

This model is much different than the other ones. Indeed, since in this model there are only 2 on-board motors, one for the rear axle and one for the front one (fig. 2.9), only 2 controllers have been developed. Both motors are connected to the wheels through open differentials and half shafts, so the motor torque at the wheel is not T_d , but it's the motor torque at the half shaft T_{hs} . From now on, the front NMPC will be considered.

The states vector x_F of the front controller is represented by

$$\begin{aligned} x_F = & [\dot{z}_{b,F} \ z_{b,F} \ \dot{z}_{u,F,L} \ z_{u,F,L} \ \dot{z}_{u,F,R} \ z_{u,F,R} \\ & \dot{x}_{b,F} \ x_{b,F} \ \dot{x}_{u,F,L} \ x_{u,F,L} \ \dot{x}_{u,F,R} \ x_{u,F,R} \\ & \dot{\theta}_{u,F,L} \ \theta_{u,F,L} \ \dot{\theta}_{u,F,R} \ \theta_{u,F,R} \ \theta_{s,F,L} \ \theta_{s,F,R} \\ & \dot{\theta}_{df,F} \ \Delta\dot{\theta}_{s,F} \ T_{m,F}]^T \end{aligned}$$

where:

- $\dot{z}_{b,F}$ is the vertical speed of the sprung mass at the front axle

$$\dot{z}_{b,F} = \dot{z}_b + a \cdot \dot{\theta}_b$$

where \dot{z}_b is the vertical speed of the sprung mass at its own COG, $\dot{\theta}_b$ is the pitch velocity and a is the front semi-wheelbase;

- $z_{b,F}$ is the vertical displacement of the sprung mass at the front axle

$$z_{b,F} = z_b + a \cdot \tan \theta_b$$

where z_b is the vertical displacement of the COG of the sprung mass and θ_b is the pitch angle;

- $\dot{z}_{u,F,L}$ and $\dot{z}_{u,F,R}$ are the vertical speeds of the front-left and front-right unsprung masses;
- $z_{u,F,L}$ and $z_{u,F,R}$ are the vertical displacements of the front-left and front-right unsprung masses;
- $\dot{x}_{b,F} = \dot{x}_b$ is the longitudinal speed of the sprung mass at the front axle and it's equal to the longitudinal speed of the sprung mass at its own COG;
- $x_{b,F}$ is the longitudinal displacement of the sprung mass at the front axle

$$x_{b,F} = x_b + a$$

where x_b is the longitudinal displacement of the COG of the sprung mass;

- $\dot{x}_{u,F,L}$ and $\dot{x}_{u,F,R}$ are the longitudinal speeds of the front-left and front-right unsprung masses;
- $x_{u,F,L}$ and $x_{u,F,R}$ are the longitudinal displacements of the front-left and front-right unsprung masses;
- $\dot{\theta}_{u,F,L}$ and $\dot{\theta}_{u,F,R}$ are the angular velocities of the front-left and front-right unsprung masses;
- $\theta_{u,F,L}$ and $\theta_{u,F,R}$ are the angular displacements of the front-left and front-right unsprung masses;
- $\theta_{s,F,L}$ and $\theta_{s,F,R}$ are the angular displacements of the front-left and front-right half shafts;
- $\dot{\theta}_{df,F}$ is the angular velocity of the front open differential;

- $\Delta\dot{\theta}_{s,F}$ is the difference between the angular velocities of the front-left and front-right sun gears;
- $T_{m,F}$ is the actual motor torque of the front motor.

As in the other models, the control action u_F is the correction of the motor torque ΔT_m , and the online data vector o_F is still represented by

$$o_F = [w_{F,L} \ \beta_{y,F,L} \ w_{F,R} \ \beta_{y,F,R} \ T_{m,req,F} \ T_{hs,req,R,L} \ T_{hs,req,R,R}]^T$$

where $w_{F,L}$ and $w_{F,R}$ are the the individual effective road displacement, $\beta_{y,F,L}$ and $\beta_{y,F,R}$ are the individual effective road gradient, $T_{m,req,F}$ is the required front motor torque, and $T_{hs,req,R,L}$ and $T_{hs,req,R,R}$ are the required motor torque at the rear wheels:

$$T_{hs,req,R,L} = T_{hs,req,R,R} = T_{m,req,R} \cdot i_{ft,R}$$

where $T_{m,req,R}$ is the required motor torque and $i_{ft,R}$ is the final transmission ratio between the motor and the wheel.

In the end, the constraints of this model are only related to the motor torque as in eq. 3.2.

3.4.1 Internal model

In contrast to the previous models, here only 2 NMPCs have been developed. So, the internal model represents a *half-full car model*.

| | | |
|------------------------------|--|------|
| $\ddot{z}_{b,F}$ | $= \left[-F_{k,z,F,L} - F_{c,z,F,L} - F_{k,z,F,R} - F_{c,z,F,R} \right] \cdot \frac{1}{m_b} \frac{L}{b}$ | (1) |
| $\ddot{z}_{u,F,L}$ | $= \frac{F_{k,z,F,L} + F_{c,z,F,L} + F_{r,z,F,L} - F_{t,z,F,L} + F_{x,z,F,L}}{m_{u,F}}$ | (2) |
| $\ddot{z}_{u,F,R}$ | $= \frac{F_{k,z,F,R} + F_{c,z,F,R} + F_{r,z,F,R} - F_{t,z,F,R} + F_{x,z,F,R}}{m_{u,F}}$ | (3) |
| $\ddot{x}_{b,F}$ | $= \left[-F_{k,x,F,L} - F_{c,x,F,L} - F_{k,x,F,R} - F_{c,x,F,R} \right. \\ \left. + \frac{T_{hs,req,R,L}}{R_R} + \frac{T_{hs,req,R,R}}{R_R} - F_{drag} - F_{roll,R} \right] \cdot \frac{1}{m_{app}}$ | (4) |
| $\ddot{x}_{u,F,L}$ | $= \frac{F_{k,x,F,L} + F_{c,x,F,L} - F_{r,x,F,L} - F_{t,x,F,L} + F_{x,x,F,L}}{m_{u,F}}$ | (5) |
| $\ddot{x}_{u,F,R}$ | $= \frac{F_{k,x,F,R} + F_{c,x,F,R} - F_{r,x,F,R} - F_{t,x,F,R} + F_{x,x,F,R}}{m_{u,F}}$ | (6) |
| $\ddot{\theta}_{u,F,L}$ | $= \frac{T_{hs,F,L} - F_{x,F,L} \cdot \rho_{F,L} - M_{y,F,L}}{I_{u,F,y}}$ | (7) |
| $\ddot{\theta}_{u,F,R}$ | $= \frac{T_{hs,F,R} - F_{x,F,R} \cdot \rho_{F,R} - M_{y,F,R}}{I_{u,F,y}}$ | (8) |
| $\dot{\theta}_{s,F,L}$ | $= \dot{\theta}_{df,F} - \frac{1}{2} \Delta \dot{\theta}_{s,F}$ | (9) |
| $\dot{\theta}_{s,F,R}$ | $= \dot{\theta}_{df,F} + \frac{1}{2} \Delta \dot{\theta}_{s,F}$ | (10) |
| $\ddot{\theta}_{df,F}$ | $= \left[4J_{eq,2,F} T_{df,F} - 4J_{eq,2,F} T_{hs,F,R} - 4J_{eq,2,F} + T_{hs,F,L} \right. \\ \left. + \Delta J_{hs,F} T_{hs,F,R} - \Delta J_{hs,F} T_{hs,F,L} \right] \cdot \frac{2}{8 \cdot J_{eq,1,F} \cdot J_{eq,2,F} - \Delta J_{hs,F}^2}$ | (11) |
| $\Delta \ddot{\theta}_{s,F}$ | $= \left[-2J_{eq,1,F} T_{hs,F,R} + 2J_{eq,1,F} T_{hs,F,L} - \Delta J_{hs,F} + T_{df,F} \right. \\ \left. + \Delta J_{hs,F} T_{hs,F,R} + \Delta J_{hs,F} T_{hs,F,L} \right] \cdot \frac{4}{8 \cdot J_{eq,1,F} \cdot J_{eq,2,F} - \Delta J_{hs,F}^2}$ | (12) |
| $\dot{T}_{m,F,L}$ | $= \frac{T_{m,cor,F,L} - T_{m,F,L}}{\tau_m}$ | (13) |

Table 3.4: Differential equations : 2 on-board internal model

The equations, up to the eighth one and the thirteenth one, have already been explained in the previous internal model (tab. 3.3).

The main difference is that , considering the whole axis of the vehicle, the front-right corner is also implemented in the equations. Moreover, the apparent mass m_{app} has to be changed due to the fact that the internal model describes a *half-full car model*:

$$m_{app} = m_b + 2m_{u,R} + 2 \frac{I_{u,R,y}}{R_R^2}$$

The motor torques at the wheels are represented by $T_{hs,F,L}$ and $T_{hs,F,R}$ which are given by eq. 2.5. Due to the presence of an open differential, the angular velocities and displacements of the left and right half shafts, $\dot{\theta}_{s,F,L}$, $\dot{\theta}_{s,F,R}$, $\theta_{s,F,L}$ and $\theta_{s,F,R}$ are related.

The remaining four equations describe the open differential dynamics. The ninth and tenth equations are the Willis equations shown in eq. 2.11. The eleventh and twelfth equations describe the torsional dynamics of the open differential (eq. 2.7), where the motor torque at the differential is given by eq. 2.8, the front equivalent

moments of inertia $J_{eq,1,F}$ and $J_{eq,2,F}$ are given by eq. 2.9, and $\Delta J_{hs,F}$ corresponds to the difference between the moments of inertia of the front-right and front-left half shaft, $J_{hs,F,R}$ and $J_{hs,F,L}$.

Chapter 4

Results

4.1 Introduction

After having created the plant models and after having developed the NMPCs, the core of the study has begun.

All the simulation have been done through Simulink, with a discretization time of the simulator $T_{s,sim}$ equal to 0.1 ms. Instead, the sampling time of the NMPCs has been set equal to 1 ms.

4.1.1 Internal models' validation

Before making some analyses, the internal models had to be validate. The validation consists on comparing the output of the passive model configuration, \ddot{x}_b , with the predicted output of the internal model, $\ddot{x}_{b,pred}$. The passive model configuration means that the controllers are set off, so the motor torque is not the corrected one $T_{m,cor}$, but only the required one $T_{m,req}$. Moreover, the internal model has to be implemented in open loop. By doing this, when the motor torque changes or the step is encountered, for both the internal model and the plant, the accelerations \ddot{x}_b and $\ddot{x}_{b,pred}$ changes. To check if the internal model has been done well, the predicted curve should be as close as possible to the real one. By optimizing some parameters, such as the ones in tab. 3.1, the internal models have been validate.

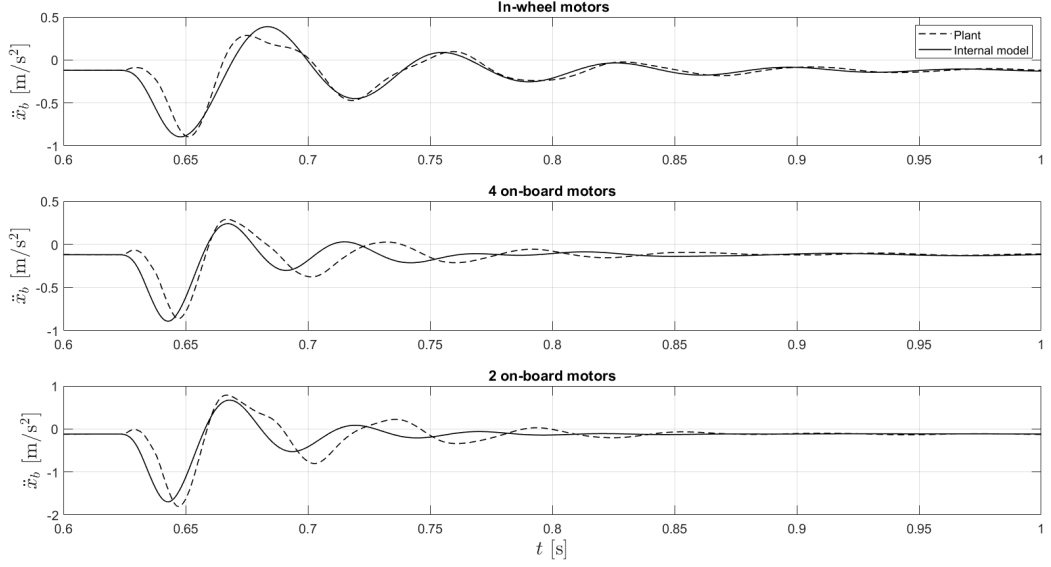


Figure 4.1: Internal models validation

It's not possible to obtain a perfect approximation for many reason, such that the approximated functions (e.g. fig. 3.14, eq. 3.9), the enveloping model that substitutes MF-Swift, etc. After the validation tests, the analysis can proceed.

4.1.2 Performance assessment

The KPIs that are usually used for this kind of applications, e.g. in [58], are the following:

- $RMS_{\ddot{x}_b}$ is the root mean squared error of the longitudinal acceleration of the vehicle respect to its steady-state reference value:

$$RMS_{\ddot{x}_b} = \sqrt{\frac{1}{T_2 - T_1} \int_{T_1}^{T_2} [\ddot{x}_b - \ddot{x}_{b,ref}]^2 dt}$$

- $VDV_{\ddot{x}_b}$ is the fourth power longitudinal acceleration vibration dose value:

$$VDV_{\ddot{x}_b} = \sqrt[4]{\int_{T_1}^{T_2} [\ddot{x}_b - \ddot{x}_{b,ref}]^4 dt}$$

- $RMS_{\ddot{\dot{x}}_b}$ is the root mean square value of the longitudinal jerk of the vehicle:

$$RMS_{\ddot{\dot{x}}_b} = \sqrt{\frac{1}{T_2 - T_1} \int_{T_1}^{T_2} \ddot{\dot{x}}_b^2 dt}$$

- $\Delta\ddot{x}_{b,max}$ is the maximum longitudinal acceleration error between the actual longitudinal acceleration and its reference value:

$$\Delta\ddot{x}_{b,max} = \max(|\ddot{x}_b - \ddot{x}_{b,ref}|)$$

4.2 Prediction horizon and preview analysis

The target of this analysis is to identify the optimal calibration of the for a localized road event, i.e., the 20 mm step. The sensitivity of the controllers is assessed by considering zero total torque demand $T_{m,req}$ and an initial longitudinal speed \dot{x}_b equal to 40 km/h. The cost function weight matrices, i.e., Q and R , introduced in eq. 1.13, have been assumed constant for the specific case of prediction horizon equal to 30 ms. The prediction horizon was already introduced in figure 1.11, while the preview (fig. 3.9, 3.13) corresponds to the amount of information that the controller receives in advance. In this application, the preview allows the controller to know the road profile with some time step ahead. The greater is the preview time, the earlier the controller will see the road profile unevenness.

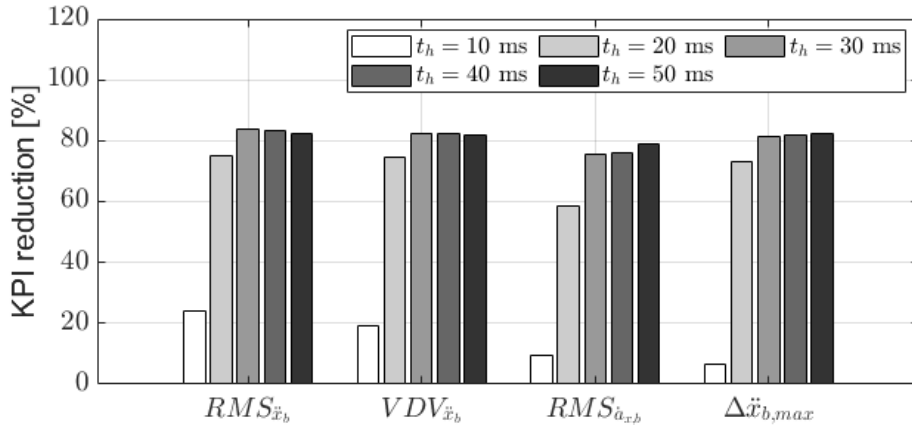


Figure 4.2: Prediction horizon KPIs : in-wheel model

Let's start with the in-wheel model. From the figure 4.2, the value on the vertical axis corresponds to the KPIs improvement that the active plant has respect the passive one, and it is expressed in percentage. It is easy to understand that a greater percentage value means that the system is better controlled. For this reason, the prediction horizons from 30 to 50, which have KPIs improvements up to 80%, are optimal.

Moreover, according to the increment of the prediction horizon, also the computation time increases, as shown in the figure 4.3.

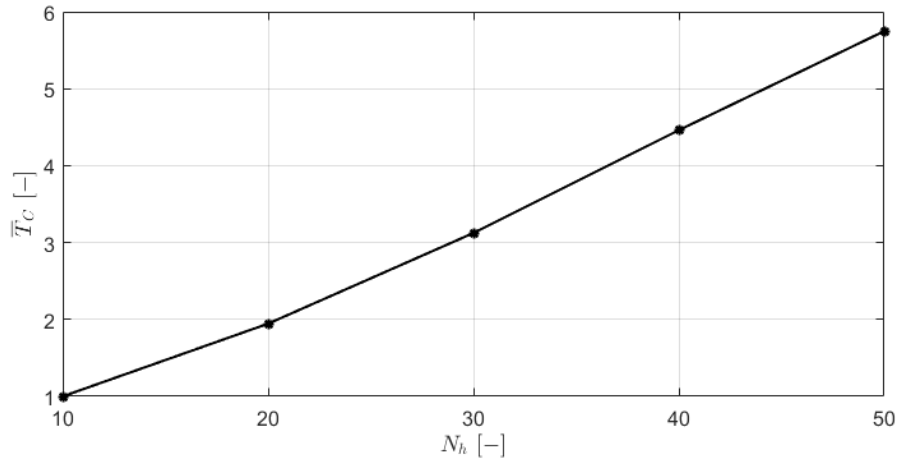


Figure 4.3: Computation time : in-wheel model

Here, the non-dimensional running times are normalized w.r.t. the case with the lowest prediction horizon. Can be notice that the computation time increases in an almost linear way. So, due to the fact that the KPIs from 30 to 50 (fig. 4.2) are almost the same, the prediction horizon N equal to 30 is chosen, in order to consider a good trade-off between accuracy and computation time. The corresponding running time is around 1.1 s. It is important to understand that the computation time cannot be too much high, because of real time implementation.

As said, the other main factor that we want to analyze is the preview.

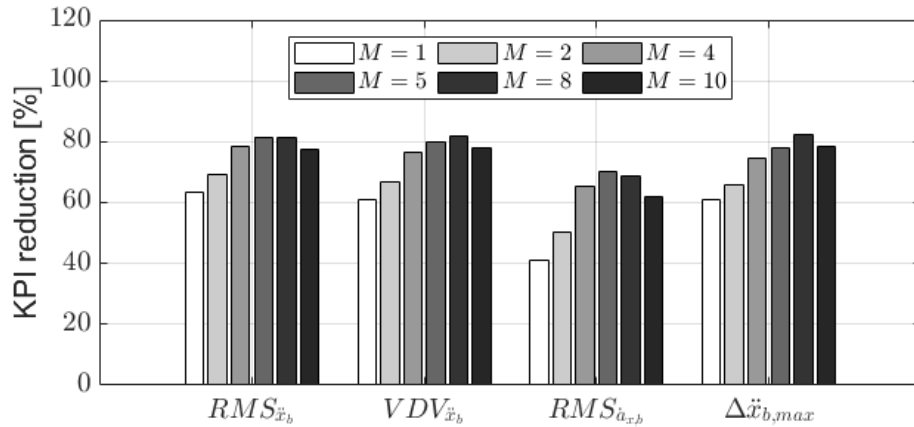


Figure 4.4: Preview KPIs : in-wheel model

In figure 4.4, the KPIs rise with a preview having up to 5/8 steps, and then they decrease. For this reason, was chosen, as the preview steps, $M = 5$. The main

factor of this decrease is the internal model that is not exactly equal to the plant model. This obviously produces an error that can be propagated, both according to the prediction horizon (fig. 4.2) and the preview steps (fig. 4.4).

All the main parameters are summarized in the following table.

| Parameter | Description | Value | Unit |
|-----------|---------------------|-------|------|
| N | Prediction horizon | 30 | [-] |
| M | Preview steps | 5 | [-] |
| T_s | Discretization time | 1 | [ms] |
| T_c | Computation time | 1.1 | [s] |

Table 4.1: NMPC parameters : in-wheel model

Let's continue to analyse the 4 on-board powertrains:

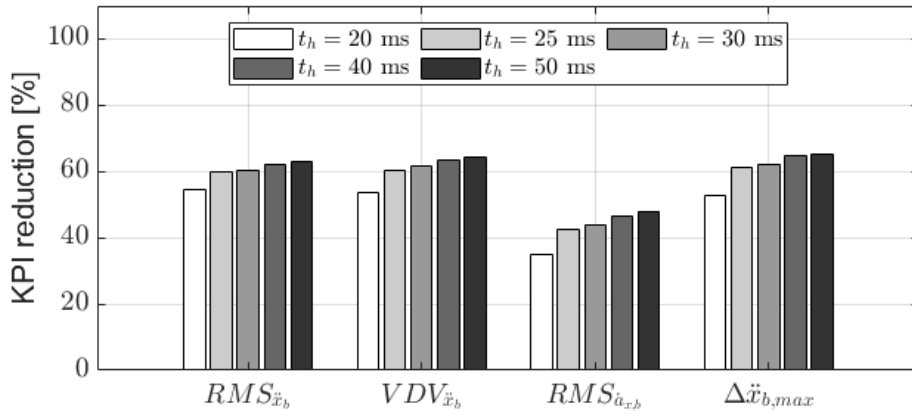


Figure 4.5: Prediction horizon KPIs : 4 on-board model

In the graph in Fig. 4.5, respect to the previous case in which after a given value of ph the KPIs decreases, here they continues to increments. But, a greater prediction horizon, leads to a greater computation time.

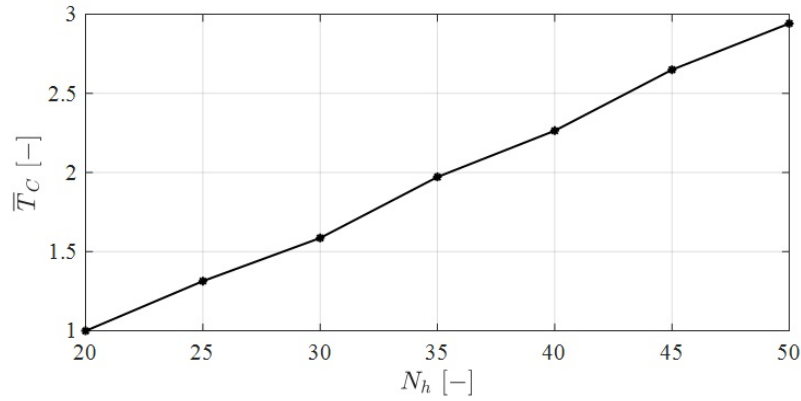


Figure 4.6: Computation time : 4 on-board model

By considering the KPIs improvement and the computation time, a prediction horizon of 30 steps, which is a good trade-off, has been chosen. Its running time is around 2.1 s. It is interesting how, due to the presence of the torsional dynamics equations in the 4 on-board motor's internal model, the computation time in fig. 4.6 is almost double than the previous one, shown in tab. 4.1.

The other main factor to check is the preview, that is shown in the figure 4.7. The gap between the first column, which corresponds to 5 steps, and the second one, which corresponds to 10, is very big. However, by considering the best option for each KPI, the optimal amount of preview steps is 25.

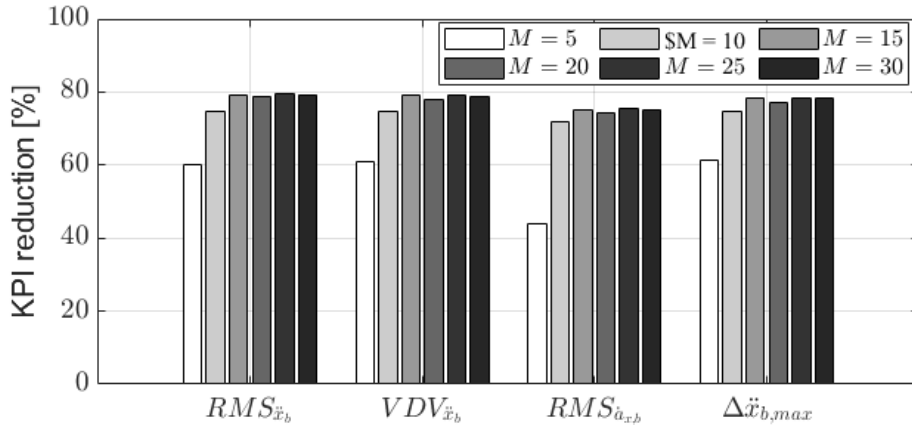


Figure 4.7: Preview KPIs : 4 on-board model

As in the previous case, the main parameters are summarized in the following table.

| Parameter | Description | Value | Unit |
|-----------|---------------------|-------|------|
| N | Prediction horizon | 30 | [-] |
| M | Preview steps | 25 | [-] |
| T_s | Discretization time | 1 | [ms] |
| T_c | Computation time | 2.1 | [s] |

Table 4.2: NMPC parameters : 4 on-board model

In the end, the last model to analyse is the vehicle model with 2 on-board motors and open differential.

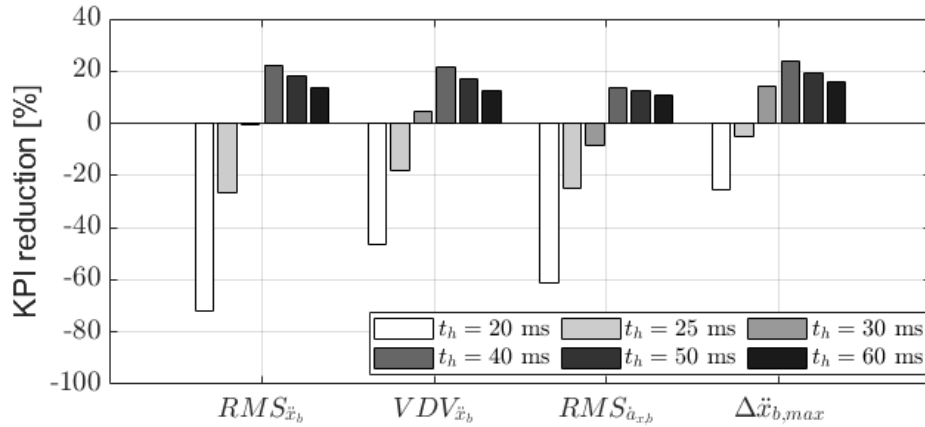


Figure 4.8: Prediction horizon KPIs : 2 on-board model

It is noticeable that the KPIs percentages are worst respect to the previous model and after a prediction of 40 ms, they decrease. The reason for a loss of performance at high prediction horizon can be identified in a non-optimal weight scheduling, which is kept constant for different prediction horizon length, and an increasing of the cumulative error caused by the mismatch between real plant and prediction model [65] [66]. It is easy to understand that the optimal prediction horizon is 40.

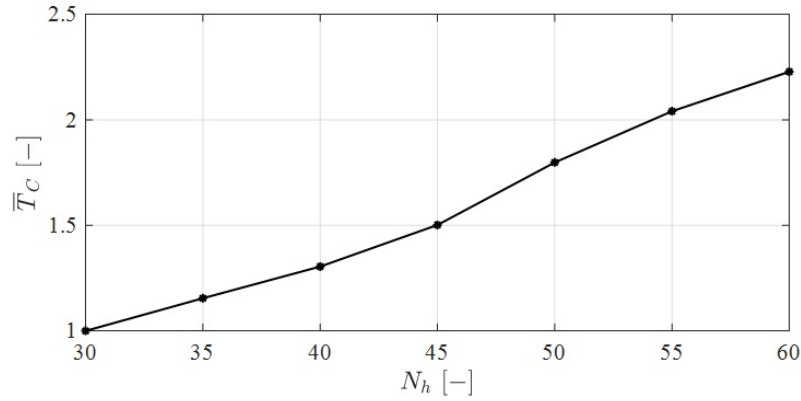


Figure 4.9: Computation time : 2 on-board model

Due to the presence of the open differential equations, the formulation of the NMPC is much more complex and so the running time is much greater than in the previous cases (tab. 4.1, 4.2). In detail, the computation time is 8.8 s, that is approximately 4 times greater than the previous case (tab. 4.2) and 8 times greater than the first case (tab. 4.1).

The last part of this analysis consists in determining the optimal preview steps.

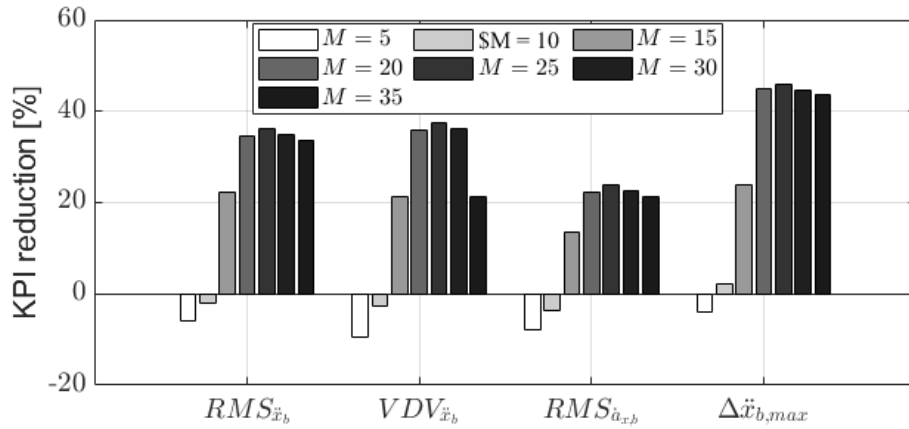


Figure 4.10: Preview KPIs : 2 on-board model

In case of a few preview steps, when the NMPC receives the road profile information, it has not enough time to provide a corrected motor torque $T_{m,cor}$ such that the oscillations of acceleration can be compensated. So, the optimal amount of preview steps is 25.

The main NPMPC parameters are summarized in the following table.

| Parameter | Description | Value | Unit |
|-----------|---------------------|-------|------|
| N | Prediction horizon | 40 | [-] |
| M | Preview steps | 25 | [-] |
| T_s | Discretization time | 1 | [ms] |
| T_c | Computation time | 8.8 | [s] |

Table 4.3: NMPC parameters : 2 on-board model

4.3 Controller evaluation on step

This analysis aims to explore the potential performance of the pre-emptive NMPC when its calibrations is optimized for a localized road event as the 20 mm step. The test is carried out by considering zero total torque demand and an initial longitudinal speed \dot{x}_b equal to 40 km/h.

The plant models are represented in case of passive plant (non-controlled), active plant without preview ($M = 0$), indicated as NMPC^(w/o prev), and active plant with preview, specified as NMPC^(prev). Fig. 4.11 shows the road distance profiles of the main variables for the three different powertrain architectures. Moreover, the plots refer to individual front and rear corners; given the symmetry of the selected road profile, the results are identical on the left and right vehicle sides. The longitudinal acceleration \ddot{x}_b is shown in the first row. The second row shows the front and rear motor torques $T_{m,F}$ and $T_{m,R}$ while the third row shows the motor torques at the wheels for the in-wheel case T_w and at the half shafts T_{hs} for the on-board cases.

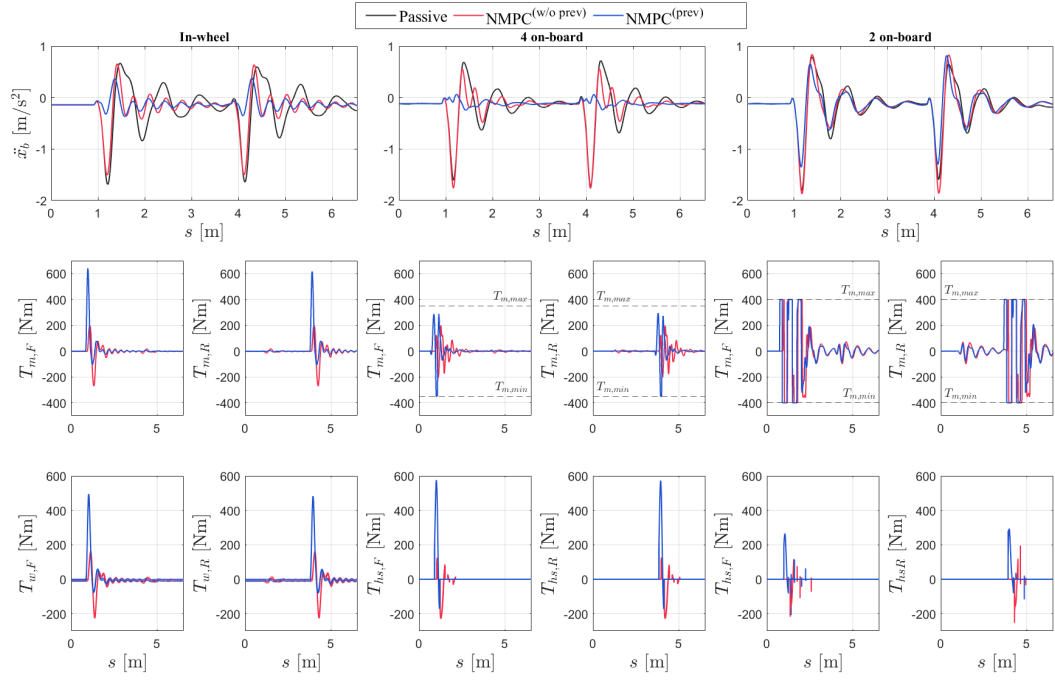


Figure 4.11: Comparison : step 2 cm

The road preview has a significant effect for localized event, e.g., step or speed bump, as it allows to significantly reduce the first peak by requesting a motor torque in advance. This results clearly show as the control algorithm can effectively work both for the in-wheel powertrain but also for the on-board cases by including the torsional dynamics, the electric motor dynamics and the equivalent backlash in the internal model formulations. The NMPC^(prev) bring a generalized improvement in terms of longitudinal acceleration, reducing the related indicators KPIs of > 85% for the 4 on-board model, 80% for the in-wheel model and 30% for the 2 on-board model.

On the other hand, the configuration without preview only bring a minor response improvement after the step for the in-wheel. In the on-board cases, the controller is partially or not capable to attenuate the longitudinal acceleration oscillations due to the delay in the response caused by the torsional and electric motor dynamics and the equivalent backlash of the transmission.

In contrast to the 4 on-board models, the performance of 2 on-board motors model are worse. This is caused by many factors such as bigger motor time constant and inertia moment, asymmetry between left and right side, bigger backlash etc.

4.4 Controller evaluation on road with irregularities

While the previous analysis is focused on analysing the NMPCs' robustness for the step profile, this section shows how performing the controllers are for an uneven road profile. Therefore, in order to better adapt each controller with the new road scenario, these analyses were done by changing the calibration of the weights Q and R , used for the step profile (fig. 4.11), and some tire structure parameters in the prediction model, $k_{r,f}$, $c_{r,f}$, $k_{t,f}$ and $c_{t,f}$ 3.1, to achieve a better compatibility between the NMPC prediction model and the MF Swift tire model.

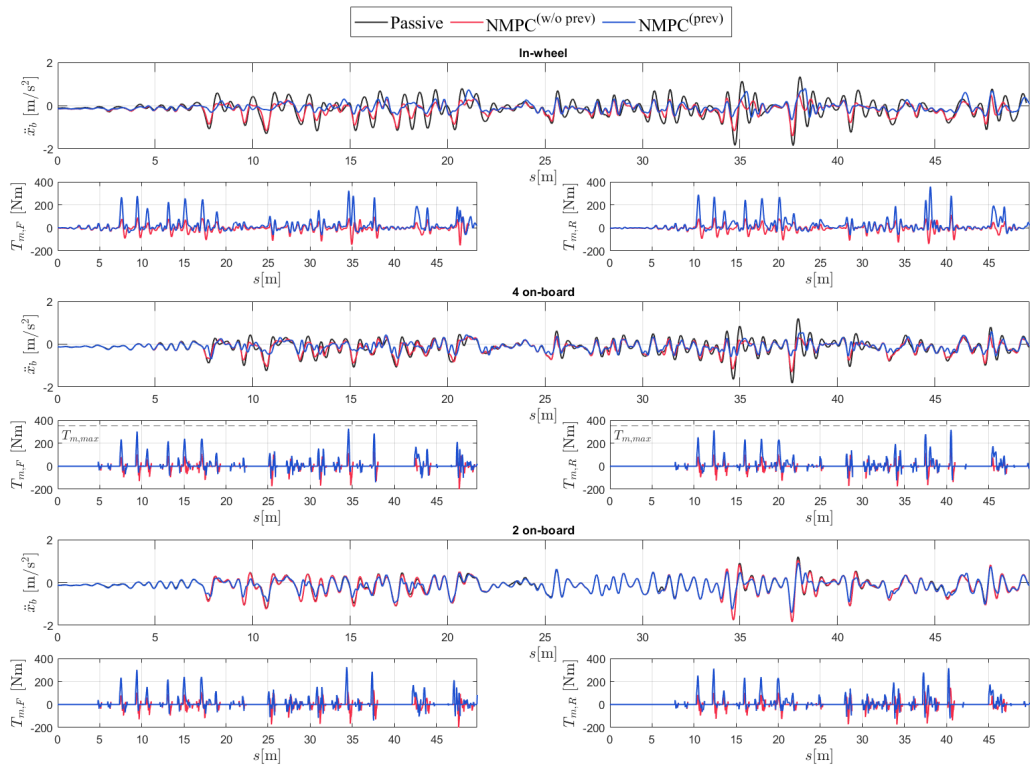


Figure 4.12: Comparison : uneven road profile

Fig. 4.12 shows the controllers performance comparison on a section of uneven road profiles, in conditions of zero motor torque demand, with initial speed of 40 km/h. The figures include the passive configuration, $NMPC^{(w/o\ prev)}$ and the $NMPC^{(prev)}$ for all three models.

On one hand, for the in-wheel and 4 on-board models, it can be noticed a large improvement, mainly due to the preview. This benefit can be easily seen at the acceleration peaks, e.g. immediately before and after 15 m. However, the case

without preview still provides some improvements, which can be easily noticed, for example, from 20 to 25 m. In case of 4 on-board motors, compared to the step profile 4.11, the NMPC's performance get worse. On the other hand, the 2 on-board model is not significantly controlled by the NMPC, both with and without preview. This trend is similar to the one for the step profile, shown in fig. 4.11. However, thanks to the preview, a marginal improvement w.r.t. the passive vehicle is provided.

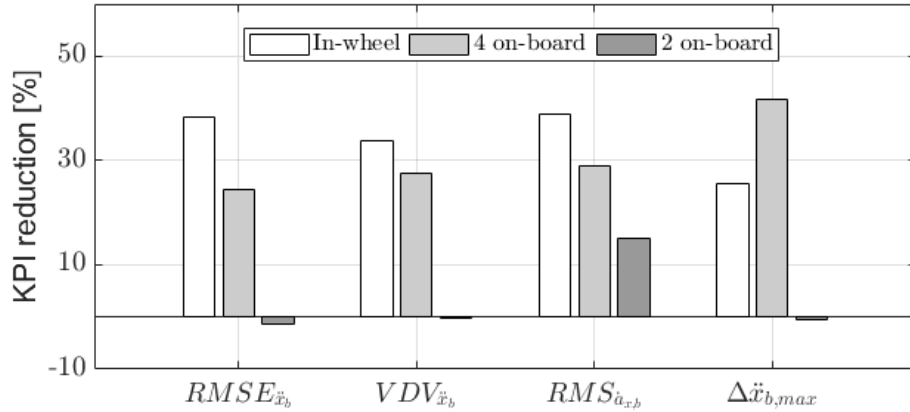


Figure 4.13: Comparison : road without preview

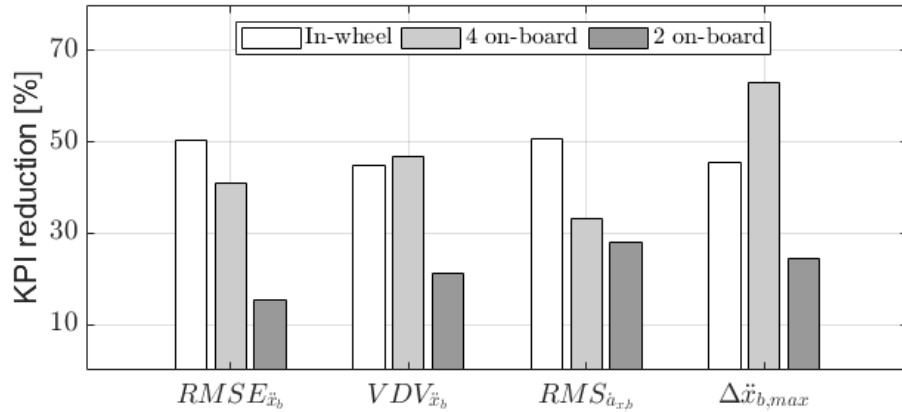


Figure 4.14: Comparison : road with preview

Fig 4.13 shows the KPI percentage reduction of the $NMPC^{(w/o\ prev)}$ w.r.t. the passive configuration for all models, while the 4.14 shows the KPI reduction caused by $NMPC^{(prev)}$, also in this case w.r.t. the passive.

4.5 Asymmetric road profile

The goal of this analysis is to test the robustness of on-board configurations on an asymmetric road scenario in which the right corner of the vehicle reaches the step for first, meanwhile, the left side reaches it only after 0.25 m or 0.5 m, depending on the selected scenario. Moreover, in this scenario, the calibration weights changes with respect to previous case, because both configurations' change; indeed, for the 4 on-board powertrains the time constant remain the same, but changes the equivalent inertia and the backlash, set as for the 2 on-board configurations. In the latter one, changes the time constant from 25 ms to 5 ms. These changes are necessary to have roughly similar performance for the symmetric case, and to understand how the two models perform on an asymmetric scenario.

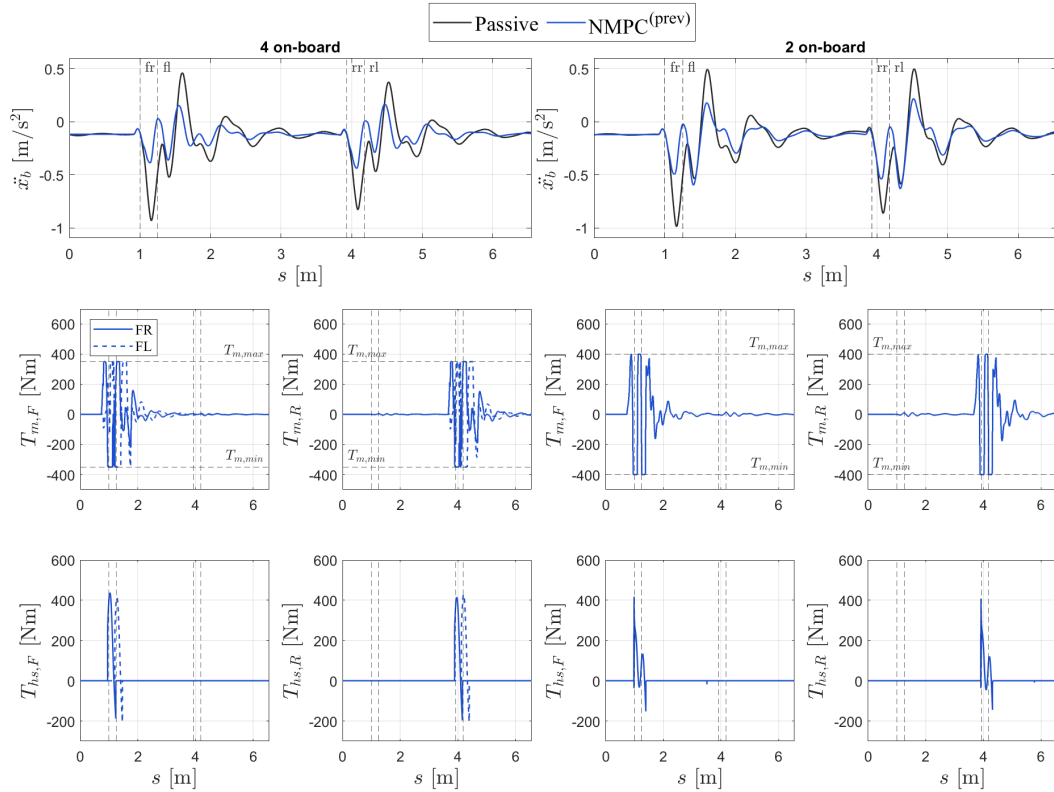


Figure 4.15: Comparison : 2 cm step with asymmetry of 0.25 m

Fig. 4.15 shows the 4 and 2 on-board powertrains, respectively on the left and right part. Because of the presence of the open differential, the requested torque is unique for axle, and the torque at the half shaft are equivalent for the right and left corner. On the other hand, the 4 on board powertrains can manage better

the asymmetrical road thanks to four different torques at half shafts, one each for corners, that can reduce the longitudinal oscillation, independently. Tables 4.5 and 4.4 shows the KPIs in three different road scenarios for both configurations, symmetric road, road with step asymmetry of 0.5 m and road with step asymmetry of 0.25 m.

| Road profile | Configuration | $RMSE_{\ddot{x}_b}$ [m/s ²] | $VDV_{\dot{x}_b}$ [m/s ^{1.75}] | $RMS_{\ddot{x}_b}$ [m/s ³] | $\Delta\ddot{x}_b$ [m/s ²] |
|---------------------------|---------------|--|---|---|---|
| Symmetric road | Passive | 0.408 | 0.558 | 52.0 | 1.645 |
| | NMPC(w prev) | 0.151 | 0.207 | 26.1 | 0.573 |
| Asymmetric road of 0.5 m | Passive | 0.282 | 0.344 | 36.6 | 0.878 |
| | NMPC(w prev) | 0.118 | 0.147 | 18.4 | 0.434 |
| Asymmetric road of 0.25 m | Passive | 0.210 | 0.282 | 28.4 | 0.813 |
| | NMPC(w prev) | 0.091 | 0.119 | 18.6 | 0.321 |

Table 4.4: Asymmetry analysis KPIs : 4 on-board model

| Road profile | Configuration | $RMSE_{\ddot{x}_b}$ [m/s ²] | $VDV_{\dot{x}_b}$ [m/s ^{1.75}] | $RMS_{\ddot{x}_b}$ [m/s ³] | $\Delta\ddot{x}_b$ [m/s ²] |
|---------------------------|---------------|--|---|---|---|
| Symmetric road | Passive | 0.419 | 0.574 | 53.4 | 1.687 |
| | NMPC(w prev) | 0.162 | 0.223 | 27.9 | 0.639 |
| Asymmetric road of 0.5 m | Passive | 0.303 | 0.372 | 39.7 | 0.940 |
| | NMPC(w prev) | 0.145 | 0.193 | 23.5 | 0.565 |
| Asymmetric road of 0.25 m | Passive | 0.234 | 0.306 | 31.4 | 0.898 |
| | NMPC(w prev) | 0.141 | 0.187 | 23.6 | 0.513 |

Table 4.5: Asymmetry analysis KPIs : 2 on-board model

Is important to highlight that also the passive KPIs changes from 2 on-board and 4 on-board, despite τ, K_s, J_{eq} and α are the same. Indeed, these KPI changes are due to different motor masses, and different shaft sprung and damper constant between left and right side, in case of the 2 on-board powertrains with open differential. To better understand the behaviour of both controller KPIs % w.r.t the passive configuration are computed

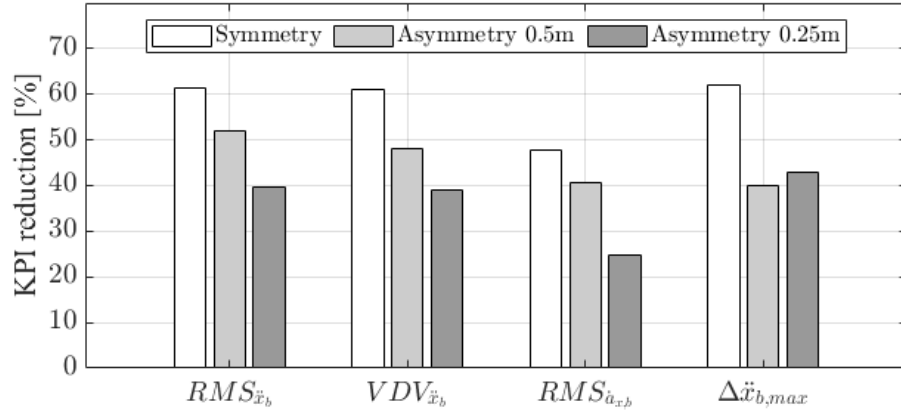


Figure 4.16: Step asymmetries : 2 on-board motors' model KPI reductions

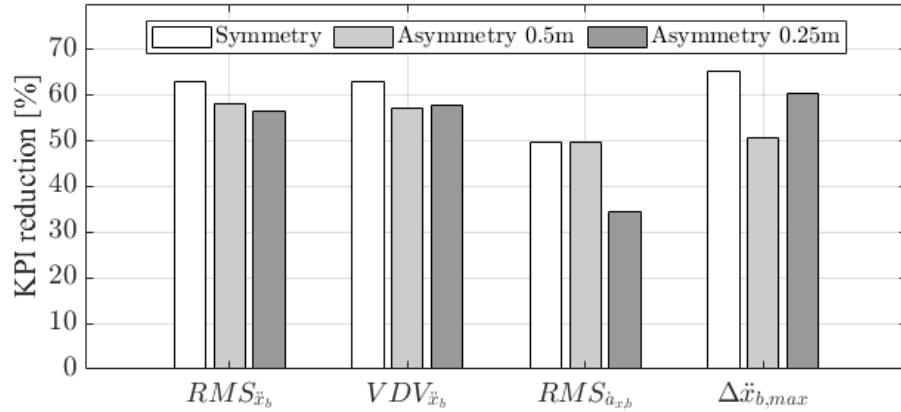


Figure 4.17: Step asymmetries : 4 on-board motors' model KPI reductions

By comparing fig. 4.16 and 4.17, it is interesting to notice that on the 2 onboard configuration, by decreasing the step asymmetry from 0.5 to 0.25 m, the controlled system succeeds less on managing the longitudinal acceleration. Indeed, the KPIs reductions decrease (e.g. in case of $RMS_{\ddot{x}_b}$, the improvement changes from more than 50% to around 40%). Instead, the KPIs improvements for the 4 on-board configuration are approximately constant at 60%.

4.6 Robustness analysis

Once developed the NMPCs, the first interesting sensitivity analysis is about the robustness. The target of this analysis is to verify the robustness of the controller

w.r.t. different initial speeds \dot{x}_b and required motor torques $T_{m,req}$ in the 20 mm step scenario. The weight matrices have been optimized for the NMPC^(prev) case in the different sub-cases. So, the weights are considered optimal for the first case, but not for the second one.

4.6.1 Speed analysis

The first robustness analysis, whose data are collected in tab. 4.6, 4.7, and 4.8, have been obtained through simulations whose required motor torque $T_{m,req}$ is null.

Regarding the case of NMPC^(prev), the KPIs show an improvement compared to the passive case, especially in the 4 motors models (tab. 4.6, 4.7). As the speed increases, the KPIs of the in-wheel model (tab. 4.6) and 4 on-board model (tab. 4.7) still have good results, having a rate of improvement of approximately 75% w.r.t. the passive case. On the other hand, the 2 on-board model presents a loss of efficiency at high speeds, but still guarantees a good improvement w.r.t. the passive case. In fact, the rate of improvement is around 30% at 20 km/h, 20% at 40 km/h, and 10% at 80 km/h.

Moreover, it can be noticed that, without the information given in advanced by the preview, no significant improvements occur, with the exception of the 4 in-wheel model (tab. 4.6), which shows a rate of improvement of almost 40%. This behaviour is caused by the dynamic response of the powertrains; indeed, the torsional stiffness of the half-shaft, the mass moments of inertia of the powertrains components, ecc, are responsible for a significant deterioration in the system response in terms of the wheel torque. This analysis demonstrates that the NMPCs for the 4 motors' models (tab. 4.6, 4.7) are robust in a range of speeds, at least from 20 to 80 km/h. This may be due to the different motor time constant between the 4 motors and 2 motors' models (2.4), that if it is enough small it can guarantee a good control technique also at high speeds. Moreover, it proves the need to implement the preview in the control method.

| $\dot{x}_{b,ini}$ [km/h] | Configuration | $RMSE_{\ddot{x}_b}$ [m/s ²] | $VDV_{\ddot{x}_b}$ [m/s ^{1.75}] | $RMS_{\ddot{\dot{x}}_b}$ [m/s ³] | $\Delta\ddot{x}_b$ [m/s ²] |
|-----------------------------|----------------------------|--|--|---|---|
| 20 | Passive | 0.373 | 0.702 | 31.3 | 1.662 |
| | NMPC ^(w/o prev) | 0.217 | 0.514 | 19.9 | 1.310 |
| | NMPC ^(w prev) | 0.059 | 0.101 | 9.5 | 0.241 |
| 40 | Passive | 0.419 | 0.581 | 44.6 | 1.547 |
| | NMPC ^(w/o prev) | 0.316 | 0.504 | 44.6 | 1.375 |
| | NMPC ^(w prev) | 0.099 | 0.135 | 16.4 | 0.345 |
| 80 | Passive | 0.387 | 0.436 | 42.1 | 1.249 |
| | NMPC ^(w/o prev) | 0.262 | 0.346 | 40.1 | 0.965 |
| | NMPC ^(w prev) | 0.081 | 0.099 | 13.6 | 0.278 |

Table 4.6: Speed analysis KPIs : in-wheel model

| $\dot{x}_{b,ini}$ [km/h] | Configuration | $RMSE_{\ddot{x}_b}$ [m/s ²] | $VDV_{\ddot{x}_b}$ [m/s ^{1.75}] | $RMS_{\ddot{\dot{x}}_b}$ [m/s ³] | $\Delta\ddot{x}_b$ [m/s ²] |
|-----------------------------|----------------------------|--|--|---|---|
| 20 | Passive | 0.327 | 0.595 | 32.0 | 1.488 |
| | NMPC ^(w/o prev) | 0.238 | 0.592 | 26.6 | 1.492 |
| | NMPC ^(w prev) | 0.084 | 0.160 | 8.7 | 0.442 |
| 40 | Passive | 0.370 | 0.561 | 47.0 | 1.612 |
| | NMPC ^(w/o prev) | 0.331 | 0.574 | 49.1 | 1.650 |
| | NMPC ^(w prev) | 0.045 | 0.063 | 8.1 | 0.178 |
| 80 | Passive | 0.385 | 0.398 | 55.1 | 1.058 |
| | NMPC ^(w/o prev) | 0.366 | 0.424 | 57.4 | 1.177 |
| | NMPC ^(w prev) | 0.105 | 0.097 | 21.9 | 0.265 |

Table 4.7: Speed analysis KPIs : 4 on-board model

| $\dot{x}_{b,ini}$ [km/h] | Configuration | $RMSE_{\ddot{x}_b}$ [m/s ²] | $VDV_{\ddot{x}_b}$ [m/s ^{1.75}] | $RMS_{\ddot{\dot{x}}_b}$ [m/s ³] | $\Delta\ddot{x}_b$ [m/s ²] |
|-----------------------------|----------------------------|--|--|---|---|
| 20 | Passive | 0.324 | 0.562 | 31.4 | 1.377 |
| | NMPC ^(w/o prev) | 0.316 | 0.634 | 32.1 | 1.599 |
| | NMPC ^(w prev) | 0.228 | 0.403 | 22.6 | 0.967 |
| 40 | Passive | 0.382 | 0.574 | 48.8 | 1.684 |
| | NMPC ^(w/o prev) | 0.399 | 0.627 | 52.6 | 1.751 |
| | NMPC ^(w prev) | 0.293 | 0.440 | 42.6 | 1.231 |
| 80 | Passive | 0.351 | 0.428 | 49.7 | 1.144 |
| | NMPC ^(w/o prev) | 0.365 | 0.446 | 51.3 | 1.202 |
| | NMPC ^(w prev) | 0.326 | 0.398 | 47.8 | 1.043 |

Table 4.8: Speed analysis KPIs : 2 on-board model

4.6.2 Torque analysis

The second robustness analysis, whose data are collected in tab. 4.9, 4.10, and 4.11, is referred to different requested motor torque and have been obtained through simulations with an initial speed \dot{x}_b equal to 40 km/h. Regarding the case of NMPC^(prev), the KPIs improvement of the in-wheel model with respect to the passive case (tab. 4.9) are good at each required motor torque. Indeed, the rate of improvement only goes from around 80% to 70%. Instead, the performance of the NMPC^(prev), for the 4 on-board model (tab. 4.10), decreases more: the rate of improvement decreases from almost 85% at $T_{m,req} = 0$ Nm, to approximately 60% at $T_{m,req} = 1200$ Nm, to almost 40% at $T_{m,req} = 2400$ Nm. However, the improvements are still good at each required motor torque. In the end, the rate improvement of the 2 on board model for each required motor torque is kept approximately constant at around 30%.

Compared to the speed analysis (tab. 4.6, 4.7, 4.8), without the use of the preview, small improvements occur for each model at almost all the required motor torque, but not significantly as in the previous analysis.

This analysis demonstrates that only the performance of the 4 on-board motors' model depends on the required motor torque. Indeed, in the step simulation (fig. 4.11), the corrected motor torque was not even close to its limits in the in-wheel model, while in the 4 on-board case it was really close to its saturation level and in the 2 on-board model, it was fully saturated. By increasing the required motor torque, the corrected motor torque tends to reaches first its saturation limits. Moreover, this analysis, as the previous one, proves the need to implement the preview in the control method.

| $T_{m,req}$ [Nm] | Configuration | $RMSE_{\ddot{x}_b}$ [m/s ²] | $VDV_{\ddot{x}_b}$ [m/s ^{1.75}] | $RMS_{\ddot{\ddot{x}}_b}$ [m/s ³] | $\Delta\ddot{x}_b$ [m/s ²] |
|---------------------|----------------------------|--|--|--|---|
| 0 | Passive | 0.419 | 0.581 | 44.6 | 1.547 |
| | NMPC ^(w/o prev) | 0.316 | 0.504 | 44.6 | 1.375 |
| | NMPC ^(w prev) | 0.099 | 0.135 | 16.4 | 0.345 |
| 1200 | Passive | 0.385 | 0.544 | 42.0 | 1.467 |
| | NMPC ^(w/o prev) | 0.343 | 0.535 | 40.5 | 1.486 |
| | NMPC ^(w prev) | 0.103 | 0.147 | 18.1 | 0.448 |
| 2400 | Passive | 0.335 | 0.536 | 37.1 | 1.545 |
| | NMPC ^(w/o prev) | 0.295 | 0.513 | 35.6 | 1.488 |
| | NMPC ^(w prev) | 0.116 | 0.161 | 17.5 | 0.451 |

Table 4.9: Torque analysis KPIs : in-wheel model

| $T_{m,req}$ [Nm] | Configuration | $RMSE_{\ddot{x}_b}$ [m/s ²] | $VDV_{\ddot{x}_b}$ [m/s ^{1.75}] | $RMS_{\ddot{\ddot{x}}_b}$ [m/s ³] | $\Delta\ddot{x}_b$ [m/s ²] |
|---------------------|----------------------------|--|--|--|---|
| 0 | Passive | 0.370 | 0.561 | 47.0 | 1.612 |
| | NMPC ^(w/o prev) | 0.331 | 0.574 | 49.1 | 1.650 |
| | NMPC ^(w prev) | 0.045 | 0.063 | 8.1 | 0.178 |
| 1200 | Passive | 0.318 | 0.502 | 41.9 | 1.475 |
| | NMPC ^(w/o prev) | 0.297 | 0.476 | 46.4 | 1.420 |
| | NMPC ^(w prev) | 0.131 | 0.173 | 19.0 | 0.507 |
| 2400 | Passive | 0.299 | 0.479 | 40.1 | 1.465 |
| | NMPC ^(w/o prev) | 0.273 | 0.444 | 43.2 | 1.376 |
| | NMPC ^(w prev) | 0.173 | 0.225 | 25.6 | 0.709 |

Table 4.10: Torque analysis KPIs : 4 on-board model

| $T_{m,req}$ [Nm] | Configuration | $RMSE_{\ddot{x}_b}$ [m/s ²] | $VDV_{\ddot{x}_b}$ [m/s ^{1.75}] | $RMS_{\ddot{\ddot{x}}_b}$ [m/s ³] | $\Delta\ddot{x}_b$ [m/s ²] |
|---------------------|----------------------------|--|--|--|---|
| 0 | Passive | 0.382 | 0.574 | 48.8 | 1.684 |
| | NMPC ^(w/o prev) | 0.399 | 0.627 | 52.6 | 1.751 |
| | NMPC ^(w prev) | 0.293 | 0.440 | 42.6 | 1.231 |
| 1200 | Passive | 0.305 | 0.495 | 41.6 | 1.480 |
| | NMPC ^(w/o prev) | 0.274 | 0.482 | 39.6 | 1.435 |
| | NMPC ^(w prev) | 0.204 | 0.330 | 33.5 | 0.989 |
| 2400 | Passive | 0.312 | 0.469 | 43.9 | 1.465 |
| | NMPC ^(w/o prev) | 0.301 | 0.478 | 42.9 | 1.463 |
| | NMPC ^(w prev) | 0.230 | 0.326 | 37.4 | 0.954 |

Table 4.11: Torque analysis KPIs : 2 on-board model

4.7 Powertrains parameters' sensitivity analysis

To understand which parameters can affect more the NMPC's performance, simulation based sensitivity analyses have been carried out. All simulations' data have been taken by considering only one model, the one with 4 on-board motors, in a localized road event (2 cm step) and constant weights equal to the optimal values for $T_{m,req} = 0$ Nm and $v = 40$ km/h. This approach is relevant, since, depending on the result, it will show how the controller's efficiency to reduce the longitudinal oscillations will be affected by changing different parameters. Fig 4.18, 4.19 and 4.20, show the behaviour of the vehicle as function of the time constant, the equivalent inertia moment, and the shaft stiffness.

The first sensitivity analysis has been done by changing the time constant of the motor. The effect of increasing τ on the performance of the controller is reported in the figure below.

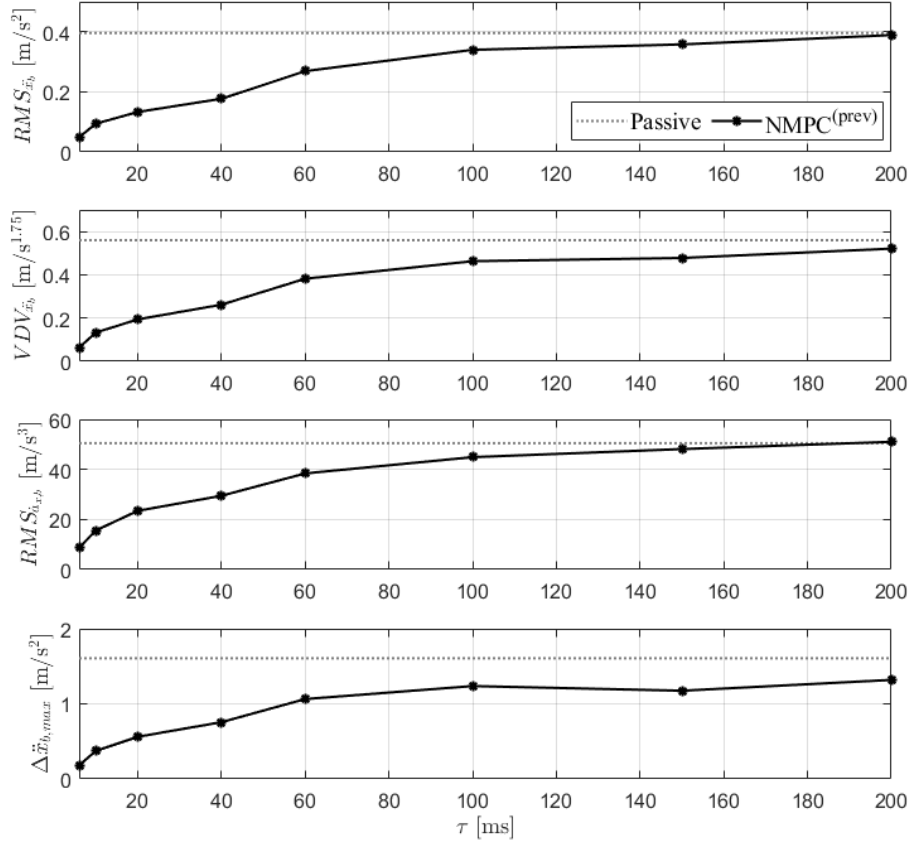


Figure 4.18: Motor time constant sensitivity

The KPIs of the passive system are constant along the horizontal axis, since τ affects only the controller's performance and not the vehicle's structure. A progressive worsening of all indicators is observed as function of τ , highlighted by a logarithmic shape of the curve. By getting into detail, the performance of the passive system is reached by increasing the time constant from 6 to 200 ms.

The second analysis refers to the equivalent inertia moment.

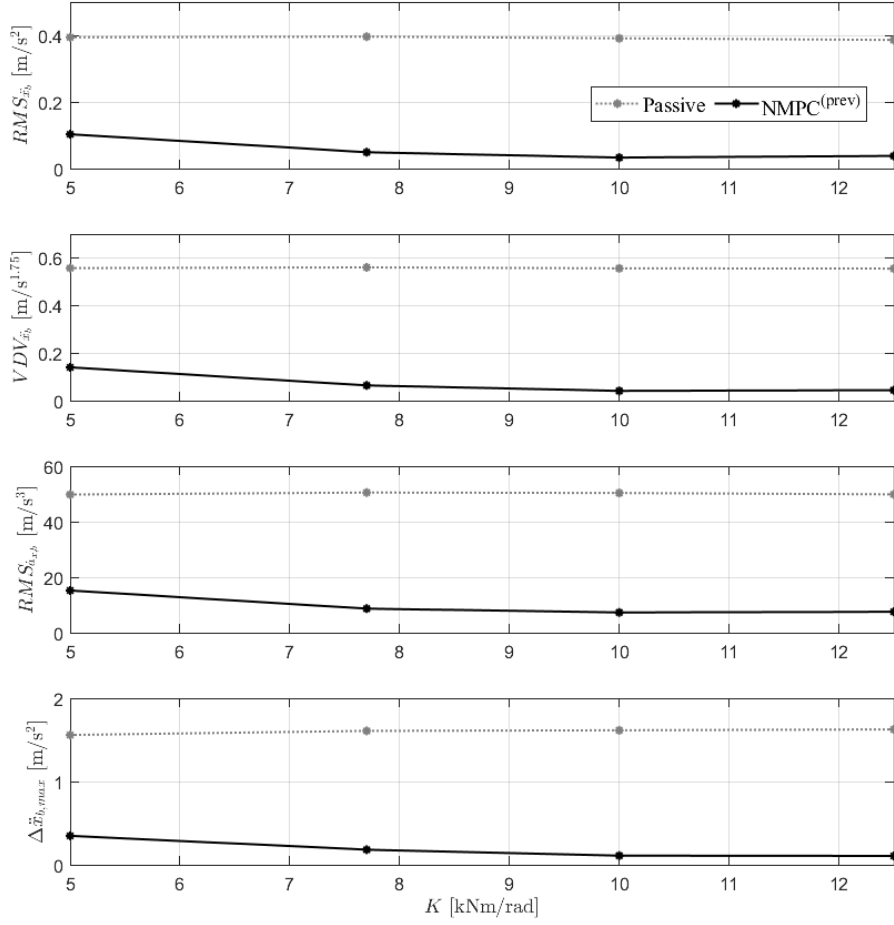


Figure 4.19: Equivalent inertia moment sensitivity

In this case, the passive configuration changes by changing J , unlike the previous case, since also the vehicle structure's characteristics change. By doubling the inertia, also the KPIs double. For example, the RMS value of \ddot{x}_b for NMPC^(w/o prev) increases from 0.05 to 0.103. Moreover, the jerk reduction is more evident for NMPC^(prev), with its RMS value that changes from 8.86 to 19.68. This happens because, by increasing J_{eq} , the angular acceleration of half shaft $\ddot{\theta}_s$ decreases, improving the performance.

The third sensitivity analysis is referred to the shaft stiffness.

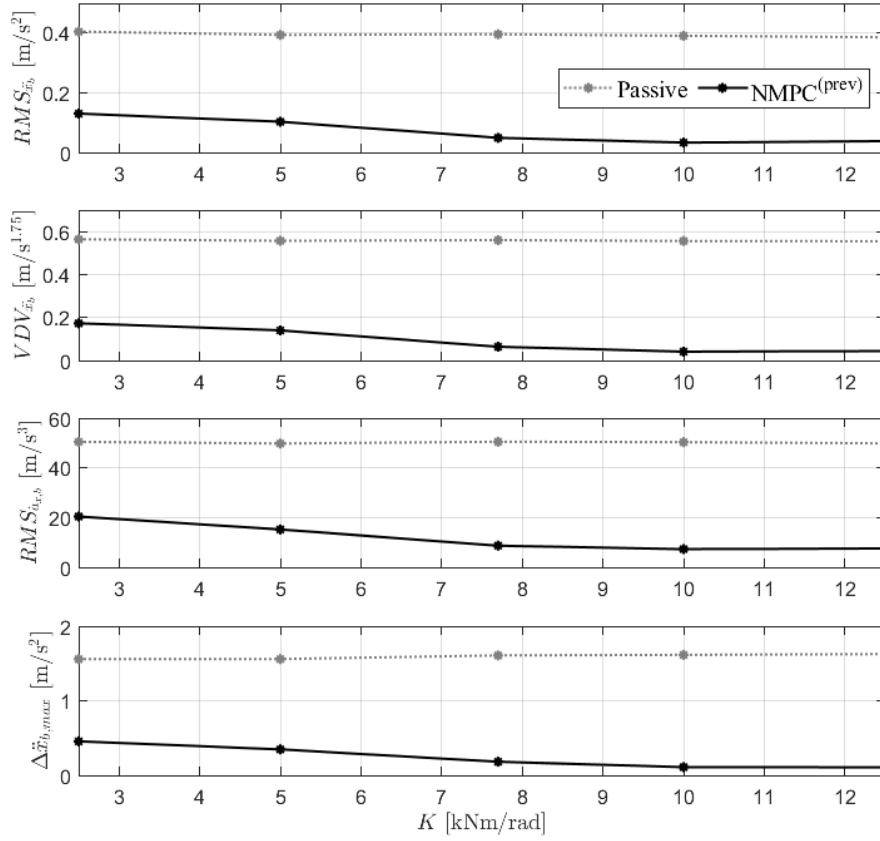


Figure 4.20: Half shaft stiffness sensitivity

As in the previous case, the passive configuration changes. It can be concluded that the NMPC^(prev) performs better with a higher value of half shaft stiffness, since, by increasing K , the KPIs improve.

4.7.1 Backlash sensitivity analysis of different models

The target of this analysis is to verify, through simulations, how the performance of the controller changes by considering not only a variation of the equivalent backlash, but also by progressively and simultaneously changing the following parameters: motor time constant τ from 6 to 25 ms, half shaft stiffness K from 7700 to 6500 Nm/rad, and equivalent inertia moment J_{eq} from 1.4 to 2.8 kgm². For this analysis, the optimal weights have been obtained for each model, at backlash equal to 1.2°. This sensitivity analysis is shown in a different way w.r.t. the previous ones; in fact, the percentage reductions of the selected KPIs, w.r.t. their values for the passive EV, are shown. The figure 4.21 shows four different configurations. Each one of them differs from the previous one, on just one modified parameter: NMPC

is characterized by $\tau = 6$ ms, NMPC^τ by $\tau = 25$ ms, $\text{NMPC}^{\tau,K}$ by $K = 6500$ Km/rad, and $\text{NMPC}^{\tau,K,J}$ by $J = 2.8$ kgm².

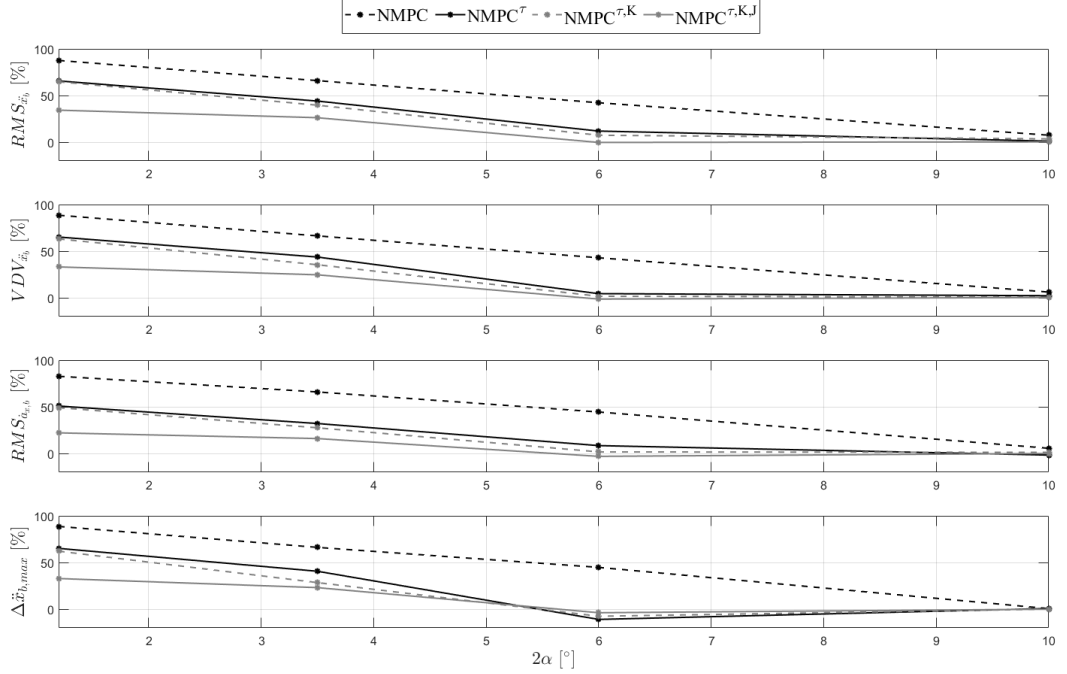


Figure 4.21: Sensitivity analysis of different models w.r.t. the backlash

The results highlight that, by considering a model with more changed variables, the KPIs get worse. It can be noticed that the RMS values of \ddot{x}_b in $\text{NMPC}^{\tau,K,J}$ is worse than the passive system also with 2α equal to 6° , compared to the other models where the backlash must increase up to 10° .

Considering a small backlash of 1.2° , the KPIs improvements are halved with a motor time constant of 25 ms. Moreover, with the addition of a double equivalent inertia moment, the improvements get further reduced by half. Instead, increasing the backlash up to 6° , the greatest gap is due to the motor time constant. In the end, at 10° , each configuration reaches approximately the same KPIs, with a null improvement w.r.t. the passive configuration.

In conclusion, with a small backlash, both the motor time constant and equivalent inertia are the main parameters that affect the performance, while at higher backlash, only the motor time constant affects the system.

4.8 dSPACE

The controllers have been designed in order to provide computational efficiency that facilitates the implicit real-time implementation of the controller; indeed, by considering only one corner of the vehicle, for the 4 on-board powertrains, or only one axle, for the 2 on-board powertrains, instead of the full vehicle, a reduced number of states, control inputs and parameters have been considered. The real-time tests have been run on a dSPACE MicroAutoBox III system

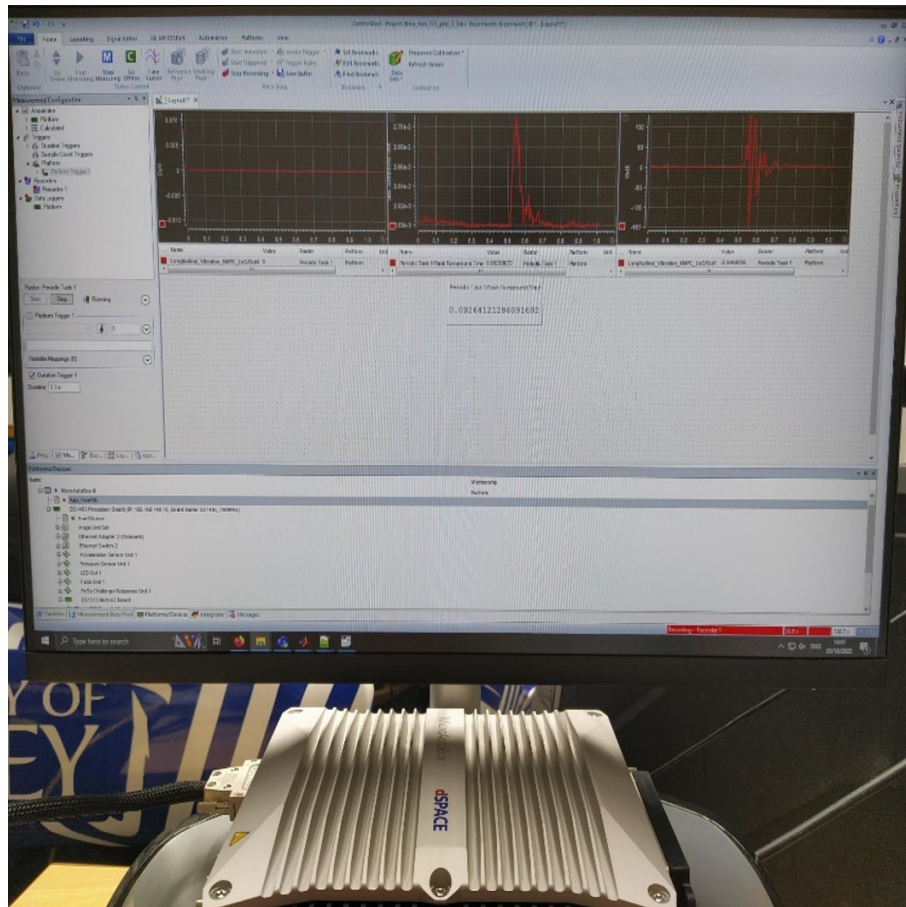


Figure 4.22: dSPACE

Different configurations were tested, by starting with small prediction horizon and high sampling time with respect the simulation on Simulink, until reaching the following set of values:

- For the in-wheel powertrains, with a sampling time T_s of 3 ms, a prediction horizon steps N of 9 and 2 controller's iterations N_{iter} , the turnaround time

TAT is equal to 2.5 ms,

- For the 4 on-board powertrains, with a sampling time T_s of 4 ms, a prediction horizon steps N of 7 and 2 controller's iterations N_{iter} , the turnaround time **TAT** is equal to 3.25 ms.
- For the 2 on-board powertrains, with a sampling time T_s of 6 ms, a prediction horizon steps N of 7 and 1 controller's iterations N_{iter} , the turnaround time **TAT** is equal to 5.5 ms.

Moreover, the discretization time of each internal model is half of T_s in order to still obtain good performance without significantly affect the computational time. Each controller, with the previous settings, can run in real-time and provide good KPI improvements. Despite the small prediction horizon e high values of sampling time with respect the simulation on Simulink, the NMPC^(prev) with 4 motors still manage to reduce the longitudinal acceleration by reaching RMS values of \ddot{x}_b reduction w.r.t the passive configuration of about 66% for in-wheel model and about 64% for 4 on-board model. Also the 2 on-board powertrains still run in real-time by guaranteeing an improvement with respect to the passive configuration, even if in smaller percentages. For example, $\Delta\ddot{x}_{b,max}$ is about 19% better with respect to the passive case. By considering, instead, the NMPC^(w/o prev) the performance gets worse. These results highlight the importance of a pre-emptive action on the controllers also in a real time implementation.

Conclusions

This study has presented three different non-linear model predictive controllers (NMPCs) based on the road preview information, to attenuate the longitudinal acceleration oscillations caused by irregular road profiles. Each one of them, was related to a different electric vehicle's powertrains, such as in-wheel motors, 4 on-board motors and with 2 on-board motors with open differential. With respect to the existing literature the novelty is the inclusion of prediction models for longitudinal dynamics, also considering the torsional dynamics in the on-board powertrains. Through the robustness and sensitivity analyses and to the simulations on different road profiles, some conclusions can be formulated.

- By considering the optimal weight matrices for a positive step input, the NMPC formulation with road preview, for the in-wheel and 4 on-board models, achieves good longitudinal acceleration peak compensations, improving the performance up to the 80% with respect to the passive configuration. Instead, the 2 on-board model presents a loss of efficiency due to different parameters, such as the time constant of the motors, the equivalent inertia, and the shaft stiffness, but still guarantees a good improvement of around 25%. Moreover, without the road preview information, the improvements are less than 10%. This important difference of performance has proved the need to know in advance the road profile, in particular for a localized road event.
- Testing the vehicles at different speeds, the analysis has proved that the NMPC with the implementation of road preview, for the 4 motors' models, is robust in a wide speed range, from 20 to 80 km/h. In fact, $RMS_{\dot{x}_b}$, $VDV_{\dot{x}_b}$ and $\Delta\ddot{x}_{b,max}$ are reduced by an order of magnitude with respect to the passive case, while $RMS_{\ddot{a}_{x,b}}$ is reduced by a factor of about 3. Moreover, an equal improvement is not guaranteed by the 2 on-board model, which, as expected, has a loss of performance due to different motor time constant, which affects the performance at high speed.

Moreover, through tests at different motor torque demands, it has proved that only the in-wheel and 2 on-board models are not significantly affected. This

is due to a different maximum torque, which in the first case is not reached and in the second one is fully reached, also with null torque demand.

- The sensitivity analyses have shown that by changing different powertrains' parameters in the study cased, the performances of the NMPCs are affected. The first analysis is referred to the motor time constant, which has been increased from about 6 to 200 ms; thus, a progressive deterioration of KPIs has been obtained until the passive configuration's performance has been achieved. This study has proved that a wide range of motors with different time constant can be implemented. However, it is important to remember that, by changing the motor, also the inertia moment of the system changes. In fact, the motor's inertia corresponds to its main component. For this reason, the second analysed parameter has been the equivalent inertia at the wheels, which has been increased from around 1.4 to 2.8 Nm². In this case, from the lowest to the highest value, the KPIs have gotten worse by twice; for example, the RMS values of \ddot{x}_b goes from 0.05 to 0.1. The third parameter to have been taken into account is the shaft stiffness. A range of values, commonly used in a vehicle, has been analysed. By increasing the stiffness from 5000 to 12500 Nm/rad, a noticeable improvement has been obtained.

The last analysis has demonstrated, by considering different combinations of all the previous parameters at different backlashes, which parameters have the greatest influence. In fact, by considering a small backlash of 1.2°, the KPIs improvements are halved with a higher motor time constant, which corresponds to the one of the 2 on-board model, and they are further halved by doubling the equivalent inertia. Instead, increasing the backlash, the main parameter that affects the performance is only the motor time constant.

- By considering an uneven road profile and the road preview information, the NMPC for the in-wheel and 4 on-board models achieves great improvements from around 40% to more than 60%, depending on the selected KPI. Also, the 2 on-board model presents an improvement of all indicators in a range between 15% and 30%. Compared to the step profile test without the road profile information given in advance, the NMPC guarantees good improvements with values that go from more than 25% to more than 40%, with the exception of the 2 on-board model, which it is not capable to manage non-localized road events.
- The test with asymmetric road inputs on the two vehicles side, shows that the 2 on-board model, due to a unique requested torque, and equal half-shaft torque as consequence, cannot manage the longitudinal acceleration as the 4 on-board models. Indeed, by decreasing the asymmetric between the right

and left step from 0.5 m to 0.25 m, the KPIs decrease of about 20%. Situation that does not happen in the 4 on-board model.

Acknowledgements

Prima di concludere del tutto il mio periodo da studente, vorrei dedicare questo piccolo spazio del mio elaborato alle persone che mi sono state vicine in questo percorso di crescita professionale e personale.

Grazie al mio relatore Vigliani Alessandro, presente, puntuale e disponibile. Ringrazio il Prof. Aldo Sorniotti e il Prof. Umberto Montanaro per il progetto svolto all'università del Surrey che mi ha permesso di sviluppare maggiormente la mia capacità di analisi e di problem solving.

Ringrazio i miei genitori che hanno sempre sostenuto e appoggiato le mie scelte, qualsiasi esse siano; dal trasferirmi a Torino lontano di casa o intraprendere un viaggio lungo 6 mesi in un altro continente. Un grazie va alle mie sorelle, Federica e Luisa, che, nonostante si siano appropriate della mia camera e del mio letto durante la mia assenza, mi hanno confortato e aiutato. Ringrazio anche mia nonna e tutta la mia famiglia per il supporto datomi.

Ringrazio i miei amici storici, che nonostante la lontananza di 2 anni, sono sempre stati presenti. Grazie per aver ascoltato i miei sfoghi e per tutti i momenti di spensieratezza.

Una nota particolare per gli amici che ho conosciuto a Torino e i anche ragazzi che mi hanno accompagnato nella lontana Cholula; Andrea Bombo, Ornella, Sabrina, Andrea Lai, Pao, Ludo, Giovanni e Domenico. Senza di loro, probabilmente, sarei stato in balia degli eventi e disperso in qualche punto remoto del Messico. Con la speranza di poter trascorre altro tempo con loro, li ringrazio di cuore per aver reso indimenticabili questi anni di università.

Un grazie va anche a Davide e Pietro per aver collaborato con me in questo progetto. Ringrazio tutte le persone che ho conosciuto in Inghilterra per la compagnia e il divertimento. Grazie anche e soprattutto ad Elisabetta, Irina, Victor e Greta per i bei momenti trascorsi insieme.

Un grazie di cuore a tutti.

Bibliography

- [1] Carl Knospe. «PID control». In: *Control Systems Magazine, IEEE* 26 (Mar. 2006), pp. 30–31. DOI: 10.1109/MCS.2006.1580151 (cit. on p. 10).
- [2] Daniel Watzeing. *Automated Driving*. Springer, 2017 (cit. on pp. 10, 11, 13).
- [3] T. Hessburg and M. Tomizuka. «Fuzzy logic control for lateral vehicle guidance». In: *Proceedings of IEEE International Conference on Control and Applications*. 1993, 581–586 vol.2. DOI: 10.1109/CCA.1993.348341 (cit. on p. 11).
- [4] Daniel Watzenig and Martin Horn. *Automated Driving: Safer and More Efficient Future Driving*. 1st. Springer Publishing Company, Incorporated, 2016. ISBN: 3319318934 (cit. on p. 12).
- [5] C. Edwards and S. Spurgeon. *Sliding Mode Control: Theory And Applications*. Series in Systems and Control. CRC Press, 1998. ISBN: 9781498701822. URL: <https://books.google.co.uk/books?id=8U1ZDwAAQBAJ> (cit. on p. 12).
- [6] Arie Levant and L. Levantovsky. «Sliding Order and Sliding Accuracy in Sliding Mode Control». In: *International Journal of Control - INT J CONTR* 58 (Dec. 1993), pp. 1247–1263. DOI: 10.1080/00207179308923053 (cit. on p. 12).
- [7] G. Monsees. «Discrete-time sliding mode control». PhD thesis. technische universiteit delft, 2002. URL: <https://www.tudelft.nl/> (cit. on p. 12).
- [8] V. Utkin. «Variable structure systems with sliding modes». In: *IEEE Transactions on Automatic Control* 22.2 (1977), pp. 212–222. DOI: 10.1109/TAC.1977.1101446 (cit. on p. 12).
- [9] Jan Maciejowski. *Predictive Control With Constraints*. Jan. 2002 (cit. on p. 14).
- [10] Manfred Morari and Jay H. Lee. «Model predictive control: past, present and future». In: *Computers & Chemical Engineering* 23.4 (1999), pp. 667–682. ISSN: 0098-1354. DOI: [https://doi.org/10.1016/S0098-1354\(98\)00301-9](https://doi.org/10.1016/S0098-1354(98)00301-9). URL: <https://www.sciencedirect.com/science/article/pii/S0098135498003019> (cit. on p. 14).

- [11] Carlos E. Garcia, David M. Prett, and Manfred Morari. «Model predictive control: Theory and practice - A survey». In: *Autom.* 25 (1989), pp. 335–348 (cit. on p. 14).
- [12] J. Richalet, A. Rault, J. L. Testud, and J. Papon. «Model predictive heuristic control: Applications to industrial processes». In: *Autom.* 14 (1978), pp. 413–428 (cit. on p. 14).
- [13] David A. Hokanson and James G. Gerstle. «Dynamic Matrix Control Multivariable Controllers». In: *Practical Distillation Control*. Ed. by William L. Luyben. New York, NY: Springer US, 1992, pp. 248–271. ISBN: 978-1-4757-0277-4. DOI: 10.1007/978-1-4757-0277-4_12. URL: https://doi.org/10.1007/978-1-4757-0277-4_12 (cit. on p. 14).
- [14] Masahiro Ohshima, Hiromu Ohno, Iori Hashimoto, Mikiro Sasajima, Masayuki Maejima, Keiichi Tsuto, and Tadaharu Ogawa. «Model predictive control with adaptive disturbance prediction and its application to fatty acid distillation column control». In: *Journal of Process Control* 5.1 (1995), pp. 41–48. ISSN: 0959-1524. DOI: [https://doi.org/10.1016/0959-1524\(95\)95944-9](https://doi.org/10.1016/0959-1524(95)95944-9). URL: <https://www.sciencedirect.com/science/article/pii/0959152495959449> (cit. on p. 14).
- [15] Carlos E Garcia and Manfred Morari. «Internal model control. A unifying review and some new results». In: *Industrial and Engineering Chemistry Process Design and Development* 21.2 (1982), pp. 308–323 (cit. on p. 14).
- [16] Manfred Morari and Evangelos Zafiriou. *Robust process control*. Morari, 1989 (cit. on p. 14).
- [17] Elisa Capello, Satoshi Satoh, and Matteo Facchino. «MPC Design for CMG based Testbed». In: () (cit. on p. 15).
- [18] J Rawlings and D Mayne. «Postface to model predictive control: Theory and design». In: *Nob Hill Pub* 5 (2012), pp. 155–158 (cit. on p. 15).
- [19] Vidas Žuraulis, Loreta Levulytė, and Edgar Sokolovskij. «The impact of road roughness on the duration of contact between a vehicle wheel and road surface». In: *Transport* 29.4 (2014), pp. 431–439. DOI: 10.3846/16484142.2014.984330 (cit. on p. 18).
- [20] Rafal Burdzik. «Identification of structure and directional distribution of vibration transferred to car-body from road roughness». In: *Journal of Vibro-engineering* 16 (Feb. 2014), pp. 324–333 (cit. on p. 18).
- [21] Krzysztof Prażnowski, Jarosław Mamala, Michael Smieja, and Mariusz Kupina. «Assessment of the Road Surface Condition with Longitudinal Acceleration Signal of the Car Body». In: *Sensors (Basel, Switzerland)* 20 (Oct. 2020). DOI: 10.3390/s20215987 (cit. on p. 18).

- [22] Nacer Hamadi, Djamel-eddine Ameddah, and Hocine Imine. «Investigation of the Adherence Influence on the Dynamic Behavior of the Vehicle». In: *International Journal of Hybrid Information Technology* Vol 7 (Oct. 2014), PP.85–102. DOI: 10.14257/ijhit.2014.7.5.08 (cit. on p. 18).
- [23] K.T. Chau. *Electric Vehicle Machines and Drives: Design, Analysis and Application*. May 2015, pp. 1–400. ISBN: 9781118752524. DOI: 10.1002/9781118752555 (cit. on pp. 18, 22).
- [24] Satoshi Murata. «Innovation by in-wheel-motor drive unit». In: *Vehicle System Dynamics* 50.6 (2012), pp. 807–830. DOI: 10.1080/00423114.2012.666354 (cit. on p. 18).
- [25] Ziyong Song, Li Jianqiu, Zhibin Shuai, Liangfei Xu, and Minggao Ouyang. «Fuzzy logic torque control system in four-wheel-drive electric vehicles for active damping vibration control». In: *International Journal of Vehicle Design* 68 (Jan. 2015), p. 55. DOI: 10.1504/IJVD.2015.071068 (cit. on p. 18).
- [26] Yechen Qin, Ze Zhao, Zhenfeng Wang, and Guofa Li. «Study of Longitudinal–Vertical Dynamics for In-Wheel Motor-Driven Electric Vehicles». In: *Automotive Innovation* 4 (Apr. 2021), pp. 1–11. DOI: 10.1007/s42154-021-00141-5 (cit. on p. 18).
- [27] Ze Zhao, Hamid Taghavifar, Haiping Du, Yechen Qin, Mingming Dong, and Liang Gu. «In-Wheel Motor Vibration Control for Distributed-Driven Electric Vehicles: A Review». In: *IEEE Transactions on Transportation Electrification* 7 (Dec. 2021), pp. 2864–2880. DOI: 10.1109/TTE.2021.3074970 (cit. on p. 18).
- [28] Z.Q. Zhu, Dahaman Ishak, David Howe, and Chen Jintao. «Unbalanced Magnetic Forces in Permanent-Magnet Brushless Machines With Diametrically Asymmetric Phase Windings». In: *Industry Applications, IEEE Transactions on* 43 (Dec. 2007), pp. 1544–1553. DOI: 10.1109/TIA.2007.908158 (cit. on p. 18).
- [29] Go Nagaya, Yasumichi Wakao, and Akihiko Abe. «Development of an in-wheel drive with advanced dynamic-damper mechanism». In: *Jsaе Review - JSAE REV* 24 (Oct. 2003), pp. 477–481. DOI: 10.1016/S0389-4304(03)00077-8 (cit. on p. 19).
- [30] Liqiang Jin, Yajing Yu, and Yue Fu. «Study on the ride comfort of vehicles driven by in-wheel motors». In: *Advances in Mechanical Engineering* 8 (Mar. 2016). DOI: 10.1177/1687814016633622 (cit. on p. 19).

- [31] R. Vos, I.J.M. Besselink, and H. Nijmeijer. «Influence of in-wheel motors on the ride comfort of electric vehicles». English. In: *Proceedings of the 10th International Symposium on Advanced Vehicle Control (AVEC10), 22-26 August 2010, Loughborough, United Kingdom*. 2010, pp. 835–840 (cit. on p. 19).
- [32] Xinbo CHEN, Jun YIN, Wei WANG, Lixin WU, and Feng TANG. «Approaches to diminish large unsprung mass negative effects of wheel side drive electric vehicles». In: *Journal of Advanced Mechanical Design, Systems, and Manufacturing* 10.4 (2016), JAMDSM0064–JAMDSM0064. DOI: 10.1299/jamdsm.2016jamdsm0064 (cit. on p. 19).
- [33] Jian Jun Zhu, Amir Khajepour, E. Esmailzadeh, and Alireza Kasaiezadeh. «Ride quality evaluation of a vehicle with a planar suspension system». In: *Vehicle System Dynamics - VEH SYST DYN* 50 (Mar. 2012), pp. 395–413. DOI: 10.1080/00423114.2011.592591 (cit. on p. 19).
- [34] Zhiqiang Guo, Wei Wu, and Shihua Yuan. «Longitudinal-vertical dynamics of wheeled vehicle under off-road conditions». In: *Vehicle System Dynamics* (Sept. 2020), pp. 1–21. DOI: 10.1080/00423114.2020.1823003 (cit. on p. 19).
- [35] Francesco Bottiglione, Aldo Sorniotti, and Leo Shead. «The effect of half-shaft torsion dynamics on the performance of a traction control system for electric vehicles». In: *Proceedings of the Institution of Mechanical Engineers, Part D: Journal of Automobile Engineering* 226.9 (2012), pp. 1145–1159. DOI: 10.1177/0954407012440526 (cit. on p. 19).
- [36] Jianwu Zhang, Benben Chai, and Xingyang Lu. «Active oscillation control of electric vehicles with two-speed transmission considering nonlinear backlash». In: *Proceedings of the Institution of Mechanical Engineers, Part K: Journal of Multi-body Dynamics* 234.1 (2020), pp. 116–133. DOI: 10.1177/1464419319877332 (cit. on p. 19).
- [37] Fabian Walz, Tobias Schucht, Johann Reger, and Soeren Hohmann. «Shaft Torque and Backlash Estimation for Longitudinal Motion Control of All-Wheel-Drive Vehicles». In: Aug. 2018. DOI: 10.1109/CCTA.2018.8511096 (cit. on p. 19).
- [38] Alessandro Scamarcio, Carmine Caponio, Mario Mihalkov, Petar Georgiev, Javad Ahmadi, Kai Man So, Davide Tavernini, and Aldo Sorniotti. «Predictive anti-jerk and traction control for V2X connected electric vehicles with central motor and open differential». In: *IEEE Transactions on Vehicular Technology* (2022), pp. 1–1. DOI: 10.1109/TVT.2022.3143497 (cit. on pp. 19, 26).

- [39] J. Heywood and P.J. Heywood. *Internal Combustion Engine Fundamentals*. Automotive technology series. McGraw-Hill Education, 1988. ISBN: 9780070286375. URL: <https://books.google.co.uk/books?id=u9FSA AAAMAAJ> (cit. on p. 19).
- [40] Alessandro Scamarco. «Active systems for drivability improvement of electric vehicles». PhD thesis. University of Surrey, 2020 (cit. on pp. 28, 31).
- [41] Eric Armengaud, Omar Hegazy, Bernhard Brandstatter, Valentin Ivanov, Reinhard Tatschl, Michele De Gennaro, Aldo Sornioti, Joeri Van Mierlo, and Christof Schernus. «European Innovation for Next Generation Electrified Vehicles and Components». In: Nov. 2019, pp. 1–6. DOI: 10.1109/ICCVE45908.2019.8964843 (cit. on p. 30).
- [42] Printed motor works. *XR32-13 In-Wheel Motor*. Online (cit. on p. 30).
- [43] Remy. *HVH250-115 Electric Motor*. Online (cit. on p. 30).
- [44] Remy. *HVH250-090 Electric Motor*. Online (cit. on p. 30).
- [45] Enrico Galvagno, Mauro Velardocchia, and Alessandro Vigliani. «Drivability enhancement and transient emission reduction for a mild hybrid diesel-electric truck». In: *INTERNATIONAL JOURNAL OF POWERTRAINS* 2 (Jan. 2013), pp. 262–291. DOI: 10.1504/IJPT.2013.054154 (cit. on p. 31).
- [46] Fabian Walz, Tobias Schucht, Johann Reger, and Soeren Hohmann. «Shaft Torque and Backlash Estimation for Longitudinal Motion Control of All-Wheel-Drive Vehicles». In: Aug. 2018. DOI: 10.1109/CCTA.2018.8511096 (cit. on p. 33).
- [47] Chen Lv, Junzhi Zhang, Yutong Li, and Ye Yuan. «Mode-switching-based active control of powertrain system with nonlinear backlash and flexibility for electric vehicle during regenerative deceleration». In: *Proceedings of the Institution of Mechanical Engineers Part D Journal of Automobile Engineering* 229 (Aug. 2015), pp. 1429–1442. DOI: 10.1177/0954407014563552 (cit. on p. 33).
- [48] «Copyright». In: *Tire and Vehicle Dynamics (Third Edition)*. Ed. by Hans B. Pacejka. Third Edition. Oxford: Butterworth-Heinemann, 2012, p. iv. ISBN: 978-0-08-097016-5. DOI: <https://doi.org/10.1016/B978-0-08-097016-5.02001-5>. URL: <https://www.sciencedirect.com/science/article/pii/B9780080970165020015> (cit. on p. 37).
- [49] Ijm Igo Besselink, Hans B. Pacejka, Aje Antoine Schmeitz, and Sven T. H. Jansen. «The SWIFT tyre model : overview and applications». In: 2004 (cit. on p. 37).

- [50] Carlo Lugaro, Mohsen Alirezai, Ioannis Konstantinou, and Abhijeet Behera. «A Study on the Effect of Tire Temperature and Rolling Speed on the Vehicle Handling Response». In: 2020 (cit. on p. 38).
- [51] C Lugaro, I Konstantinou, and M Mazzeo. «A tire model extension for predicting temperature and rolling speed influences on tire performance». In: *JSAE Annual Congress*. Vol. 5. 2020, pp. 25–26 (cit. on p. 38).
- [52] Hideki Fukudome. *Reduction of longitudinal vehicle vibration using In-Wheel motors*. Tech. rep. SAE Technical Paper, 2016 (cit. on p. 47).
- [53] Ibrahim Bakirci and Nino Katadzic. «The use of wheel torque modulation to mitigate road induced longitudinal vibrations». MA thesis. 2014 (cit. on p. 47).
- [54] Shota Yamada, Thomas Beauduin, Hiroshi Fujimoto, Takeshi Kanou, and Etsuo Katsuyama. «Model-based longitudinal vibration suppression control for electric vehicles with geared in-wheel motors». In: July 2017, pp. 517–522. DOI: 10.1109/AIM.2017.8014069 (cit. on p. 47).
- [55] Thomas Beauduin, Shota Yamada, Hiroshi Fujimoto, Takeshi Kanou, and Etsuo Katsuyama. «Control-oriented modelling and experimental modal analysis of Electric Vehicles with geared In-Wheel Motors». In: July 2017, pp. 541–546. DOI: 10.1109/AIM.2017.8014073 (cit. on p. 47).
- [56] Fabian Walz and Sören Hohmann. «On model-based longitudinal feed-forward motion control for low velocities on known road profiles». In: *Vehicle System Dynamics* 57.8 (2019), pp. 1126–1142. DOI: 10.1080/00423114.2018.1498111 (cit. on p. 47).
- [57] F. Walz and S. Hohmann. «Model predictive longitudinal motion control for low velocities on known road profiles». In: *Vehicle System Dynamics* 58.8 (2020), pp. 1310–1328. DOI: 10.1080/00423114.2019.1618880 (cit. on p. 47).
- [58] Víctor Vidal, Pietro Stano, Gaetano Tavolo, Miguel Dhaens, Davide Tavernini, Patrick Gruber, and Aldo Sorniotti. «On Pre-Emptive In-Wheel Motor Control for Reducing the Longitudinal Acceleration Oscillations Caused by Road Irregularities». In: *IEEE Transactions on Vehicular Technology* (2020) (cit. on pp. 47, 72).
- [59] Boris Houska, Hans Joachim Ferreau, and Moritz Diehl. «ACADO toolkit—An open-source framework for automatic control and dynamic optimization». In: *Optimal Control Applications and Methods* 32.3 (2011), pp. 298–312 (cit. on p. 48).

- [60] D. Ariens, B. Houska, H. Ferreau, and F. Logist. *ACADO: Toolkit for Automatic Control and Dynamic Optimization*. <http://www.acadotoolkit.org/>. Optimization in Engineering Center (OPTEC) (cit. on p. 48).
- [61] Filip Logist, Mattia Vallerio, Boris Houska, Moritz Diehl, and Jan Van Impe. «Multi-objective optimal control of chemical processes using ACADO toolkit». In: *Computers & Chemical Engineering* 37 (2012), pp. 191–199 (cit. on p. 49).
- [62] H.J. Ferreau, C. Kirches, A. Potschka, H.G. Bock, and M. Diehl. «qpOASES: A parametric active-set algorithm for quadratic programming». In: *Mathematical Programming Computation* 6.4 (2014), pp. 327–363 (cit. on p. 50).
- [63] AJC Schmeitz, STH Jansen, HB Pacejka, JC Davis, NN Kota, CG Liang, and G Lodewijks. «Application of a semi-empirical dynamic tyre model for rolling over arbitrary road profiles». In: *International Journal of Vehicle Design* 36.2-3 (2004), pp. 194–215 (cit. on p. 50).
- [64] Siemens Digital Industries Software. «Simcenter Tire – MF-Tyre/MF-Swift User Manual». In: (Dec. 2010) (cit. on p. 55).
- [65] Huiran Wang, Qidong Wang, Wuwei Chen, Linfeng Zhao, and Dongkui Tan. «A novel path tracking approach considering safety of the intended functionality for autonomous vehicles». In: *Proceedings of the Institution of Mechanical Engineers, Part D: Journal of Automobile Engineering* 236.4 (2022), pp. 738–752. DOI: 10.1177/09544070211020535 (cit. on p. 77).
- [66] Hong Wang, Yanjun Huang, Amir Khajepour, Yubiao Zhang, Yadollah Rasehipour, and Dongpu Cao. «Crash Mitigation in Motion Planning for Autonomous Vehicles». In: *IEEE Transactions on Intelligent Transportation Systems* 20.9 (2019), pp. 3313–3323. DOI: 10.1109/TITS.2018.2873921 (cit. on p. 77).